COMPUTATIONAL FLUID DYNAMICS STUDY OF AEROSOL TRANSPORT AND DEPOSITION MECHANISMS

A Dissertation

by

YINGJIE TANG

Submitted to the Office of Graduate Studies of
Texas A&M University
in partial fulfillment of the requirements for the degree of

DOCTOR OF PHILOSOPHY

May 2012

Major Subject: Mechanical Engineering

Computational Fluid Dynamics Study of Aerosol Transport and Deposition Mechanisms

COMPUTATIONAL FLUID DYNAMICS STUDY OF AEROSOL TRANSPORT AND DEPOSITION MECHANISMS

A Dissertation

by

YINGJIE TANG

Submitted to the Office of Graduate Studies of
Texas A&M University
in partial fulfillment of the requirements for the degree of

DOCTOR OF PHILOSOPHY

Approved by:

Co-Chairs of Committee,	Bing Guo
	Devesh Ranjan
Committee Members,	Hamn-Ching Chen
	Qi Ying
Head of Department,	Jerald Caton

May 2012

Major Subject: Mechanical Engineering

ABSTRACT

Computational Fluid Dynamics Study of Aerosol Transport and Deposition Mechanisms.

(May 2012)

Yingjie Tang, B.S., Tsinghua University;

M.S., Tsinghua University

Co-Chairs of Advisory Committee: Dr. Bing Guo
Dr. Devesh Ranjan

In this work, various aerosol particle transport and deposition mechanisms were studied through the computational fluid dynamics (CFD) modeling, including inertial impaction, gravitational effect, lift force, interception, and turbophoresis, within different practical applications including aerosol sampling inlet, filtration system and turbulent pipe flows. The objective of the research is to obtain a better understanding of the mechanisms that affect aerosol particle transport and deposition, and to determine the feasibility and accuracy of using commercial CFD tools in predicting performance of aerosol sampling devices. Flow field simulation was carried out first, and then followed by Lagrangian particle tracking to obtain the aerosol transport and deposition information. The CFD-based results were validated with experimental data and empirical correlations.

In the simulation of the aerosol inlet, CFD-based penetration was in excellent agreement with experimental results, and the most significant regional particle

deposition occurred due to inertial separation. At higher free wind speeds gravity had less effect on particle deposition. An empirical equation for efficiency prediction was developed considering inertial and gravitational effects, which will be useful for directing design of similar aerosol inlets.

In the simulation of aerosol deposition on a screen, a "virtual surface" approach, which eliminates the need for the often-ambiguous user defined functions, was developed to account for particle deposition due to interception. The CFD-based results had a good agreement compared with experimental results, and also with published empirical correlations for interception.

In the simulation of turbulent deposition in pipe flows, the relation between particle deposition velocity and wall-normal turbulent velocity fluctuation was quantitative determined for the first time, which could be used to quantify turbulent deposition, without having to carry out Lagrangian particle tracking. It suggested that the Reynolds stress model and large eddy simulation would lead to the most accurate simulated aerosol deposition velocity. The prerequisites were that the wall-adjacent y+ value was sufficiently low, and that sufficient number of prism layers was applied in the near-wall region. The "velocity fluctuation convergence" would be useful criterion for judging the adequacy of a CFD simulation for turbulent deposition.

DEDICATION

To my grandfather

ACKNOWLEDGEMENTS

I would like to thank my advisory committee chair, Dr. Bing Guo, my committee co-chair Dr. Ranjan, and my committee members, Dr. Chen and Dr. Ying, for their guidance and support throughout the course of this research.

I would also like to thank Dr. Andrew McFarland for valuable guidance and discussions on CFD simulation of aerosol sampling devices. I am grateful for the instructions and helps from my colleagues and the faculty members of the department, who made my study at Texas A&M University a great experience. I would like to extend my gratitude to the Aerosol Technology Laboratory and Advanced Mixing Laboratory as well, which provided a dynamic research environment, and to all the co-workers who managed to help and participate in the study.

Finally, thanks to my mother and father for their encouragement and love.

NOMENCLATURE

A	the area
a	the acceleration
C_c	the Cunningham slip correction factor
C_p	the particle concentration
C_D	the drag factor
D	the molecular diffusivity
D_i	the inner diameter
D_o	the outer diameter
d_c	the characteristic dimension
d_f	the fiber diameter
d_p	the aerodynamic particle diameter
e_{rms}	the root-mean-square normalized error
$\mathbf{F_D}$	the drag force
F	the Fanning friction factor
f_{OA}	the fraction of open area
G	the dimensionless gravitational settling parameter
GSD	the geometric standard deviation
J	the particle deposition flux
K	the turbulence kinetic energy; wall-normal velocity fluctuation
Ku	the Kuwabara hydrodynamic factor

Kn	the Knudsen number
L	the length
m_p	the particle mass
n	the particle number
P	the penetration efficiency
Q	the volumetric flow rate
R	the interception parameter
Re	the Reynolds number
R_{int}	the interception ratio
r_t	the turbophoresis factor
r_v	the velocity ratio
S_c	the particle source or sink term
S_{tk}	the Stokes number
TKE	the turbulence kinetic energy
t	the time
U	the average velocity
U_0	the uniform flow velocity
U^*	the sampling velocity
$\mathbf{u}$	the flow velocity
$\bar{\mathbf{u}}$	the time-averaged velocity
$\mathbf{u'}$	the turbulence velocity fluctuation
$\mathbf{u_p}$	the particle velocity

u_*	the turbulence friction velocity
V_{dep}	the particle deposition velocity
V_+	the dimensionless particle deposition velocity
V^c	the particle convective velocity
α	the particle responsiveness factor
ε_p	the eddy diffusivity
λ	the molecular mean free path of the gas
ρ	the density
Γ	the effective particle diffusivity
τ	the particle relaxation time
$\tau+$	the dimensionless particle relaxation time
τ_L	the Lagrangian time scale
μ	the dynamic viscosity
ν	the kinematic viscosity
ν_t	the fluid turbulent viscosity
η	the collection efficiency
η_{SFE}	the single-fiber-efficiency

TABLE OF CONTENTS

LIST OF FIGURES

Page

LIST OF TABLES

1. INTRODUCTION *

1.1 Background

An aerosol is a suspension of solid or liquid particulate matter in a gas (Hinds, 1999). Aerosols could be naturally existing in the earth atmosphere, in the forms of originating residuals from volcanoes, dust storms, fires, living vegetation, and sea spray. On the other hand, aerosols could as well be produced by human social activities, in both incidental and intentional ways. Fossil fuel combustion could create aerosols, or intentionally sources of human society could product the harmful substances or pollutants as aerosols (Davies, 1966; Hinds, 1999; Reist, 1984; Vincent, 1995); an aerosol is also a commonly applied form of medication delivery for therapeutic treatments. As a consequence, the climate and the atmosphere visibility could be affected by aerosols; and more importantly, unfavorably effects to the human health would be caused by aerosols if inhaled. Thus, the detection and identification of critical aerosol properties, such as the size distribution, the concentration and the material or chemical composition, and the health effects of aerosol particles are extremely crucial nowadays. Apparently, such research requires quantitative information of the particle transport and deposition in an aerosol fluid of interest. For an accurate measurement of

---

This dissertation follows the style of *Journal of Aerosol Science.*

aerosol in the atmosphere, the particle deposition in aerosol sampling and collection devices needs to be quantitated, which would be highly up to the prediction of particle transport trajectories. (Tang & Guo, 2011)

Normally, an aerosol is treated as an active system, in which the particle concentration, the size distribution, and the material/chemical composition would change because of the coagulation, the evaporation/condensation, the dispersion, the deposition, and the chemical reactions. It should be noted that the particle transport and deposition is the emphasis of this dissertation research, without focusing on the particle growth due to any process such as the coagulation, the chemical reaction, or physical changes like condensation and evaporation. In other words, this study is only reasonable for processes in which the particle dispersion/deposition time scales are so short, and that deviations of the aerosol content because of other mechanisms could be negligible.

A general description of aerosol mechanical basics is before discussions on particle transport and deposition. Typical mechanisms would include the particle inertial separation, the gravitational settling, the electrostatic deposition, the interception effect, the Brownian motion, the thermophoresis, and the turbulent dispersion/turboporesis (Hinds, 1999):

In practical studies, it should be noted that the density of particles is normally greater than that of the gas, and thus inertial separation (relative movements between particles and the gas flow) usually happens when the air flow accelerates, decelerates, or as the flow direction changes. The inertial separation of a particle happens when the particle is unable to adjust quickly enough to the abruptly changing the streamlines. This

is a normal and perhaps dominating mechanism for particle deposition in cases such as flows in cyclones, impactors, and pipe bends. The parameter which is used to govern this mechanism is the Stokes number, S_{tk}, which is defined as:

$$Stk = \frac{\rho_p d_p^2 U_0 C_c}{18 \mu d_c} \tag{1.1}$$

where ρ_p is the particle density; d_p is the aerodynamic diameter of particle; U_0 is the flow velocity; C_c is Cunningham slip correction factor; μ is the dynamic viscosity of fluid; and, d_c is the characteristic dimension length. When the Stokes number is large, higher inertia would make the particle more easily separated from the flow; when the Stokes number is lower and approaching zero, the particle would be more likely following the flow streamline, and less opportunities for separation.

The density difference between the particle and the air also could cause the particle settling in the earth's gravitational field. Since in most cases, the magnitude and the direction of the gravity would be constant, the gravitational effect would be more significant when the particle size is large (or the density is large) or the fluid velocity is low (longer settling time through the flow channel).

Particles sometimes carry electrical charges, which could cause the particle deposition due to electrostatic forces (Davies, 1966; Hinds, 1999; Vinchurkar *et al.*, 2009). It should be noted that it is always difficult to quantify the electrostatic deposition unless the charge on the particles is known. And this effect would be significant only when the charge on the particles would be in some quantifiable way (Hinds, 1999).

Another potentially important mechanism is the interception effect. Interception occurs due to the finite size of a particle when it comes close to a surface (Hinds,1999). When the particle follows a fluid streamline to get into one particle radius from any surface, this particle would intercepted by this surface even the trajectory of this particle mass point has not impacted on the surface. Interception could be an important factor if the characteristic dimension of the device surface is small and in the similar magnitude as the particles, and sometimes be overlooked.

Brownian motion causes the thermal diffusion process and is especially important for the deposition of small particles (diameter smaller than 1 micrometer). It is the unbalanced motion of an aerosol particle in air caused by random variations in the relentless bombardment of gas molecules against the particle. For large particles, it should be noted that this effect could be neglected compared to those mentioned earlier.

Thermophoresis is defined for the particle-motion phenomenon that particles move due to temperature gradient in the gas, which causes particles to deposit when a warm aerosol is in contact with a cold surface (Tsai et al., 2004).

Turbulence is another important factor to influence on the particle transport and deposition, which is related to a phenomenon called the turbophoresis (Guha, 2008). Change of velocity fluctuation (turbulent kinetic energy gradient) could also cause inertial influence on particle transport and deposition. This is an effect similar to the thermophoresis, and note that the driving force here is the turbulent kinetic energy gradient, not the temperature gradient like thermophoresis. One classic research example is that in a vertical straight pipe, the particles within the internal flow could also be

possible to deposit on the pipe wall, due to the turbophoresis effect, and other mechanisms, like inertial separation or gravitational effect, would not be involved in this case.

In some specific circumstances, the lift force would be considered (perpendicular to the relative translational velocity between the particle and the gas) on a particle due to relative rotation between the particle and the gas (Saffman, 1965). This would mostly occur in a shear flow where the fluid velocity gradient becomes significant, like in a boundary flow.

In a Lagrangian perspective, Newton's second law was used for the motion of a particle description:

$$\frac{\mathrm{d}\mathbf{u}_\mathbf{p}}{\mathrm{d}t} = \frac{\mathbf{F}_\mathbf{D}}{m_\mathrm{p}} + \mathbf{a}\,, \tag{1.2}$$

where $\mathbf{u_p}$ is the particle velocity; $\mathbf{F_D}$ is the drag force; m_p is particle mass; $\mathbf{a}$ is the accelerations due to all forces other than drag force, which includes the gravity, the electrostatic force, the thermophoretic force, and lift force (Hinds, 1999; Reist, 1984; Saffman, 1965).

Note that in Equation (1.2), the turbulent influence on particles is employed through the fluctuation of the gas velocity, which in turn leads to fluctuation of the drag force $\mathbf{F_D}$. In most cases, the drag force may be expressed by applying the Stokes law (Hinds, 1999):

$$\mathbf{F_D} = \frac{3\pi\mu d_\mathrm{p}}{C_\mathrm{c}}\left(\mathbf{u} - \mathbf{u_p}\right), \tag{1.3}$$

where **u** is the gas velocity (local); μ is the fluid dynamic viscosity; d_p is the aerodynamic particle diameter; C_c is the Cunningham slip correction factor. The Stokes law applies when the particle Reynolds number, based on the particle diameter and gas-particle relative velocity (also known as the slip velocity), is much smaller than unity. If the Reynolds number is high, then the appropriate drag force calculation should be used; and for non-spherical particles, a shape factor should be used (Hinds, 1999).

The Cunningham slip correction factor is employed here in Equation (1.3) to correct for the non-continuum effect when the particle size approaches the molecular mean free path of the air, λ. It is defined as (Hinds, 1999):

$$C_c = 1 + \frac{\lambda}{d_p}\left[2.34 + 1.05\exp\left(-0.39\frac{d_p}{\lambda}\right)\right], \tag{1.4}$$

On the other hand, particle transport and deposition may also be defined and processed with an Eulerian framework. The generally transport equation for the aerosol concentration in an Eulerian approach is:

$$\frac{\partial \rho C_p}{\partial t} + \nabla\cdot\left(\rho \mathbf{u} C_p\right) = \nabla\cdot\left(\Gamma\nabla C_p\right) + S_c, \tag{1.5}$$

where C_p is the particle concentration; ρ is the air density for dilute aerosols; Γ is the effective particle diffusivity; S_c the particle source or sink term. The effective particle diffusivity Γ is defined as a function of Brownian motion and eddy diffusivity (Hinds, 1999):

$$\Gamma = \rho\left(D + \varepsilon_p\right), \tag{1.6}$$

where D represents the molecular diffusivity and ε_p is the eddy diffusivity in Equation (1.6).

Numerical modeling process to address the particle transport and deposition profile could be carried out, based on different aerosol properties. Generally in most applications, the particle concentration is considered to be low, and the particles are several orders of magnitude smaller than the characteristic dimensions of the flow channel. This is usually referred to as the "one-way coupling" problem (ANSYS, 2008). The flow properties of the studied aerosol flow, like viscosity, are fundamentally the same as those of the air. It could also be safe to assume that the particles do not considerably influence the flow field profile, and the movement of any single particle is not affected by other particles. Therefore, numerical modeling process could be carried out on the gas flow field first without considering the particles, and then followed by the Lagrangian particle tracking (Longest & Xi, 2007) or the Eulerian particle diffusion simulation based on the simulated flow field (Mitsakou et al., 2005). On the contrary, when particle concentration is high, or particle size is comparable to dimensions of the flow channel, it is essential and necessary to consider aerodynamic particle-gas and particle-particle interactions in modeling process (Tsuji, 2007; Zhou et al., 2011); if the electrical effect remains, the effect of charged particles on the electric field must be resolved, e.g. by solving the Poisson Equation (Hinds, 1999; Reist, 1984; Vinchurkar, et al., 2009). Furthermore, when the particle concentration is sufficiently high, the flow could become the granular flow, and the applicable flow equations are no longer the same as for the normal dilute aerosols (Coroneo et al., 2011; S. H. Hosseini et al., 2010).

If the particle size is considerably large relative to the size of the flow channel, such as aerosol flow through porous media, the effect of particles on the flow field must be considered and addressed (Chen & Hsiau, 2008; Shapiro & Brenner, 1989). However in this study, the study focus would be on low concentration aerosol flows with particles size much smaller than the size of the flow channel, which is a practical situation in most common aerosol cases in industry.

To study on particle transport and deposition, experimental and numerical approaches are generally applied. Aerosol properties may be measured experimentally in the laboratory or within an "uncontrolled" environment such as the earth atmosphere. The typical test procedure involves locating the device or the model to an incoming aerosol flow with a known particle size distribution and concentration profile. A usual assumption is made that the concentration in the incoming aerosol flow is designed to be spatially uniform. It could be measured that the aerosol concentration at the outlet of the device or the model, which could be used to determine the fraction of deposition. The particle concentration may be determined by gravimetric measurement, fluorescence intensity, or other methods (Hinds, 1999). Experimental measurement is an indispensable approach for quantifying particle transport and deposition. It has yielded many useful empirical relations for relatively "standard" problems such as the particle deposition in impactors, aspiration ratio of thin-wall probes, and turbulent deposition in pipe flows (Gong *et al.*, 1996; Hinds, 1999; S. Parker *et al.*, 2008; Stein, 2008).

The motivation for using computational fluid dynamics (CFD) to simulate aerosol transport and deposition is mainly to reduce cost of engineering design and to

obtain information that is difficult to obtain through experimental measurements (Tang & Guo, 2011). For instance, the aerosol sampling system designs traditionally require laborious experiments, especially for complex flow fields and cases without scaling laws. CFD-based "numerical experiments" could comparatively be used to replace the physical experiments because of its lower design cost. Also in other cases, experimental measurements are difficult to obtain because of physical conditions (K. Miller *et al.*, 2000; Murphy *et al.*, 1992; Rostami, 2009). For example in human respiratory tract, information of the aerosol deposition could be very important for understanding the biologic effects of inhaled aerosols, but special techniques, such as the tracing isotope-tagged particles, are needed to measure regional particle deposition in the human respiratory tract (Stahlhofen, 1980; Stahlhofen et al., 1983).

Since 1990s, CFD-based simulation of aerosol transport and deposition has a crucial development. It has been employed to evaluate the aerosol deposition properties in aerosol sampling devices including impactors (Stein, 2008; Vinchurkar, et al., 2009), cyclones (Gimbun et al., 2005; Griffiths & Boysan, 1996; Gu et al., 2004; Hoekstra et al., 1999; Hu & McFarland, 2007; Kim & Lee, 2001), filters (Deuschle et al., 2008; Fortes & Laserna, 2010; T. Han, 2007; T. Han et al., 2009; S. A. Hosseini & Tafreshi, 2010; Tronville & Rivers, 2005; J. Wang & Pui, 2009), and inlets (Bird, 2005; Cain & Ram, 1998; Chandra & McFarland, 1997; P. F. Gao *et al.*, 2002; P. F. Gao *et al.*, 1999; S. R. Lee *et al.*, 2008; Y. J. Tang *et al.*, 2010). It has also been used for the medication studies of the human respiratory tracts (Broday & Georgopoulos, 2001; Darquenne, 2001; Darquenne & Paiva, 1996; Jayaraju et al., 2007; Ma & Lutchen, 2009; Mitsakou,

et al., 2005; Nowak et al., 2003; Park & Wexler, 2007; Rostami, 2009; Stapleton et al., 2000).

CFD contains numerically solving the Navier-Stokes equation that describes the conservation of the momentum and the energy in a fluid flow. Most practical flow fields include turbulence, in which case equations for modeling turbulence are resolved simultaneously. In numerical solutions, the most common information provided by a CFD simulation includes velocity, temperature and pressure profiles. As in the case of turbulent flow field, a CFD simulation delivers the flow field profile (for instance, time-averaged mean data) and turbulence properties such as turbulence kinetic energy and dissipation rate of turbulence. As mentioned earlier, the particle concentration is typically so low that the effect of particles on flow field itself is neglected. With the flow field information obtained, two major approaches could be used to confirm the particle transport and deposition: either the Lagrangian approach or the Eulerian approach.

With CFD packages applied today, CFD-based modeling is no longer a mere supplement of physical experiments. “Numerical experiments” could be carried out by properly validated CFD models, which is to provide sufficient information not yet available from physical measurements. However, it should be noted that CFD simulation of the aerosol transport and deposition should be “validated” with experimental results.

In the following sections, some of the general approaches and practical strategies of CFD modeling of aerosol transport and deposition would be described, which includes the basic theories in CFD-based modeling systems and applications.

1.2 Approach of CFD Modeling on Aerosol Transport and Deposition

Generally in numerical modeling process, the CFD-based simulation in the subject of the aerosol transport and deposition may include several major steps: (1) the flow field simulation, (2) the particle tracking, and (3) the post-processing to calculate the particle deposition. The following section would provide an instructive description on these strategies.

1.2.1 Model Definition and Flow Field Simulation

The geometry model could be built with any 2D or 3D design software. These geometric surfaces may be created through computer aided design (CAD) programs, in 2D or 3D form, or they may be produced from scans of real surface (Longest et al., 2009; Materialise, 2007; Rostami, 2009; Simpleware, 2007). The previous approach is widely used for large scale aerosol device which used for sampling; while the latter one is more likely applied in micro-scale or more complex flow passages such as human respirational system.

After the geometry model of any aerosol device is introduced, confirm of the computational domain (control volume in the flow case) is the first step of flow field simulation. The computational domain is defined as the spatial region in which the flow field and the particle transport/deposition are to be resolved (ANSYS, 2008), and numerically speaking, it would be 'bounded' by various types of wall surfaces (with no-slip flow boundary condition) or non-wall surfaces (e.g. in/out flow planes, symmetry or periodic planes). The wall surfaces are representing the physical geometric surfaces of

the devices or structures, with strict no-slip flow condition defined. The non-wall surfaces basically but entirely contain the inlets/outlets, symmetry planes, and surfaces with periodic boundary conditions. In CFD-based simulation process, both internal (control volume with real wall surfaces as boundaries) and external (control volume with non-wall surfaces as outer boundaries) flows would be involved in this kind of study, which might be referred to as a 'domain' or 'region' in CFD literatures.

The next critical step of flow field simulation is the mesh (or grid) generation. The defined control volume, e.g. the computation domain, is divided into discrete cells for simulation (ANSYS 2008). Normally, commercial CFD packages provide options for users to adjust the mesh generation parameters, such as the mesh shapes (e.g. prismatic, tetrahedral, or hexahedral), the growth ratio, etc. Generally speaking, higher resolution and smaller mesh size is required at locations where high flow property gradients exist, such as the near-wall region, boundary layers or near aerodynamic shocks. The mesh density and quality is actually an crucial criteria for the simulation outcome (Matida et al., 2004). The effect of mesh density is also intertwined with the choice of fluid dynamics models (Parker, et al., 2008). Specifically, the "grid convergence" must be achieved in flow field simulation, in other words, further refining of the mesh would not produce any better accuracy (Longest & Xi, 2007).

1.2.2 Flow Turbulence Modeling

Turbulence is a common phenomenon in aerosol flows, which suggests that some procedures of turbulence modeling is needed in aerosol simulations. It would cause

significant deviations in the aerosol transport and deposition simulation, if different turbulence models and wall treatments were employed (Matida *et al.*, 2003; Matida, et al., 2004; Y. Zhang *et al.*, 2004). Theoretically, turbulent flows can be designated with the unsteady Navier-Stokes equation. By resolving the unsteady Navier-Stokes equation within a given computational domain, the flow field information with its fluctuates could be obtained. Consequently, this flow field solution is a function of location and time. The above description is the governing conception of the direct numerical simulation (DNS), which is proposed to resolve all turbulent length scales. DNS is an approach without turbulence "modeling" but just "resolving". Its computational cost would increase with the Reynolds number as Re^3 (Pope, 2000). In most turbulent flow fields, simulation with DNS is excessively expensive, and therefore it is quite required for turbulence models in academic and industry applications.

In nowadays commercial CFD tools, the most widely used turbulence models are the Reynolds-Average Navier-Stokes (RANS) models. RANS models are established on the Reynolds momentum equations which are derived from the Reynolds decomposition and time averaging of the unsteady Navier-Stokes equation (Landau & Lifshits, 1987). Within these equations, the turbulent velocity fluctuations terms (also named as the Reynolds stress) are derived as additional unknown variables. These various kinds of RANS models have been built to solve the turbulence closure problem, including the k-ε, the k-ω, and the Reynolds stress transport models (RSM). The difference of these models mainly lies in the treatment of the Reynolds stresses (Launder et al., 1975; B. Launder & D. B. Spalding, 1974; B. E. Launder & D. B. Spalding, 1974; Wilcox, 2006).

In these models, mathematical relationships of these Reynolds stress terms must be identified to solve the turbulence flow field.

Another most well-known turbulent model is the large eddy simulation (LES). It is a strategy in which sub-grid scale models are used for the small scales of the turbulent flow, while the large eddies are simulated in a time-dependent manner (Pope, 2000). LES is proposed to resolve the largest and most important scales of turbulence, while modeling the smallest scales. Therefore, LES generally could get more accurate unsteady information compared to RANS model (requires more computational resources than RANS methods), and greatly decreasing the computational cost comparing to DNS.

1.2.3 Wall Functions and Treatments

The effect of flow-wall interaction would cause a serious challenge to turbulence modeling. In practical flow conditions, momentum parameters for the flow in one boundary layer may change more than an order of magnitude as turbulent mixing gives way to purely molecular transport at the wall. Thus a very fine mesh structure is needed in order to numerically resolve the transition within this near-wall flow. Typically, the criterion was raised to define this “sufficiently fine”, which required the cell Reynolds number (or the cell Peclet number) to be on the order of unity (B. Launder & D. B. Spalding, 1974). This would require extra computational resource and memory in a CFD-based numerical simulation and most likely result in a slow convergence. Furthermore, the turbulence models were designed to fit the flow with fully turbulent conditions, apparently without dominant wall effects. The technique solution for this

issue is to create a “bridge”, or so called “wall treatment” between the fully turbulence in the main flow region and the near-wall flow. Normally in commercial CFD packages, a number of wall treatments could be employed which have different requirements on the mesh resolution in the near-wall region (ANSYS, 2008). It should be noted that the choice of wall treatments could as well influence on the flow simulation and the particle tracking results, sometimes even in a significant way.

1.2.4 Aerosol Transport and Deposition Simulation

With the Lagrangian approach, Equation (1.2) was employed as the governing equation and individual trajectories of particles are tracked as they move through the control volume. In this case, a typical requirement is that the aerosol concentration is low and the particle-particle interaction needs to be negligible.

With the Eulerian approach, the particle mass or number concentration is treated as a scalar quantity, which is shown in the Eulerian transport equation (1.5). This scalar equation may be resolved simultaneously at the same time as the flow field simulation. It should be noted that the Eulerian approach is more appropriate used in aerosol cases for ultrafine particles compared to the Lagrangian modeling. And in the Eulerian method, the inertia is essentially negligible, but Brownian motion is significant.

Most aerosol flows are related to the turbulence, which significantly influences on the particle transport and deposition (Benjamin Y.H Liu & Agarwal, 1974). Normally, turbulent particle dispersion is simulated within the Lagrangian approach, by

using an instantaneous gas velocity in Equation (1.7) instead of the flow time-averaged velocity. The instantaneous gas velocity includes a fluctuating component **u'**:

$$\mathbf{u} = \bar{\mathbf{u}} + \mathbf{u}' \tag{1.7}$$

where $\bar{\mathbf{u}}$ is the time-averaged local velocity of the turbulent flow field. The fluctuation velocity **u'** is ensured to follow a Gaussian probability distribution with zero mean (Casella & Berger, 2002; Schobeiri, 2010). For isotropic RANS models (e.g. the k-ε and the k-ω models), the fluctuation velocity is:

$$\mathbf{u}' = 2\sqrt{k}\zeta \tag{1.8}$$

where k is the turbulence kinetic energy; ζ is a normally distributed random vector with a unity variance. The turbulence kinetic energy k would be obtained in the result of the turbulent flow field. For an anisotropic turbulence model such as RSM or LES, the fluctuation velocity will be anisotropic.

Within the Lagrangian tracking approach, some commercial CFD packages (such as ANSYS FLUENT) predicted the turbulent dispersion of particles by integrating the trajectory equations for individual particles, using the instantaneous fluid velocity as shown in Equation (1.7), along the particle path during the integration. By computing the trajectory in this manner for a sufficient number of representative particles, which could be controlled by user interface, the random effects of turbulence on the particle dispersion can be included.

The time interval over which the particle interacted with the randomly sampled velocity field was calculated followed. They suggested that it was associated with a turbulent eddy, in which case the interaction time was determined by one or the other of

the following two events: 1) the particle moved sufficiently slowly relative to the gas phase to remain within the eddy during the whole of its lifetime, or 2) the relative or "slip" velocity between the gas and particle was sufficient to allow it to traverse or cross the eddy in a transit/crossing time. The interaction time scale will therefore be the minimum of the above two. The commercial CFD package STAR-CCM+ (CD-adapco, London, UK) employed the turbulent dispersion based on Gosman and Ioanniedes's model (CD-adapco, 2008)(CD-adapco, 2008), assuming particle passing through a sequence of turbulent eddies as it traverses a turbulent flow field, with an eddy being a local disturbance to the Reynolds-averaged velocity field. The particle remained in the eddy until either the eddy time-scale was exceeded, or the separation between the particle and the eddy exceeds the eddy's length scale, which would be as recast as a term of eddy transit time (Longest & Xi, 2007).

In recent years, considering the potential errors when ignoring the particle turbulent dispersion effect in predicting trajectories, the commercial CFD packages developed models or approach to introduce the turbulent dispersion effect in particle tracking process. For example, ANSYS FLUENT models either a stochastic discrete-particle approach or a 'cloud' representation of a group of particles about a mean trajectory (ANSYS, 2008). In the stochastic tracking technique, stochastic tracking included the effect of turbulent velocity fluctuations on the particle trajectories using the discrete random walk model. The fluctuating velocity components were treated as discrete piecewise constant functions of time. Their random value would be kept constant over an interval of time given by the characteristic lifetime of the eddies. Also,

the momentum and mass defined for the injection would be divided evenly among the multiple particle/droplet tracks, and were thus spread out in terms of the interphase momentum, heat, and mass transfer calculations.

1.2.5 Pre- and Post-Processing

In the Lagrangian approach, an injection surface built in the geometric model is used to release particles to the domian. The shape, dimensions and location of this injector need to be defined so that it would be applicable to the physical condition. In most commercial CFD program, the conception of "parcel" is used as a sample particle injection point that may represent a number of particles released in the same conditions. The number of particle release points on the surface of the injector need to be sufficiently large, and usually uniform. The number of "real" particles simulated in the specific case, would depend upon the following parameters in CFD pre-setup: the number of injection points, the spatial distribution of the particle injection, and the particle mass flow rate respect to the injection surface. Once the Lagrangian particle tracking was carried out, particle trajectories were drew in the computational domain, based on which the particle deposition rate onto a specific surface (a solid wall or an outflow surface) would be obtained in pro-processing. With such information, one can readily calculate the fraction of deposition or penetration efficiency.

1.3 Examples of Aerosol Transport and Deposition Simulation

An important concern about hazardous aerosols, which might be potential threats in the environment, drew more and more attention nowadays. In order to achieve early detection and identification to prevent environmental threat, several effective aerosol devices are used for aerosol sampling, collection and identification, such as probes, inlets, channels/ducts, impactors, cyclones, and filters. In this section, literature review is carried out to evaluate some practical studies on CFD-based particle transport and deposition in such systems. Considering different shapes and dimensions of these applied aerosol devices, a number of particle transport and deposition mechanisms were actually involved in this part of study, including the inertial separation, the diffusion, the electrostatic effect, the interception and the turbulent dispersion.

1.3.1 Probes and Inlets

Sampling probes or inlets are generally used in ambient monitoring of environmental pollutants, perimeter monitoring of industrial and nuclear facilities, and global monitoring of radionuclides (B. Y. H. Liu & Pui, 1981; Mcfarland et al., 1992; McKinnon et al., 1998; Pleil et al., 1993; Witschger, 2000). Ambient aerosol sampling at high volumetric flow rates is generally an essential part and the first step towards proper agent detection. In order to achieve precise measurements, a demonstrative aerosol sample, which covered the pre-selected particle size range of interest, must be drawn through the probes or inlets into the particle identifying or collecting device in the next

level (Tang et al., 2010). Therefore, as the first component of the entire sampling system, the performance of the inlet is critical.

There are two major types of inlets used for aerosol sampling: the uni-directional and the omni-directional. Unidirectional inlets, such as shrouded probes (Chandra & McFarland, 1997), are more applicable to higher speed sampling applications, e.g., wind speeds greater than about 24 km/h (15 miles/h), as characterized by any source identifying systems where the direction of the aerosol flow is known (Bisgaard, 1995).

Gong et al. (Gong, et al., 1996) carried out numerical simulations of a shrouded probe, a device typically used for aerosol sampling in stacks. A finite element-based code FIDAP was used in this study for a 2D problem. The k-ε turbulence model was employed to simulate the flow field first, and the stochastic particle transport model was appled to track particle trajectories. In this study, several factors were considered to affect particle movements, including the drag effect, the gravity, the lift force, and turbulent dispersion. The study suggested that the penetration efficiency through the shrouded probe was well predicted with a difference of 5% compared to experiments. And the free stream velocity was one of the important operating conditions that may vary during the operation of a sampling probe. Based on this, Cain and Ram (Cain & Ram, 1998) presented the results of axisymmetric numerical simulation studies of turbulent airflow through a shrouded airborne aerosol sampling probe.

Omni-directional inlets on the other hand, are used extensively in the ambient air sampling where the aerosol flow direction is greatly variable and such a properly designed aerosol inlet should be able to sample independent of flow speed or coming

direction (P. F. Gao, et al., 1999). A typical omni-directional inlet used in the ambient environment includes three main components: an entrance section, an insect screen and a pre-separator. The entrance section generally has circumferential intakes that allow particles to be aspirated regardless of the wind direction (B. Y. H. Liu & Pui, 1981). It samples the horizontally directed aerosol flow, with any flow velocity and direction changes. The sampling flow would change to vertical direction and be adjusted to a fixed speed that corresponds to the sampling flow rate. The usage of the insect screen and pre-separator is to prevent large unwanted debris and particles from the size distributed sampling.

Ambient sampling introduces the challenge of sampling from an unknown direction, which is why omnidirectional inlets are usually suitable. Wedding and McFarland (Wedding *et al.*, 1977; Wedding *et al.*, 1980) developed the omni-directional inlet in modified Anderson air sampler. The Bell Shaped Inlet entrance section used in this study, which is referred to as BSI-e here in this study, is similar in design to an ambient aerosol sampling inlet developed by McFarland et al. (Mcfarland *et al.*, 1977). A conically-shaped connector was used to ensure the sampling status remain the same for various coming wind direction for all weather sampling. The inlet samples air via a narrow circular slit into a chamber-shaped section that turns the sampled flow from a horizontal to vertical direction, facilitating effective post-sampling analysis. Some experimental study was done for this cylindrical symmetry inlet, Wedding et al. (1980) used a variation of the BSI-e design in a PM-10 aerosol sampler, in which the inner shell was curved and outer shell was straight with no extended rim. Loss by inertial impaction

on the inner shell was studied in this research (Wedding, et al., 1980). Nene (Nene, 2006) and Baehl (Baehl, 2007) tested the BSI-e in a wind tunnel and determined the effects of wind speed and particle size on aerosol penetration. Nene (Nene, 2006) also developed a semi-empirical correlation for the BSI-e inlet that was based on his experimental data, however large deviations were existing in the lower wind speed case (2 km/h).

For other types of omni-directional aerosol sampling inlets, CFD simulations were carried out as a supplement to experiments. Gao et al. (P. F. Gao, et al., 1999) predicted aerosol penetration efficiency through an omni-directional aerosol inlet (an inverted funnel). A finite-element-based code, FIDAP 7.52 (Fluid Dynamics International, Inc., Evanston, IL) was used in their study. The computational domain comprised the flow fields inside and outside the inlet. The mesh structure consisted of over 50000 nodal points. The mesh density around and within the manifold sampler was set to be higher than that established in other regions of the flow field. Based on the flow field profile, particle trajectories were tracked, with the turbulent dispersion involved, which was considered by simulating along the velocity fluctuations obtained from a k-ε turbulence model. The computed penetration efficiency agreed well with experimental results for large particle sizes, but showed deviations of up to 10% for small particles.

In recent times, Lee et al.(Lee, Holsen et al. 2008) reported the development of a novel, large particle inlet (LPI) designed using CFD techniques. CFD code FLUENT was used at the design stage to achieve the optimal combination of geometrical and operational parameters, and the inlet sampled aerosol flow from various directions by a

narrow circular slit and a funnel shape section. Over 4 million grids were involved in simulations, and the RSM and the k-ε turbulence model was applied. While traditional inlets are designed to sample particles below 10 μm (PM10), the LPI was designed to accurately sample particles beyond 10 μm, over a wide range of wind velocities. Based on the numerical results, an empirical equation aiming for the penetration was developed in terms of a Stokes number.

1.3.2 Channels and Ducts

Particle deposition in channels and ducts would consider turbulence as an important factor. The famous experimental results in the research by Liu and Agarwal (Benjamin Y.H Liu & Agarwal, 1974) provided example and validation for CFD-based simulation on the turbulent effect on particle deposition in the internal flow. Parker et al. (Parker, et al., 2008) reproduced Liu and Agarwal's experiment in CFD simulation, based on the steady-state vertical pipe flow. ANSYS FLUENT software was applied in this research and the simulation was processed within a new 2-D geometric model. The turbulent flow field was simulated in RANS models (k-ε, k-ω and RSM), and based on which the Lagrangian particle tracking was followed to obtain aerosol deposition results. Besides different turbulent models, various near-wall mesh resolution (while keeping the grid's growth rate constant), and two kinds of wall treatments were applied in the simulation. It suggested that the different turbulence models, the mesh resolutions, and the wall treatments all had significant influences on the particle deposition rate. The RSM model could lead to a good agreement with experimental results, but still required

sufficiently high mesh resolutions, e.g. the wall-adjacent grids' y+ values in the order of unity. Meanwhile, using isotropic turbulence models (k-ε and k-ω) apparently over-predicted the near-wall turbulence kinetic energy gradient, thus caused a significant over-prediction of aerosol depositions.

Wang and Squires (Q. Wang & Squires, 1996) simulated the aerosol dispersion and deposition process in a fully-developed turbulent channel flow. LES was used for turbulence modeling and a maximum Reynolds number of about 80,000 was applied in this case with the incompressible Navier-Stokes. Both the drag and the lift effect regarded as the governing parameters, and the particle-particle interaction was neglected in this case. The DNS results obtained by McLaughlin (Mclaughlin, 1989) were refered to compare to this LES simulation, with a reasonable agreement, however both were below the experiment measured depositions (Benjamin Y.H Liu & Agarwal, 1974). The authors claimed that it probably was due to the neglect of the particle–particle interaction. Additionally, for very high Reynolds number, more complex wall treatments seemed to be required, because LES could only be applicable to simulate the particle-turbulence interactions in the outer flow.

Wang et al. (Q. Wang et al., 1997) accomplished simulations within turbulent boundary layers and studies on the particle depositions with both DNS and LES approaches. The Saffman lift force (Saffman, 1965) was involved in their model and the effect on deposition was examined: it would apparently over-predict the dependence of the deposition velocity on the particle relaxation time. Based on this result, an 'optimum' lift force, in terms of the shear-induced lift components, was developed and represented

the lift force acting on a particle in a near-wall shear flow. It should be noted that this term generated a dependent relationship between the deposition velocity and the particle relaxation time. It suggested as well that LES results could provide a better agreement after introducing this optimum force, compared with experimental measurements (Benjamin Y.H Liu & Agarwal, 1974).

Kuerten and Vreman (Kuerten & Vreman, 2005) studied the particle-laden turbulent flow in a channel. Both DNS and LES models were applied in this numerical experiment. The simulation showed that turbophoresis could significantly cause an accumulation of particles in the near-wall region. Through incorporating an inverse filtration model, the LES results reduced the turbulent effect in particle motion. A good agreement was observed between LES and DNS cases, and based on which the authors indicates that the prediction of the Lagrangian particle tracking in LES modeling could be accurate as well.

1.3.3 Real and Virtual Impactors

An impactor is one kind of widely-used collecting device, which captures particles by inertial impaction. It could also be used to evaluate the size distribution of aerosol particles or produce concentrated aerosols (Hinds, 1999).

Vinchurkar et al. (Vinchurkar, et al., 2009) developed the Mark II Andersen cascade impactor (ACI) model using CFD tools and based on which the effect of electrical charge on particle deposition was evaluated. The commercial CFD code ANSYS FLUENT was used for modeling in this study. From 0.8 to 2.5 million grids

were generated for each impactor stage, in order to simulate the internal flow. The incompressible laminar and transitional models (Low Reynolds number (LRN) k-ω model) were used for the flow field simulation, and then particle trajectories were simulated using that Lagrangian tracking approach. In this study, the effects of impaction, sedimentation, diffusion, and electrostatic attraction were considered to track the particles. The CFD-based predicted cut-off diameters for each ACI stage were found to be within 10% difference from the published experimental data. This study showed that CFD is capable to evaluate the effects acting on particle deposition, which might not be readily available from experiments.

1.3.4 Cyclones

Cyclones are commonly used to collect aerosol particles through inertial separation (Hinds, 1999). Generally, complex and turbulent flows would occur in the cyclone, which indicates that the choice of turbulent models significantly affect the accuracy of the flow field simulations.

Gimbun et al. (Gimbun, et al., 2005) evaluated the effects of cone tip diameter on the collection efficiency of gas cyclones, using the commercial program FLUENT 6.1. The RSM turbulent model was applied in this study to get flow fields prediction, and then the Lagrangian approach was used to predict the particle trajectories and deposition pattern. Development was applied to create a high density mesh near the cyclone cone, in order to get a probably better prediction on the effect of cone tip diameter to the collection efficiency. Compared to published experimental data, deviations up to 5.5%

was found with CFD simulations in predicting the cyclone collection efficiency for different cone dimensions. The authors indicated that the RSM turbulence model would be a feasible and effective method for modeling the collecting performance of gas cyclones.

The bioaerosol collection in a wetted wall cyclone was evaluated by Hu and McFarland (Hu & McFarland, 2007) using FLUENT, and the particle deposition pattern was estimated. Approximately 1.1 million grids were generated in the computational domain inside the cyclone. Sufficiently fine wall-adjacent cell prism layers were built for intended accurate simulation of velocity boundary layer. Also, the RSM turbulent model was employed for the flow field simulation and the Lagrangian particle tracking was used to determine particle deposition rate and most importantly, the particle collection efficiency of the cyclone. The simulations revealed that the stream-tubes experienced significant narrowing and an inward displacement as the airflow traveled down the axis of cyclone. The CFD-derived collection efficiency of the cyclone showed an excellent agreement with the published experimental data. The CFD-based study provided important information on the particle deposition locations, which would be difficult to obtain in experiments, but useful as introducing modifications into future upgraded versions of the wetted wall cyclone.

1.3.5 Filters

Filtration is an effective and widely applied method for removing particles from air flows (Deuschle, et al., 2008). Fibrous filters are the most common type of filters. In

filtration there are several basic mechanisms by which an aerosol particle can be deposited onto a fiber in a filter or in a screen including the inertial impaction, the interception, the diffusion, the gravitational settling and the electrostatic effect. Among these mechanisms, impaction is arguably the most important deposition mechanism for micrometer-sized particles (Hinds, 1999). However, the other mechanisms cannot be neglected, especially the interception effect when the particle diameter is large relative to the characteristical length of the filtration device (usually the diameter of the fiber) (J. Wang & Pui, 2009). CFD studies of filtration typically involved simulating particle deposition on fibers (J. Wang & Pui, 2009).

Particle deposition by interception occurs when the center of a particle follows a trajectory that would come within one particle radius of the surface or a fiber or wire. In contrast, impaction occurs when the center of a particle follows a trajectory that would directly hit the surface of the fiber or wire (Hinds, 1999). The theoretical analysis of particle deposition by interception has been based on a boundary layer approach using the Kuwabara-Happel flow field (Happel, 1959; Kuwabara, 1959). The Kuwabara-Happel flow field is based on the solution of the Navier-Stokes equation for the case of viscous flow around a cylinder by the use of the so-called cell model, which could provide a reasonable representation of the flow around fibers and is widely used in theoretical filtration analyses (Kirsch & Stechkina, 1978; K. W. Lee & Liu, 1982; Yeh & Liu, 1974). Various empirical correlations for particle deposition by interception have been developed (K. W. Lee & Gieseke, 1980; K. W. Lee & Liu, 1982; K. W. Lee & Ramamurthi, 1993; B. Y. H. Liu & Rubow, 1990; Pich, 1966). These correlations

typically use a dimensionless parameter called the interception parameter, R, which is defined as the ratio of particle diameter d_p to fiber/wire diameter d_f: (Hinds, 1999)

$$R = \frac{d_p}{d_f} \tag{1.9}$$

A number of researchers have used Computational Fluid Dynamics (CFD) to model aerosol flow fields in filtration systems. Liu (Z. Liu, 1993) simulated the gas flow through arrays of circular fibers in CFD method, with filtration efficiency computed. Tronville and Rivers (Tronville & Rivers, 2005) numerically modeled the flow resistance of fibrous filter media with random fiber diameters. Deuschle et al. (Deuschle, et al., 2008) presented an experimentally validated CFD model describing filtration, regeneration and deposit rearrangement effects. However, in commercial CFD packages, the standard Lagrangian particle tracking module does not account for the interception effect. They treat particles as mass points; the particle size is only used for calculating the aerodynamic drag force. This deficiency would not cause noticeable consequences if interception were an insignificant mechanism for particle deposition. However, for a filtration process such as a fibrous filter or screen, overlooking the interception events could cause considerable errors for modeling and prediction (Fotovati et al., 2010; Kasper et al., 2009).

Wang and Pui (J. Wang & Pui, 2009) created a 2D model for the nano-particle deposition simulation on elliptical fibers. In this research, ANSYS FLUENT was used and the near-fiber mesh grids were refined with the cell size gradually growing as the distance away from the fiber surface. Considering the low Reynolds number flow

condition, only laminar viscous model was employed in this simulation. Afterwards, the Lagrangian method was used to predict the particle transport and deposition, and the effects of between-fiber distance on collection rate were examined. To count for the intercepted particles, C++ subroutines in FLUENT modeling were written.

Similarly, a 3D electrospun nano-fibrous materials model was built by Hosseini and Tafreshi (S. A. Hosseini & Tafreshi, 2010), which contained resembling of the internal microstructure. FLUENT was used to simulate the pressure drop and the filter collection efficiency using both the Lagrangian and the Eulerian methods. Tetrahedral cells were used in volume mesh generation and higher mesh density was close to the fiber surfaces. In a low Reynolds number case, the aerosol flow through this filtration system was assumed to be laminar and at a steady state. Particle collection due to interception and Brownian diffusion, as well as the slip effect at the surface of nano-fibers, has been combined in FLUENT environment by developing customized user defined function. The results showed that the particle collection efficiency and pressure drop had good agreements compared with analytical/empirical results from the literature (K. W. Lee & Gieseke, 1980; K. W. Lee & Liu, 1982; K. W. Lee & Ramamurthi, 1993; B. Y. H. Liu & Rubow, 1990; Pich, 1966).

1.3.6 Turbulent Dispersion of Aerosols

Turbulence can cause aerosol particles to deposit on walls. In some scenarios, turbulent transport may become the dominant mechanism of particle deposition. Therefore particle deposition due to turbulence, or turbulent deposition, has long been a

topic of interest in aerosol research. In a turbulent flow, particles interact with eddies (local fluctuations of the gas flow); as a result, the particles exhibit motion relative to the time-averaged mean gas flow. This motion leads particle transport and deposition at the wall. Experimental studies of turbulent deposition of aerosol particles have been carried out by many researchers (Friedlander & Johnstone, 1957; Benjamin Y.H Liu & Agarwal, 1974; Papavergos & Hedley, 1984). Based on these experiments, empirical relations have been developed for quantifying turbulent deposition in pipe flows.

A two-stage process theory was provided to describe the turbulent aerosol deposition (Papavergos & Hedley, 1984). The first stage of turbulent effect on deposition involved transport within the turbulent core region turbulent eddies, resulting in an approximately uniform concentration profile in the turbulent core region of the developed flow. In the second stage, particle reaches the near-wall viscous sub-layer, where the turbulent fluctuating component reduced from the core region. Normally, particles with sufficient inertia could move towards the wall and deposit, the rate of which would depend on particle relaxation time. Apparently, turbulent deposition mechanism would significantly influenced by the aerosol behavior within this second stage, which depended on particle relaxation time and turbulent fluctuating gradient, in another word, turbophoresis.

Empirical relations of turbulent deposition are typically presented in terms of the dimensionless particle relaxation time τ_+ and the dimensionless deposition velocity V_+. The dimensionless particle relaxation time is based on the particle relaxation time (Hinds, 1999). For a spherical particle, the particle relaxation time is defined as:

$$\tau = \frac{\rho_p d_p^2 C_c}{18\mu} \tag{1.10}$$

where ρ_p is the particle density, d_p is the particle diameter, C_c is the Cunningham slip correction factor (defined in Equation 1.4), and μ is the dynamic viscosity of the fluid. The dimensionless particle relaxation time is then defined as:

$$\tau_+ = \tau \frac{u_*^2}{\nu} \tag{1.11}$$

where u_* is the friction velocity (Landau & Lifshits, 1987), and ν is the kinematic viscosity.

The deposition velocity, V_{dep}, is the effective velocity which particles travel to a surface and is analogous to the settling velocity for deposition by settling (Hinds, 1999). It is defined as:

$$V_{dep} = \frac{J}{C_{p0}} \tag{1.12}$$

Where J is the deposition flux (the number of particles deposited per unit surface area and per unit time), and C_{p0} is the undisturbed aerosol concentration (the number of particles per unit volume). Apparently, this term of deposition velocity could represent the particle deposition rate in respect to any surfaces.

The dimensionless deposition velocity V_+ is the ratio of the deposition velocity V_{dep} to the friction velocity (K. W. Lee & Gieseke, 1994; Benjamin Y.H Liu & Agarwal, 1974):

$$V_+ = \frac{V_{dep}}{u_*} \tag{1.13}$$

For turbulent pipe flows experimental studies have revealed some general correlations, typically presented in terms of the dimensionless particle relaxation time τ_+ and the dimensionless particle deposition velocity V_+ (K. W. Lee & Gieseke, 1994; Benjamin Y.H Liu & Agarwal, 1974). These correlations may be summarized as follows (Guha, 1997, 2008):

- Regime I ($\tau_+ < 0.3$): Particles follow the flow almost perfectly; deposition is dominated by Brownian motion; deposition velocity V_+ decreases as τ_+ increases; may be described with a turbulent version of Fick's law of diffusion.
- Regime II ($0.3 < \tau_+ < 30$): Particle "slip" relative to the flow is significant, and particle motion is strongly affected by turbulent fluctuation; deposition velocity V_+ increases as the second order of τ_+ (or as the fourth order of the particle size).
- Regime III ($\tau_+ > 30$): Particles have large inertia and the effect of turbulence on particle motion is significantly reduced; deposition velocity V_+ decreases with increasing particle size.

With review on many previous studies giving experimental measurements of the deposition velocity, Guha (Guha, 2008) also provided the data illustrated the basic characteristics for the dimensionless deposition velocity, which is shown in Figure 1.1.

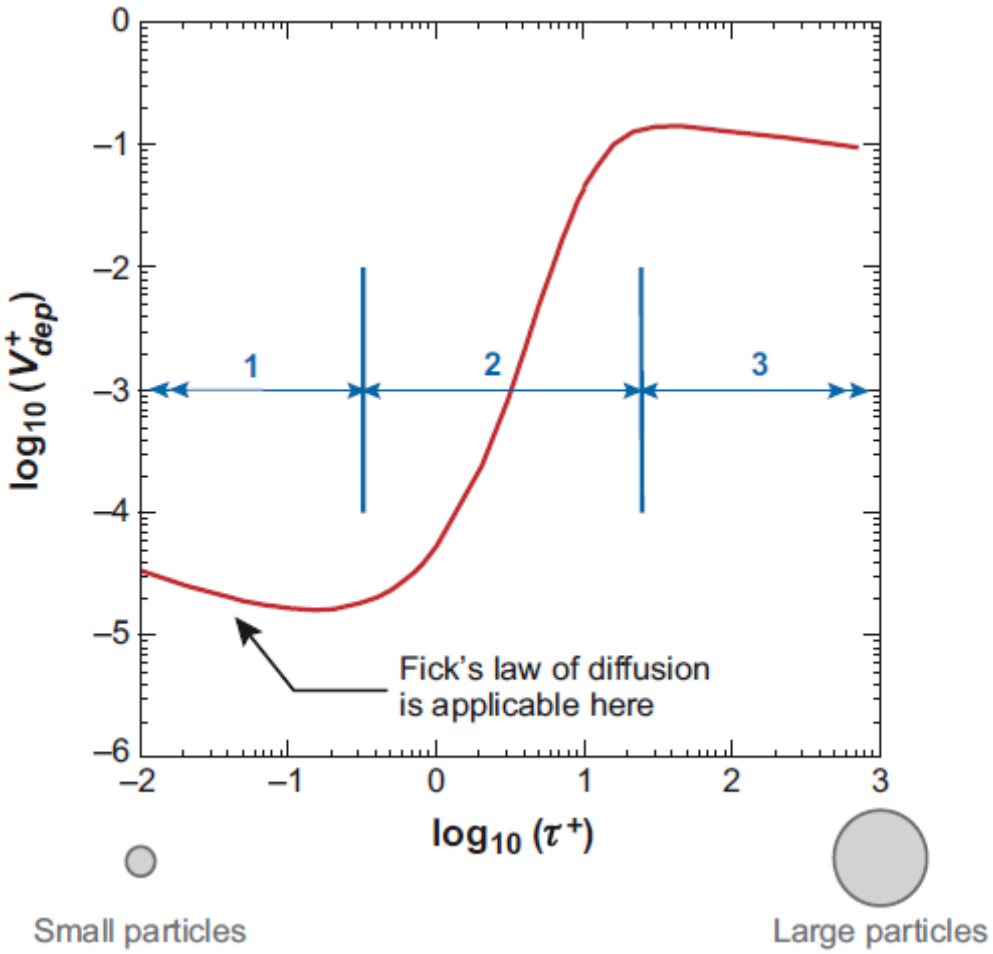

Figure 1.1 A typical variation in measured deposition rate with particle relaxation time in fully developed vertical pipe flow. Regime 1, turbulent diffusion; regime 2, turbulent diffusion-eddy impaction; regime 3, particle inertia moderated. (Guha, 2008).

Capability of simulating turbulent transport and deposition is available in most major commercial CFD packages. The simulation is typically realized with the Lagrangian approach, in which the motion of individual particles is simulated taking into account the particle-eddy interaction (Tang & Guo, 2011). The characteristics of eddies are derived from simulation results of the turbulent flow, which are strongly dependent

on the turbulence model selected. The turbulent transport models in commercially CFD packages are validated with special cases, which may not be relevant to turbulent deposition of aerosol particles. Therefore, to use CFD for solving turbulent deposition problems, one needs CFD methods (including criterion for model selection and mesh resolution) that are validated for the specific purpose.

To obtain validated CFD methods, a natural approach is to first simulate turbulent deposition in pipe flow scenarios, for which experimental data are available to validate the CFD methods; then the validated CFD methods may be extended to more complex flows. Parker et al (Parker, et al., 2008) carried out CFD simulation of turbulent deposition in turbulent pipe flows, with ANSYS FLUENT software, and compared against the experimental study of Liu and Agarwal. They found the turbulence model and the near-wall mesh resolution to be the two most important parameters. The Reynolds stress turbulence model produced the best accuracy, while the mesh resolution had to be sufficiently fine so that the y+ value of the wall-adjacent cells was on the order of 1. Drobyshevsky et al. (Drobyshevsky et al., 2009) developed a so-called Diffusion-Inertia Model for calculating aerosol particle deposition from turbulent flows, with the open-source CFD code OpenFOAM. The model was targeting the simulation of aerosol diffusion and turbophoresis deposition mechanisms. Deposition of particles in a turbulent flow was considered for cases of a straight vertical pipe and for a 90° bend in which the turbophoresis was coupled with centrifugal forces. Even based on a coarser mesh scenario ($y_{+}>30$), the calculation results from the new introduced model showed good agreement with experimental data.

Guha (Guha, 1997, 2008) has proposed an Eulerian description of particle transport in turbulent flow. This analytical description includes turbophoresis, i.e. particle transport due to gradient in turbulent velocity fluctuation; it also includes other mechanisms of particle transport such as thermophoresis, shear-induced lift force, electrical forces, and gravitational effects. A Cartesian coordinate system is adopted in Guha's formulation, with the x axis in the direction of the flow and the y axis perpendicular to the wall. The particle convective velocity perpendicular to the wall (i.e. the deposition velocity), $\overline{V_{py}^{c}}$, is given in the following particle momentum equation:

$$\overline{V_{py}^{c}}\frac{d}{dy}\left(\overline{V_{py}^{c}}\right)+\frac{\overline{V_{py}^{c}}}{\tau_I}=-\frac{d}{dy}\left(\overline{V_{py}'^{2}}\right)+F_y \tag{1.14}$$

where τ_I is the particle inertial relaxation time, defined as:

$$\tau_I=\tau\frac{24}{\mathbf{Re}_s\,C_D}C_c \tag{1.15}$$

where τ is the particle relaxation time, and C_c is the Cunningham correction factor; C_D is the drag factor, which is a function of slip Reynolds number Re_s, given by the following empirical relation (Clift *et al.*, 1978). For small particles and low "slip" velocity between the particle and the gas flow, τ and τ_I are essentially equal.

$$C_D=\frac{24}{\mathbf{Re}_s}\left(1+0.15\,\mathbf{Re}_s^{\,0.687}\right) \tag{1.16}$$

The term F_y is the y-component of forces acting on the particles, such as shear-induced lift force or electrical force. The term $\overline{V_{py}'^{2}}$ is the mean square velocity

fluctuation of the particles in the y (wall-normal) direction, and the term $-\frac{d}{dy}\left(\overline{V'^2_{py}}\right)$ represents the turbophoresis effect. In general, the particle mean square velocity fluctuation $\overline{V'^2_{py}}$ is not the same as the mean square velocity fluctuation of the gas flow $\overline{V'^2_{fy}}$. This theoretical description of turbulent deposition was used in post-processing of the simulation results in this study, as described in the following section.

1.4 Research Scope and Objective

In this dissertation work, different particle transport and deposition mechanisms are studied through CFD modeling approach, including particle inertial impaction, gravitational effect, lift force, interception, and most importantly, turbophoresis. These mechanisms were examined within different practical applications, which included aerosol sampling inlet (inertia impaction, gravitational settling, lift force, turbulent dispersion), filtration system (interception) and vertical flow channels (turbophoresis). Basically two widely-used commercial CFD packages, ANSYS FLUENT (ANSYS Inc., Canonsburg, PA) and STAR-CCM+ (CD-adapco, London, UK) are applied in the CFD simulation of this study. According to the specific flow conditions, different flow viscous models were used to predict the flow field, then the Lagrangian particle tracking approach was applied to identify the particle trajectories and deposition rate.

The objective of this research is to get a better understanding and quantitative estimation on the basic mechanisms that would influence on particle transport and deposition, and evaluate the feasibility and accuracy of using commercial CFD tools in

predicting performance of aerosol sampling. Some of the published experimental data or the empirical equations were used in validating the CFD predications.

2. METHODOLOGY *

For this doctoral dissertation study, performance of CFD tools in predicting aerosol transport and deposition was evaluate through three major models, for different focus on particle mechanisms. The CFD simulation was carried out for Bell-Shaped aerosol Inlet (BSI) efficiency study, the electroform screen model in filtration system and turbulent deposition model in a vertical straight pipe. Various aerosol deposition mechanisms, such as particle inertial impaction, gravitational effect, lift force, interception, and turbophoresis, were discussed through CFD approach based on these simulations. And the method details were described as follows, including the ways to build the geometric model (identify the computational domain), to generate the mesh grids, choices of CFD simulation parameters (flow viscous models, boundary conditions, wall functions, etc.), and finally the post-processing and analysis methods.

2.1 Aerosol Deposition on Bell-Shaped Aerosol Inlet

In this study, CFD approach was applied to carry out flow field simulations and the Lagrangian particle tracking for the entrance section of a 100 L/min omni-directional Bell-Shaped Inlet. Neither an insect screen nor a large-particle pre-separator was

---

*Reprinted with permission from "A Computational Fluid Dynamics Study of Particle Penetration through an Omni-Directional Aerosol Inlet" by Tang, Y.J., Guo, B., & McFarland, A.R. 2010. *Aerosol Science and Technology*, 44, 1049-1057, Copyright [2012] by TAYLOR & FRANCIS INFORMA UK LTD – JOURNALS.

included with the inlet. For environmental wind speeds of 2, 8, and 24 km/h, the penetration efficiency was examined through the inlet which was mainly associated with flow that enters the intake region. Penetration efficiency and the regional particle deposition were generally predicted in CFD method with this study.

2.1.1 Inlet Design and Wind Tunnel Testing

CFD approach was used to study the aerosol penetration efficiency through the entrance section of a bell-shaped omni-directional inlet (BSI-e). The flow field simulation were carried out for free wind speeds of 2, 8 and 24 km/h and a fixed exhaust flow rate of 100 L/min; and the Lagrangian particle tracking was performed for 2 to 20 μm aerodynamic diameter particles to study the inlet penetration and the regional deposition pattern.

The BSI-e, the inlet model shown in Figure 2.1 (a) and (b), is comprised of three major components, i.e. the outer shell, the inner shell, and the exhaust tube. For the device studied here in this study, which is designed to provide accommodations of a fixed flow rate of 100 L/min, the heights of the inner and outer shells are approximately 172 mm and 150 mm, respectively. The radial distance between the cylindrically shaped sections of the two shells is approximately 13 mm.

The wind tunnel experiments from two previous works, Nene (Nene, 2006) and Baehl (Baehl, 2007), with the 100 L/min BSI-e were carried out at the free wind speeds of 2, 8, and 24 km/h (0.56, 2.22, and 6.67 m/s) and with particle sizes differed from 5 to 20 μm aerodynamic diameter. The particle penetration efficiency, which used to evaluate

the aerosol inlet performance in industry, was defined as the ratio of the mean aerosol concentration at the exit of the exhaust tube of the BSI-e, $C_{f,exhaust}$, to the mean aerosol concentration in the uniform free stream, $C_{f,free}$:

$$P = \frac{C_{f,exhaust}}{C_{f,free}} \tag{2.1}$$

Experimental practices for indentifying $C_{f,exhaust}$ and $C_{f,free}$ are described in details by Nene (Nene, 2006) and Baehl (Baehl, 2007).

2.1.2 Computation Domain and Boundary Conditions

In this CFD study, a box-shaped computational domain, as shown in Figure 2.1(c), with length, width, and height dimensions of 1.07m × 0.53m × 0.53m, was developed using CFD modeling software GAMBIT 2.2.30 (ANSYS, Inc., Canonsburg, PA). A numerical model of the BSI-e was built and placed in the center of the box with the top of the outer shell a distance of 178 mm from the top of the computation domain, and with the exit plane of the exhaust tube connected with the bottom of this computation domain.

The dimensions of the computation domain were selected to be sufficiently large to avoid excessive flow blockage in the simulated flow field. Relative sensitivity analysis (S. R. Lee, et al., 2008) was carried out for different heights and widths to ensure that the velocity near the lateral boundaries did not exceed 110% of the free stream air velocity (see appendix A).

For the boundary conditions, the inlet flow surface of the computation domain was set to have a uniform velocity boundary condition (velocity inlet boundary), with a fixed pressure of 101 kPa. The boundary condition of the top, bottom and the lateral surfaces of the box domain were set to be symmetry planes (no shear at surface); the exhaust tube of the BSI-e model was set to be 'outflow' boundary, and it ensured a fixed volumetric flow rate of 100 L/min through by adjusting the split ratio of the two outlet surfaces (the BSI outlet and the domain outlet), with a given free wind speed; and the domain outlet boundary was also set to be an 'outflow' surface, i.e. a boundary with a specified volumetric flow rate.

Gambit 2.2.30 software was as well used in this case for mesh generation, after building of this geometric model. First surface meshes were generated, with the weighting ratio and the spacing factor which were set to allow for finer mesh stuctures in regions with expected greater velocity gradients. Afterwards, 3D volume meshes were built based on surface meshes and the tetrahedron and prism boundary layer meshes were employed. High-resolution gridding in regions of possible large velocity gradients (e.g., near the rims of the shells) was applied.

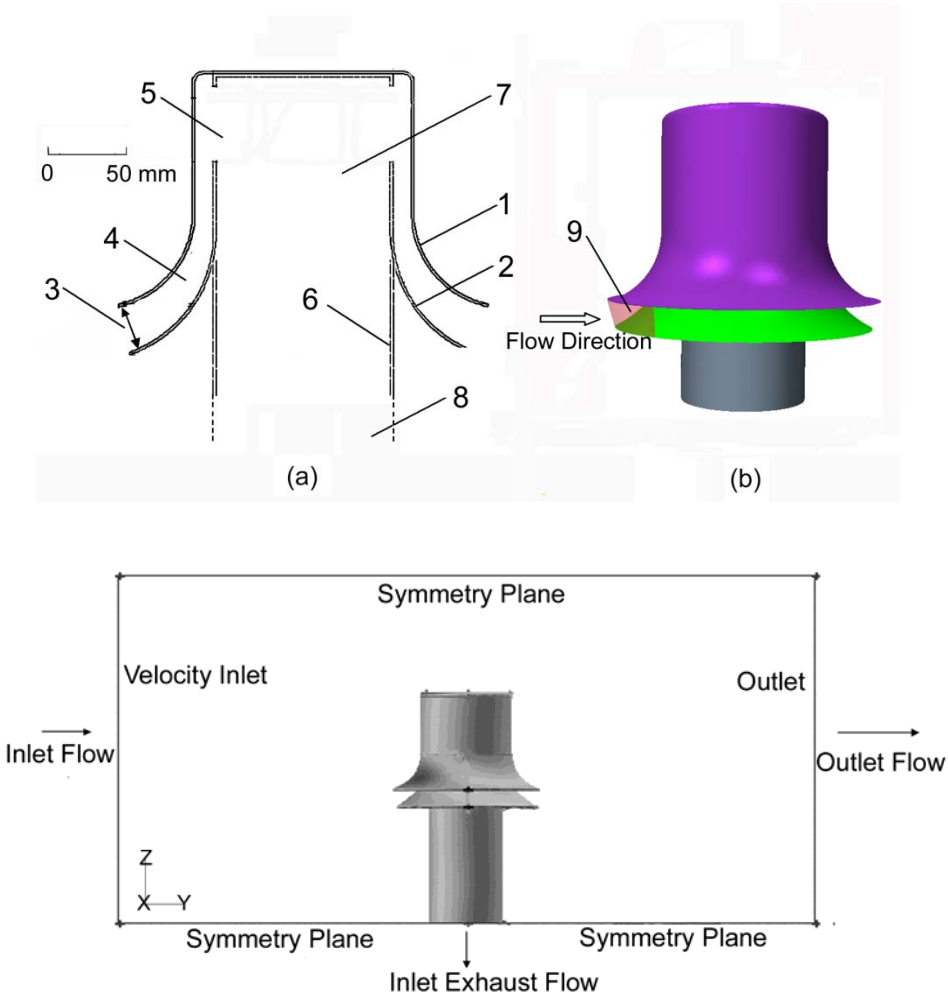

(c)

Figure 2.1 (a) Cross-sectional view of the 100 L/min Bell-Shaped Inlet entrance section (BSI-e). In the figure: 1. Outer shell; 2. Inner shell; 3. Intake gap; 4. Between-shell passage; 5.Windows; 6. Exhaust tube; 7. Entrance of the exhaust tube; 8. Exit plane of exhaust tube; 9. Intake surface (facing the wind). (b) A 3-D view of the BSI-e. (c) Schematic of the computational domain used in numerical simulations. Boundary conditions: Inlet surface of the domain—"Velocity Inlet" (with velocity of wind speed); Lateral surfaces of the domain—"Symmetric"; Outlet surface of exhaust tube and domain—"Outflow" (with outlet flow rate of 100 L/min at exhaust tube); Surfaces of BSI-e—"Wall" (Tang et al. 2010).

Mesh size sensitivity was tested by evaluating the difference in the velocity profile at high velocity-gradient locations when the mesh density was doubled. The final mesh density was sufficiently high such that the flow field results were unaffected by further mesh density increase (with less than 1% change in velocity when the mesh density was doubled). Overall, approximately 4.5 million cells were generated in the computational domain. The minimum cell volume was $1.88\times10^{-10}m^3$ and the maximum cell volume was $1.01\times10^{-6}m^3$, which were approximately the same as those volumes of 0.6 mm and 10 mm cubes.

2.1.3 Turbulence Model

In this case, the usage of a turbulence model in the CFD modeling was necessary because the Reynolds number based on the gap width of the intake section could be as high as 5,000 in the case of the free wind speed 24 km/h. Thus, the Reynolds Stress Model (RSM) was applied for the BSI-e simulations.

A 5% of the turbulence intensity on the inlet boundary of the computational domain was set before iterations, which was based on the previous wind tunnel experiments (S. R. Lee, et al., 2008). The mass and momentum equations were solved using a finite volume approach with double precision, and the numerical convergence criterion for continuity calculations was set at $\sim10^{-6}$. The flow field simulations were run until all the momentum residuals within the computational domain were almost unchanged within the next 100 additional iterations.

After the flow field simulation in the computation domain was convergent, the Lagrangian particle tracking method was carried out. The Discrete Phase model (DPM) and Particle Tracks module of the FLUENT program was functioned to simulate for this purpose, with assumed no particle-flow interaction. Considering the turbulence effect on both flows and particles, the turbulent dispersion was carried out using the Stochastic Tracking model in FLUENT. The turbulent dispersion of particles was calculated using the instantaneous fluid velocity (shown in Equation 1.7) obtained from the flow field simulation. In each particle injection point on the domain inlet surface, 100 parcels (particle releasing attempts) were processed for the turbulence dispersion with randomness. Time-dependent fluctuating velocity components were calculated based on the characteristic lifetime of eddies.

The particle number concentration in the wind tunnel experiments of Nene and Baehl (Baehl, 2007; Nene, 2006) was approximate to be about 10^9 particle per m^3. For such aerosol concentration levels, the Brownian motion and the kinematic coagulation should be both negligible (Hinds, 1999). Therefore, particle-particle interactions were neglected in CFD package here. Particles with a density of 1,000 kg/m^3 and one specified diameter were released from uniformly distributed locations on the inlet surface of the computation domain. The attachment coefficient for particles on any walls was set to be unity, i.e. no particle bounce allowed on the wall, and all the particles would be stuck once impaction occurred which ended this particle trajectory. Futhermore, the drag force, gravitational effect and the Saffman lift force were considered in this numerical model through FLUENT momentum settings.

2.1.4 Calculation of CFD-Based Penetration and Regional Deposition

The most critical judge on the efficacy and feasibility of the CFD simulations was to compare the CFD-derived particle penetration efficiency with the experimentally measured results. In terms of the post-processing calculation, the physical definition of particle penetration as given in Equation (2.1) can be expressed as:

$$P_{sim} = \frac{n_{exhaust} / Q_{exhaust}}{n_{total} / Q_{total}} \tag{2.2}$$

where $n_{exhaust}$ is the number of particles which exited the computation domain through the exhaust tube outlet as determined by particle tracking process; n_{total} is the total number of particles released to this domain in tracking; $Q_{exhaust}$ is the volumetric airflow rate through the exhaust tube (fixed aerosol sample flow rate, 100 L/min in this case); and Q_{total} is the total volumetric airflow rate through the inlet surface of the computation domain, which could be calculated by the uniform environmental velocity, i.e. the free wind speed. In the simulation the particles were released homogeneously and uniformly over the entire inlet surface.

A root-mean-square normalized error, e_{rms}, for the relative deviation between the CFD-derived and experimental penetration efficiency results can be evaluated from:

$$e_{rms} = \sqrt{\frac{1}{n}\sum_{i=1}^{n}\frac{\left(P_{\exp,i} - P_{num,i}\right)^2}{P_{\exp,i}^2}} \tag{2.3}$$

where n is the number of the experimental data pairs for penetration; $P_{\exp,i}$ is the the experimentally measured penetration for the i^{th} experimental condition (the specific case

of the particle size and the free wind speed); and, $P_{num,i}$ is the CFD-derived penetration for the same i^{th} condition. In this calculation, $P_{num,i}$ took the CFD value if a simulation was run exactly at the i^{th} condition; however, if CFD simulation for the i^{th} condition was not available, then $P_{num,i}$ was obtained from a spline curve generated from the CFD-based penetration results, which were processed and obtained by OriginPro 7.5 software (OriginLab Corporation, Northampton, MA).

The CFD results were as well used to determine the regional particle deposition pattern within the BSI-e device, which was relevant to particle penetrations through the inlet. It could be used to develop the correlations between the penetration and other mechanisms causing deposition. After the tracking particle trajectories with the Lagrangian method, FLUENT would provide the terminal coordinates of particle trajectories for deposited particles. MatLab 2008a (The MathWorks, Inc., Natick, MA) was then applied to plot 3D map of these deposited locations. The CFD results of regional deposition could not be compared with experimental data, as the latter one was not available.

Aspiration efficiency is a commonly used term to evaluate the performance of unidirectional sampling probes (Belyaev & Levin, 1974). In this case of BSI-e, the aspiration efficiency was defined as the ratio of two particle concentrations: one concentration in the intake surface (Figure 2.1(b)); the other concentration in the uniform free stream. The intake surface is where the aerosol flow enters the BSI-e between the rims of the two shells, and is technically defined as a portion of the circumferential entrance surface that is bound by the rims of the shells, forming a 60˚ azimuthal angle

about the axis of the BSI-e, and symmetric with respect to the free stream velocity on the upwind side of the BSI-e (see the figure on page 81 in top view). Based on particle tracking results, approximately only the aerosol flow that moved through the intake surface was capable to reach in the exhaust tube, i.e. being sampled. Howerve in this level, note that experiments could be difficult to measure this aspiration efficiency, P_1. Meanwhile, P_1 could be simulated based on CFD simulation using the following equation:

$$P_1 = \frac{n_{\text{intake}} / Q_{\text{intake}}}{n_{total} / Q_{total}} \tag{2.4}$$

where n_{intake} is the number of particles that pass through on the intake region; and, Q_{intake} is the volumetric airflow rate through the intake region.

Another two penetration were defined here as supplements. The penetration through the between-shell passage, P_2, was calculated from:

$$P_2 = \frac{n_{dp} / Q_{exhaust}}{n_{\text{intake}} / Q_{\text{intake}}} \tag{2.5}$$

where n_{dp} is the number of particles that reach the entrance plane of the exhaust tube.

The flow rate through the exhaust tube was constant, so the penetration through tube, P_3, could be calculated using the following equation:

$$P_3 = \frac{n_{exhaust}}{n_{dp}} \tag{2.6}$$

Note that the flow rate through the exhaust tube should be constant (100 L/min), and the device penetration efficiency is actually the production of P_1, P_2 and P_3. The independent variables in Equations (2.4)~(2.6) were calculated from CFD simulation

results, with the particle index through defined surfaces or boundaries in the Lagrangian particle tracking results.

2.2 CFD Prediction of Interception in a Filter

When the trajectory of a spherical particle's center comes within one particle radius of a solid surface, the particle will be captured on the surface because of its finite size (Hinds, 1999). This mechanism of particle capture is referred as interception. Typically for most cases, interception effect could be neglected in predicting particle deposition, e.g. the BSI-e case mentioned earlier, because the particle would be too small compared to the characteristic dimension of the flow channel. However in some other cases, interception could be a very important mechanism of particle deposition, especially when the particle size is large relative to the characteristic length of the target device (e.g. fiber or wire diameter within a filter). However it should be noted that, in most of commercial CFD packages, the standard Lagrangian particle tracking module does not technically account for this interception effect. Instead, particles are treated as mass points when they travel in the domain, and the only use of the particle size is to derive the drag force acting on itself. This deficiency of neglecting interception normally would not cause serious consequences as in those cases the interception is an insignificant mechanism. Nevertheless, for a filtration flow, overlooking the interception events could cause considerable errors in predicting the collection efficiency (Fotovati, et al., 2010; Kasper, et al., 2009). To take into account the intercepted events in commercial CFD simulations, researchers have to develop user-defined functions or

C++ subroutines (Fotovati, et al., 2010; S. A. Hosseini & Tafreshi, 2010; J. Wang & Pui, 2009). In these user-defined functions, the distance from each particle mass point to the nearest wall surface would be monitored so as to capture interception events.

In this doctoral dissertation work, a novel "virtual surface" approach to simulate particle deposition by interception in aerosol flows was developed and applied based on ordinary CFD packages. Commercial CFD program was used to simulate the flow field in a fibrous screen model as well as particle trajectories. By using standard functions of each CFD program, a "virtual surfaces" which was a radius away from the fiber surface, was generated by user to record interception events. The CFD-based results agreed well with experimental results, and also with empirical correlations for interception. For fibrous filter or screen applications, the approach developed in this study eliminates the need for user defined functions to account for interception; the results obtained using this approach can be readily validated by researchers in the field.

2.2.1 Fibrous Screen Model and the Virtual Surface

An electromesh screen model was chosen to demonstrate the "virtual surface" approach. The screen was experimentally investigated by Han et al. (T. Han, 2007; T. Han, et al., 2009) under various operating conditions. Experimental studies were carried out to identify the aerosol deposition on commercial-used electroformed wire screens. Particles with aerodynamic diameters between 3 and 20 μm were introduced in this experiment. 3D numerical simulations were performed using the CFD tools in the present study. This screen model consisted of a single layer of straight cylindrical wires,

crossing to form evenly-spaced square openings. The main parameters of the screen model are given in Table 2.1.

ANSYS FLUENT 12.1 (ANSYS Inc., Canonsburg, PA) and STAR-CCM+ 5.02 (CD-adapco, London, UK) were used as the CFD tools in this study. A volume mesh was generated using GAMBIT 2.2.30 (ANSYS, Inc., Canonsburg, PA), based on the 3-D geometric model shown in Figure 2.2. The length, width, and height of the computational domain were 1.269 mm × 1.269 mm × 2.538 mm, separately. Two crossing cylinders of 65 μm in diameter were placed in the center of the volume mesh, representing a unit section of the electroformed screen. The volume mesh included about 1.5 million tetrahedron cells, with the smallest cells near the fiber surface. The minimum cell volume was about 1.4×10^{-18} m^3, which was roughly the volume of a 1-μm cube. The same volume mesh was used with both FLUENT 12.1 and STAR-CCM+ 5.02.

Table 2.1 Parameters of the electroformed screen.

Fraction of open area, f_{OA}	Mesh size (number of openings/inch)	Screen fiber diameter d_f (micrometer)	Opening width (micrometer)
0.90	20	65	1204

The flow to be simulated was perpendicular to the cylindrical fibers, and the same as the gravity direction. The upstream surface of the computational domain was set to have a uniform velocity boundary condition, with a pressure of 1 atm. The lateral

surfaces were set to be symmetry planes, i.e. no shear across these surfaces. The downstream surface was set to have the same mass flow rate as the upstream surface. The fiber surfaces were set to be no-slip boundary. Also, the fiber surfaces were set to "trap" any particles that deposit by impaction. The face velocity (velocity at the inlet surface) was chosen to be 0.213, 0.6 and 1.06 m/s, for which experimental results were available from the work by Han et al. (T. Han, 2007; T. Han, et al., 2009).

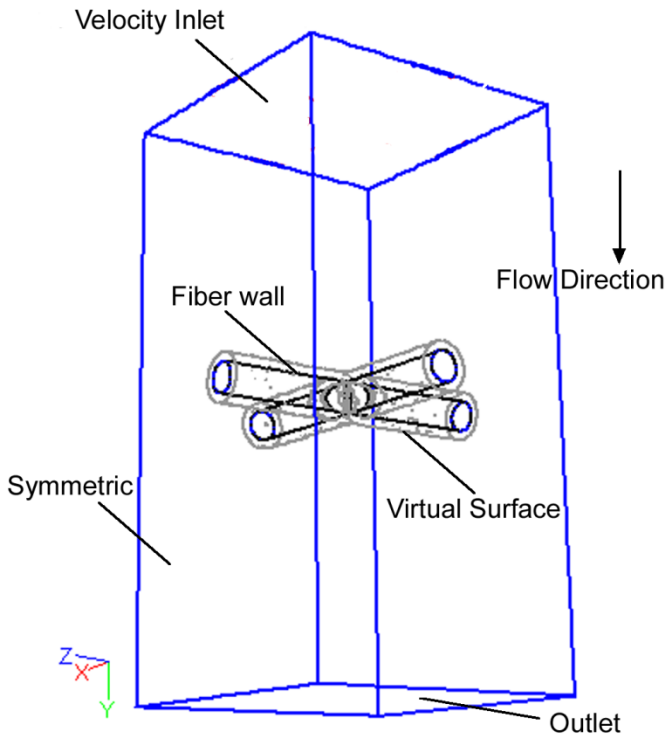

Figure 2.2 Three-dimensional electroformed screen model. Boundary conditions: Inlet surface -'Velocity Inlet' (with uniform face velocity); Lateral surfaces - 'Symmetric'; Outlet surface – 'Outflow'; Surfaces of fiber – 'Wall'.

Standard functions of the CFD programs were used to construct "virtual surfaces", as shown in Figure 2.3, around the fibers. The virtual surfaces were concentric with the cylindrical fibers. The distance between the virtual surface and the fiber surface (real surface) is equal to the radius of the particles ($d_p/2$) whose interception events were to be recorded. In FLUENT, a "virtual surface" was created by building an *Interior Boundary* with the *Surface* function; in STAR-CCM+, a virtual surface was created by building a *Cylinder Section* with the *Derived Parts* function. The "virtual surfaces" were not real, and did not alter the original geometric model or the mesh structure, hence did not affect the flow field simulation or the Lagrangian particle tracking. For each particle size, a separate set of virtual surfaces (two crossing cylinders) were created to record the interception events. The construction of the virtual surfaces could be carried out either before or after the flow field simulation was completed.

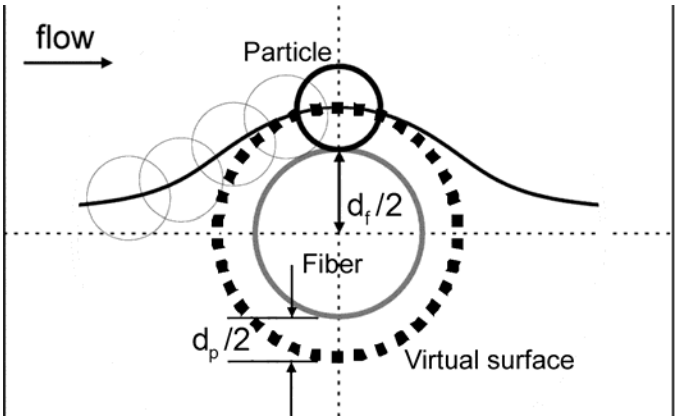

Figure 2.3 A schematic showing a virtual-surface relative to the cross section of a cylindrical fiber and its functionality for recording particle interception.

2.2.2 Flow Field Simulation and Lagrangian Particle Tracking

The laminar model and the k-ε turbulence model were used for this simulation. Both steady and unsteady cases were considered. Necessary precautions were taken to ensure that near-wall resolution was sufficiently high (Y. J. Tang, et al., 2010). A convergent flow field was obtained first within the computational domain, then particle trajectories were tracked using the Lagrangian particle tracking function with each CFD program. Each particle was tracked based on the following Newton's second law equation:

$$m_p \frac{dv_p}{dt} = \frac{1}{2} C_D \rho_a A_p \left(v_a - v_p\right)\left|v_a - v_p\right| \tag{2.7}$$

where v_p and v_a are the velocity of the particle and the air flow, respectively, m_p is the mass of the single particle, ρ_a is the air density, A_p is the projected area of the particle on the plane perpendicular to the flow direction, and C_D is the drag coefficient, which can be taken from functions (Morsi & Alexander, 1972) offered by CFD tools depending on Reynolds number. In particle tracking, turbulent dispersion of particles was included when using the k-ε model and the instantaneous fluctuating velocity components were calculated based on the characteristic lifetime of eddies (Fluent_Inc., 2005). The thermophoretic effect, Brownian motion and electrostatic forces were neglected in our particle tracking.

Due to the low particle concentration of the simulated aerosol flow, one-way coupling was assumed such that the air flow affected particle motion but not vice versa. From the inlet surface, particles were released at a sufficiently high parcel density (Y. J.

Tang, et al., 2010), which is about 10^{11} particle injection points per square meter surface area for both CFD tools. In FLUENT, the particle release density was dependent on the surface mesh density, and in STAR-CCM+, a presentation grid (a *Probe* type *Derived Part*) was built for the particle release.

Particle deposition by impaction was obtained directly through standard particle tracking of the CFD programs. In FLUENT, the number of particles that deposited on the 'real' fiber surface by impaction was obtained directly by *Particle tracks* in *Display* function; while in STAR-CCM+, the incident mass flow rate of particles onto the fiber surface (real surface) was obtained directly from *Track: particle flow rate* results in *Report* function.

Meanwhile, information of particles passing through the virtual surfaces was obtained. In FLUENT, the number of particles crossing the virtual surfaces was obtained through *Discrete Phase Sample* in *Report* function; in STAR-CCM+, the mass flow rate through the virtual surfaces was obtained from *Track: particle flow rate* results in *Report* function.

2.2.3 Calculation of Deposition Efficiency Based on CFD Results

Particle deposition on the fiber surfaces was quantitatively described in terms of collection or deposition efficiencies. Taking FLUENT simulation as an example, the deposition efficiency due to impaction was calculated using the following equation:

$$\eta_{imp} = \frac{n_{imp}}{n_{total}} \tag{2.5}$$

where n_{imp} is the number of particles that deposited on the fiber surface by inertial impaction (output as simulation result through the standard function); n_{total} is the total particle number released to the domain (controlled as user input before simulation). With STAR-CCM+, the deposition efficiency due to impaction was calculated using the following equation:

$$\eta_{imp} = \frac{m_{imp}}{m_{total}} \tag{2.6}$$

where m_{imp} is the particle mass flow rate captured on the fiber surface (output as simulation result through the standard function), m_{total} is the total particle mass flow rate released to the domain (controlled as user input before simulation).

Deposition by interception was calculated based on the particle crossing events through the virtual surfaces. In FLUENT, the number of particle crossing events through the virtual surfaces was obtained, which includes particle IDs for both impacted and intercepted particles. The number of particles 'impact' on walls, n_{imp}, which are captured by the standard Lagrangian particle tracking, is obtained by particle tracks function. The particle IDs for these 'impact' particles could be gained through discrete phase sample result based on physical fiber walls. On the other hand, the number of particles that get within virtual surfaces which would be trapped by walls due to interception but not capture by standard functions, n_{int}, could be obtained by comparing the particle IDs between 'discrete phase sample' results based on fiber wall (n_{imp}) and virtual surfaces (actually n_{imp}+ n_{int}). So in this case, the deposition efficiency by interception would be:

$$\eta_{int} = \frac{n_{int}}{n_{total}} \tag{2.7}$$

where n_{int} should be the difference of the particle numbers between sample results on virtual surface and fiber wall.

In STAR-CCM+, the particle mass flow rate through the virtual surfaces the particle mass flow rate is counted, and the deposition efficiency by interception would be defined as:

$$\eta_{int} = \frac{m_{VS} - m_{imp}}{2m_{total}} \tag{2.8}$$

where m_{vs} is the particle mass flow rate through the virtual surface, which includes particles trapped by impaction, intercepted particles which goes *in* through the virtual surface and intercepted particles which goes *out* through virtual surface since interception particles would not be captured in the standard Lagrangian particle tracking. So the actual mass flow rate of interception particles would be particle flow rate through appropriated cylinder section minus impaction rate, then divided by 2, as shown in Equation (2.8).

Thus in FLUENT, the total deposition efficiency due to inertial impaction and interception is:

$$\eta_{total} = \frac{n_{imp} + n_{int}}{n_{total}} \tag{2.9}$$

and in STAR-CCM+:

$$\eta_{total} = \frac{m_{VS}}{m_{total}} \tag{2.10}$$

2.2.4 Calculation of Deposition Efficiency Using Empirical Correlations

For this filtration system, the deposition efficiency by interception and total efficiency could be gained from previous method through CFD simulation. The results could be validated using the experiment data (T. Han, 2007; T. Han, et al., 2009) and calculations from empirical correlations (K. W. Lee & Gieseke, 1980; K. W. Lee & Liu, 1982; K. W. Lee & Ramamurthi, 1993; B. Y. H. Liu & Rubow, 1990; Pich, 1966).

These empirical correlations for the single fiber efficiency were used to calculate the deposition efficiency by interception of the electroformed screen model. The deposition efficiency by interception was related to the single fiber efficiency through the following equation:

$$\eta = 1 - \exp\left(\frac{-4\alpha\eta_{SFE}t}{\pi d_f}\right) \tag{2.11}$$

where α is the solidity, which equals to 1- f_{OA} (f_{OA}, the fraction of open area for a screen, is given in Table 2.1); η_{SFE} is the single-fiber-efficiency due to interception based on these correlations; t is the thickness of the screen, which equals to d_f here in our one-layer screen model. The empirical correlations used to calculate η_{SFE} are shown in Table 2.2.

In the empirical correlations, *Ku* is the Kuwabara hydrodynamic factor, a dimensionless factor that compensates for the effect of distortion of the flow field around a cylinder because of its proximity to other cylinders. (Hinds, 1999)

$$Ku = -\frac{\ln\alpha}{2} - \frac{3}{4} + \alpha - \frac{\alpha^2}{4} \tag{2.12}$$

Kn is the Knudsen number. It is related to the gas mean free path λ through the following equation:

$$Kn = \frac{2\lambda}{d_f} \tag{2.13}$$

Table 2.2 Single-fiber-efficiency empirical correlations used in this study to calculate deposition efficiency by interception.

Investigator(s)	Single-fiber-efficiency expressions for interception
Lee and Ramamurthi (1993)	$\eta_{SPE} = \frac{1+R}{2Ku}\left[2\ln(1+R) - 1 + \alpha + \left(\frac{1}{1+R}\right)^2\left(1-\frac{\alpha}{2}\right) - \frac{\alpha}{2}(1+R)^2\right]$
Lee and Gieseke (1980)	$\eta_{SPE} = \frac{1-\alpha}{Ku}\frac{R^2}{(1+R)^m},\ m = \frac{2}{3(1-\alpha)}$
Pich (1966)	$\eta_{SPE} = \frac{(1+R)^{-1} - (1+R) + 2(1+1.996Kn)(1+R)\ln(1+R)}{2(-0.75-0.5\ln\alpha) + 1.996Kn(-0.5-\ln\alpha)}$
Liu and Rubow (1990)	$\eta_{SPE} = 0.6\frac{1-\alpha}{Ku}\frac{R^2}{1+R}C_r,\ C_r = 1 + \frac{1.996Kn}{R}$
Lee and Liu (1982)	$\eta_{SPE} = 0.6\frac{1-\alpha}{Ku}\frac{R^2}{1+R}$

2.2.5 Quantitative Comparison of Efficiency Results

The CFD-derived deposition efficiency results were compared with experimental results from a previous study (T. Han, 2007). The agreement between the CFD-based

collection efficiency and the experimental results was quantified using a root-mean-square normalized error, e_{rms}, defined as follows:

$$e_{rms} = \sqrt{\frac{1}{n}\sum_{i=1}^{n}\frac{\left(\eta_{1,i}-\eta_{2,i}\right)^2}{\eta_{1,i}^2}} \tag{2.14}$$

where n is the number of the data pairs for comparison; $\eta_{1,i}$ is the value of the efficiency obtained by method 1 (experimental measurements or empirical calculations), for the *ith* experimental condition (combination of particle size and face velocity); and, $\eta_{2,i}$ is the efficiency obtained by method 2 (CFD simulation), for the same *i*th condition.

2.3 Turbulent Deposition - Turbophoresis

To quantitatively evaluate the turbophoresis effect and predict turbulent deposition, simple straight pipe geometry with available experimental data is studied here, and also, eliminates the interference of other deposition mechanism. The amount of deposition predicted has been seen to depend on the choices of different turbulent models and particle tracking procedure used (Y. Liu et al., 2007; Matida, et al., 2004). Wall functions and mesh resolution also could greatly influenced the prediction of turbulent conditions and aerosol deposition (Parker, et al., 2008). Therefore, a organized study of the dependence of CFD-derived deposition with different turbulence models, wall functions and mesh resolutions in vertical straight pipe flow was performed, in order to provide a better understanding of the requirements for relevant quantitative estimations.

Typically in practice, the selection of turbulence models and the control of near-wall y_+ may be both limited. Therefore, it is probably useful to investigate why certain turbulence models and certain mesh conditions produce more accurate turbulent deposition simulations. It is possible that such investigation may reveal more fundamental criterion for CFD simulation of turbulent deposition, which may be applied in practice. Herein I report such an investigation, in which the hypothesis is that the accuracy of the turbulent deposition results is strongly dependent on the accuracy of the simulated near-wall turbulence kinetic energy (TKE), or more specifically, the wall-normal mean square fluctuation velocity. The objective of this study was to determine the relation between particle deposition velocity and the wall-normal mean square fluctuation velocity as predicted by CFD simulation.

In this study, I carried out flow field simulation using a quarter geometric model of the pipe flow, and Lagrangian particle tracking with the one-way coupling assumption. In post-processing of the simulation results, I used the Eulerian description of turbulent deposition introduced above. Herein I describe the methods of CFD simulation of turbulent deposition, and the post-processing methods.

2.3.1 Methods of CFD Simulation

In this study, CFD simulation of turbulent deposition was carried out using the commercial code STAR-CCM+ 5.04 (CD-adapco, London, UK), with the effects of several CFD parameters investigated. The simulation results were compared to

experimental results of Liu and Agarwal (Benjamin Y.H Liu & Agarwal, 1974) for assessment of accuracy.

(1) Control Volume and Mesh Generation

The vertical straight pipe used in Liu & Agarwal's experiment had a length of 1.02 m and an inner diameter of 12.7 mm. Taking advantage of the axisymmetric nature of the flow, a quarter cylindrical control volume was used for the CFD simulation in this study, representing one fourth of the pipe flow. A three-dimensional geometric model was built using the STAR-CCM+ geometry function (3D-CAD models).

For mesh generation, polyhedral cells with a target size of 0.1 mm were used for the bulk of the control volume. Fifteen layers of prism cells were applied in near-wall regions and the cell thickness was increased away from the wall at a growth factor of 1.1 (more prism layers might be involved for mesh convergence study). A portion of the inlet surface mesh (perpendicular to the direction of flow) is shown in Figure 2.4.

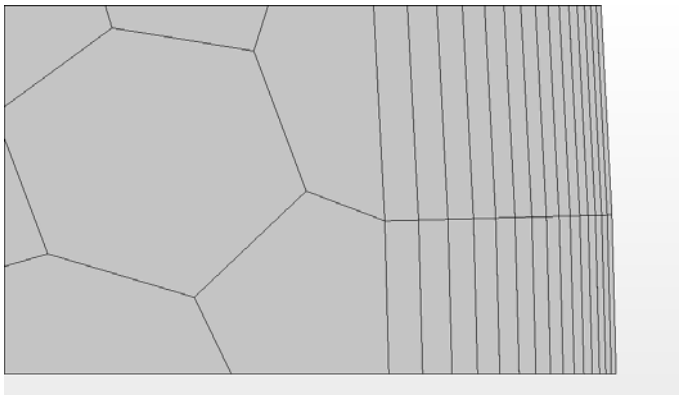

Figure 2.4 A portion of the inlet surface mesh (perpendicular to direction of flow) showing polyhedral cells (left) and 15 layers of near-wall prism cells with minimum thickness 5 μm at the wall (far right).

(2) Wall Treatment

The high-y+ wall treatment and the all-y+ wall treatment in STAR-CCM+ were applied to examine the effect of wall treatment. Wall treatment is often used in CFD simulation to model near-wall turbulent flow. Therefore the effect of wall treatment was investigated in this study by applying different wall treatment schemes in the simulation. The proper wall treatment is dependent on the y_+ value of wall-adjacent cells (often referred to simply as y_+):

$$y_+ = y\left(\frac{u_*}{\nu}\right) \tag{2.15}$$

where y is the distance from the centroid of a wall-adjacent cell to the wall; ν is the kinematic fluid viscosity and u_* is the friction velocity of turbulent flow.

In STAR-CCM+, the high-y+ wall treatment is a wall-function type approach in which it is assumed that the wall-adjacent cell lies within the logarithmic region of the boundary layer; the all-y+ wall treatment is a hybrid approach that attempts to emulate the high-y+ wall treatment for coarse meshes and the low-y+ wall treatment for fine meshes when the viscous sub-layer is properly resolved (CD-adapco, 2008). For comparison, the high-y+ formulation in STAR-CCM+ is roughly equivalent to the standard wall-function approach in ANSYS FLUENT; the all-y+ formulation is roughly equivalent to the enhanced wall treatment in ANSYS FLUENT approach where in the wall-adjacent cells.

The wall treatments have been specialized according to each turbulence model used, since assumptions respect to each model need to be made for the wall boundary conditions for the turbulence quantities.

For the all-y+ wall treatment, it is recommended to have y_+ value on the order of unity (CD-adapco, 2008). For the pipe flow in Liu and Agarwal's study, a wall distance of 5 μm would give a unity y_+ value at Reynolds number of 50000, and a y_+ of 0.25 at Reynolds number 10000. Therefore, in this study the distance from the wall to the center of the first layer of prism cells was varied from 5 μm to 50 μm (corresponding to y_+ a value of 1 to 10) to explore the effect of near-wall mesh resolution on turbulent deposition prediction.

(3) Boundary Conditions

For the surface representing the wall of the pipe, the boundary condition was set to be "wall" with no-slip condition. In accordance with the experimental installation used by Liu and Agarwal (smooth glass pipe), the pipe wall boundary condition was set to be smooth. The inlet surface of the control volume was assigned "velocity inlet" boundary condition with a uniform velocity perpendicular to the inlet surface; the magnitude of the velocity was calculated from the flow rate used by Liu and Agarwal. The outlet surface of the control volume assigned 'flow-split outlet' boundary condition. The two lateral boundaries were set to be connected "periodic plane" condition, following the axisymmetric simplification mentioned earlier in building of the pipe geometry model. For the particle phase, an "escape" boundary condition was assigned,

i.e. no reflection or bounce for particles was allowed at the surfaces of the control volume.

(4) Turbulence Modeling

Four widely used turbulence models available with STAR-CCM+ were used in this study, namely the k-ε model (RNG), the k-ω shear stress transport (SST) model, the Reynolds Stress model (RSM), and the Large Eddy Simulation model (LES). For three RANS models (k-ε, k-ω and RSM), maximum 5000 iterations were allowed for each simulation (all momentum residuals became almost constant and less than 10^{-3}). When running the LES model, the flow field solution obtained with the RSM model was used as the initial condition. The LES time step used was 1 μs, and total of 5000~10000 time steps were used. The stopping criterion was either the simulation had reached 50 iterations, or the residuals had all become lower than 10^{-4}.

(5) Particle Tracking

Particle trajectories were simulated following the turbulent flow field simulation, and assumptions had been made that the aerosol was sufficiently dilute and thus no influence acted on each other or the air flow (Y. J. Tang, et al., 2010). The Lagrangian multiphase model (generally known as Lagrangian particle tracking) in STAR-CCM+ was applied to simulate the particle trajectories, in which the momentum equation of individual particles was numerically solved. (Tang & Guo, 2011) Electrostatic forces, shear-induced lift forces, Brownian motion and thermophoresis were not included in this simulation. Particle diameter was varied from 1 to 20 μm in this study, corresponding to dimensionless relaxation time from 0.1 to 43 at Reynolds number 10000, and

dimensionless relaxation time from 2 to 740 at Reynolds number 50000. The particle density was set to be 920 kg/m^3 (olive oil), as was the case in Liu and Agarwal's experiments (1974). Particles were released from an injection surface on the inlet boundary of the pipe at an initial velocity equal to the mean flow velocity; there were approximately 1,000 uniformly distributed injection points on the surface injector.

With the Reynolds-averaged Navier–Stokes (RANS) models (k-ε, k-ω and RSM), the effect of turbulence on particle trajectory was simulated with the "turbulent dispersion" model. From each particle injection point, 100 turbulence-affected particle trajectories (called "parcels" in the CFD package) were simulated, using information of the simulated turbulent flow field in conjunction with a random number generator. (Tang & Guo, 2011) Thus, for each simulation a total of approximately 10^5 parcels were tracked.

With LES, the turbulence effect on particle trajectory was not simulated with the "turbulent dispersion" model, because evidently the turbulence parameters needed for that model were no longer available. Instead, the effect of turbulence on particle trajectory was simulated through the use of flow field solutions at multiple consecutive time points. For each particle injection point, a particle trajectory was simulated using the flow field solution at a particular instant (by using the "solver frozen" option in STAR-CCM+); then from the same particle injection point, another particle trajectory was simulated using flow field solution at the next instant in LES simulation. This was repeated 100 times, so that for each injection time point, 100 particle trajectories were simulated; the variation of the particle trajectory originated from the same injection point

would reflect a pseudo turbulence effect. The LES time step (1 μs) was chosen such that it was much smaller than the Lagrangian time scale of the turbulent flow (approx. 100 μs at Re=50,000) and the relaxation time of the smallest particle (approx. 5 μs), in order for this scheme to be valid.

Calculations of the aerosol penetration and the particle deposition velocity are described in the following section.

2.3.2 Methods of Post-Processing

(1) Calculation of Penetration and Dimensionless Deposition Velocity

Similar to the experimental approach used by Liu and Agarwal (Benjamin Y.H Liu & Agarwal, 1974), particle deposition was quantified excluding locations near the entrance and the exit of the pipe flow. For that purpose, two plane sections as "derived parts" were created in the CFD control volume, to be used for particle counting and for calculating the penetration for the pipe section in between. These two plane sections were perpendicular to the direction of the flow, at a distance of 127.5 mm and 637.5 mm from the inlet surface, respectively.

The aerosol penetration, defined as the ratio of aerosol concentration at the exit of a pipe flow to that at the entrance, was calculated:

$$P = \frac{n_{637.5}}{n_{127.5}} \tag{2.16}$$

where $n_{637.5}$ and $n_{127.5}$ were the numbers of particles moving through the derived surface sections which are perpendicular to the direction of the flow, and at a distance of 637.5 mm and 127.5 mm from the inlet surface, respectively.

With the penetration known, the deposition velocity can be calculated with the following equation (Sehmel, 1970):

$$V_{dep} = \frac{Q}{\pi D_i L} \ln\left(1/P\right) \tag{2.17}$$

where Q is the volumetric flow rate through the pipe, D_i is the inner diameter of pipe, L is the length of the pipe and P is the aerosol penetration efficiency through the pipe section. Then the dimensionless particle deposition velocity can be calculated using Equation (1.13), where u_* is the friction velocity defined as:

$$u_* = \left(\frac{f}{2}\right)^{0.5} U \tag{2.18}$$

where U is the average fluid velocity and f is the Fanning friction factor for the pipe flow. For the smooth pipe used by Liu and Agarwal (Benjamin Y.H Liu & Agarwal, 1974), the friction factor is calculated from the Blasius formula given by Schlichting (Schilichting, 1968), valid for Re < 100000:

$$f = \frac{0.316}{4\left(\mathrm{Re}\right)^{0.25}} \tag{2.19}$$

where Re is the pipe flow Reynolds number based on the pipe inner diameter.

The accuracy of the CFD simulations was quantified against the experimentally derived results, both in terms of penetration and dimensionless deposition velocity. For

each flow condition, the discrepancy of dimensionless deposition velocity between the CFD simulation and the experimental results, known as the Geometric Standard Deviation (GSD), was quantified as:

$$GSD = \mathbf{exp}\left[\left(\frac{\sum n_i \left(\mathbf{ln} V_{sim}^{+} - \mathbf{ln} V_{\boldsymbol{exp}}^{+}\right)^2}{N-1}\right)^{0.5}\right] \tag{2.20}$$

where N represents the number of the comparison pairs. When a CFD-simulated condition was not available from the experiments, interpolation was carried out to generate an "experimental" data point $V_{\boldsymbol{exp}}^{+}$ to be compared with the CFD result V_{sim}^{+}.

(2) Determination of the Particle Responsiveness Factor

According to Equation (4), $\frac{d}{dy}\left(\overline{V_{py}'^2}\right)$ is a critical quantity for turbophoresis. The mean square velocity fluctuation of the particles, $\overline{V_{py}'^2}$, is not directly known from the CFD simulation, but the mean square velocity fluctuation of the fluid, $\overline{V_{fy}'^2}$ is readily available from CFD simulation. Therefore, in this study $\frac{d}{dy}\left(\overline{V_{py}'^2}\right)$ was quantified based on $\frac{d}{dy}\left(\overline{V_{fy}'^2}\right)$ from CFD simulation, using Guha's formulation. In fact, the ratio of two gradients of mean square velocity fluctuation was calculated and compared against an empirical relationship, as a means of evaluating the validity of the CFD simulation of turbulent deposition.

The particle responsiveness factor, α, is defined as the ratio of the wall-normal gradient of the mean square particle velocity fluctuation to the wall-normal gradient of the mean square fluid velocity fluctuation:

$$\alpha = \frac{\dfrac{d}{dy}\left(\overline{V'^2_{py}}\right)_w}{\dfrac{d}{dy}\left(\overline{V'^2_{fy}}\right)_w} \tag{2.21}$$

In order to obtain the value of α from the CFD simulation results, substituting Equation (2.21) into Equation (1.12), and replacing the derivative with an expression based on finite difference, it yields the following equation, expressed in terms of the quantities at the wall and at the wall-adjacent cell centroid:

$$\overline{V^c_{py,w}}\frac{\left(\overline{V^c_{py,1}} - \overline{V^c_{py,w}}\right)}{y_1} + \frac{\overline{V^c_{py,w}}}{\tau} \approx -\alpha\frac{d}{dy}\left(\overline{V'^2_{fy}}\right)_w \tag{2.22}$$

where $\overline{V^c_{py,w}}$ is the particle convective velocity in wall-normal direction at the wall, i.e., the particle deposition velocity that may be experimentally measured; $\overline{V^c_{py,1}}$ is the particle convective velocity in the wall-normal direction at the wall-adjacent cell centroid in CFD simulation, which could be obtained from the particle convective flux through a user-defined 'virtual wall surface' through the wall-adjacent cell centroids. y_1 is the distance from the wall-adjacent cell centroid to the pipe wall.

The gradient term on the right hand side of Equation (2.22) was obtained from the flow field simulation, to be described below; the two particle convective velocity quantities on the left hand side were obtained from Lagrangian particle tracking results

and Equation (2.17). Note that in Equation (2.22), the particle relaxation time τ replaces the particle inertial relaxation time τ_I. This approximation shall not introduce significant error for the particle size range involved in this study, because the "slip" velocity between the particle the gas flow should be small.

To provide references for the CFD-based results to be compared against, empirical equations were also used to calculate the particle responsiveness factor. Using the finite difference method, the ratio of $\frac{d}{dy}\left(\overline{V'^2_{py}}\right)_w$ to $\frac{d}{dy}\left(\overline{V'^2_{fy}}\right)_w$ would be approximately equal to the ratio of $\overline{V'^2_{py}}$ to $\overline{V'^2_{fy}}$ at the wall-adjacent cell centroid, with the assumption that velocity fluctuation would be zero at y = 0. Thus, the particle responsiveness factor at the wall-adjacent cell centroid may be calculated with following empirical equation (Binder & Hanratty, 1991):

$$\frac{\overline{V'^2_{py,1}}}{\overline{V'^2_{fy,1}}} = \frac{1}{1+0.7\left(\tau / \tau_{L,1}\right)} \tag{2.23}$$

where $\tau_{L,1}$ is the Lagrangian time scale of fluid turbulence at the wall-adjacent cell centroid, which is calculated as (Johansen, 1991):

$$\tau_{L,1} = \frac{\nu_{t,1}}{\overline{V'^2_{fy,1}}} \tag{2.24}$$

Where $\nu_{t,1}$ is the fluid turbulent viscosity at the wall-adjacent cell centroid, which is calculated as follows (Davies, 1966):

$$\nu_{t,1} = y_+^{\left(4-y_+^{0.08}\right)} \left[\frac{2.5\times10^7}{\mathbf{Re}}\right]^{\left(-y_+/\left(400+y_+\right)\right)} \times 10^{-3}\nu \tag{2.25}$$

where the y+ is evaluated at the wall-adjacent cell centroid; v is the kinematic viscosity of the fluid.

(3) Determination of $\frac{d}{dy}\left(\overline{V_{fy}'^2}\right)_w$

To obtain the wall-normal gradient of the wall-normal mean square fluid velocity fluctuation, $\frac{d}{dy}\left(\overline{V_{fy}'^2}\right)_w$, within the STAR-CCM+ framework, a "line derived part" was created, so that the line was in the radial direction as well as parallel to the y axis, and $\overline{V_{fy}'^2}$ on this line was sampled to obtain $\frac{d}{dy}\left(\overline{V_{fy}'^2}\right)_w$ by finite difference. For simplicity of expression, I define:

$$K = \overline{\left(V_{fy}'\right)^2} \tag{2.26}$$

With the RANS models, the value of $\overline{V_{fy}'^2}$ was obtained directly from the flow field simulation; with the LES model, the value of $\overline{V_{fy}'^2}$ was obtained by taking the mean square of instantaneous velocity of 5000~10000 consecutive time steps. Then, $\frac{d}{dy}\left(\overline{V_{fy}'^2}\right)_w$ was obtained using the following equation:

$$\frac{d}{dy}\left(\overline{V_{fy}'^2}\right)_w = \left(\frac{\partial K}{\partial y}\right)_w \approx \frac{K_1}{y_1} \tag{2.27}$$

and a dimensionless form of the quantity was obtained by:

$$\left(\frac{\partial K}{\partial y}\right)^{+}_{w} = \frac{K_1 / u_*^2}{y_1\left(\frac{u_*}{\nu}\right)} \tag{2.28}$$

where K_1 is the value of $\overline{V'^2_{fy}}$ at the wall-adjacent cell centroid, u_* is the friction velocity of turbulent flow, and y_1 is the distance from the wall-adjacent cell centroid to the pipe wall.

(4) Determination of the Turbophoresis Factor

Equation (2.22) suggests that the particle deposition velocity is a function of the gradient of wall-normal *fluid* velocity fluctuation. Quantification of this relationship through experiments is typically not possible because the gradient of the velocity fluctuation measurement is lacking. However, it is possible to obtain this relationship from CFD simulation results. Herein I define a "turbophoresis factor", as the ratio of the dimensionless deposition velocity to the dimensionless gradient of the mean square wall-normal fluid velocity fluctuation:

$$r_t = \frac{V_+}{\left(\frac{\partial K}{\partial y}\right)^{+}_{w}} \tag{2.29}$$

In this study, the turbophoresis factor was computed once the dimensionless deposition velocity and the gradient of mean square wall-normal fluid velocity fluctuation were obtained as described above. As will be discussed later, the turbophoresis parameter may be of potential value for assessing the importance of turbulent deposition in complex flows.

3. RESULTS *

Obtained results for this doctoral dissertation study were described in this section. Different mechanisms of aerosol deposition were also discussed based on these works, including BSI penetration prediction (inertial impaction, gravitational effect and Saffman lift force), screen models in filtration system (particle interception), and turbulent deposition in vertical straight pipe flow (turbophoresis).

3.1 Aerosol Deposition and Efficiency of BSI-e

3.1.1 Simulated Flow Field

The flow field simulation results were qualitatively similar for the three different free stream velocities, so only the results for the wind speed of 8 km/h (2.22 m/s) are presented (Figure 3.1). Figure 3.1(a) shows the air velocity in a vertical plane that cuts through the BSI-e axis and is parallel to the free stream; Figures 3.1(b) and 3.1(c) show the velocity in two horizontal planes, the vertical locations of which are indicated in Figure 3.1(a). All velocity vectors shown are their projections in the respective planes. With reference to Figure 3.1(a), the aerosol flow enters the upwind side of the intake gap

*Reprinted with permission from "A Computational Fluid Dynamics Study of Particle Penetration through an Omni-Directional Aerosol Inlet" by Tang, Y.J., Guo, B., & McFarland, A.R. 2010. *Aerosol Science and Technology*, 44, 1049-1057, Copyright [2012] by TAYLOR & FRANCIS INFORMA UK LTD – JOURNALS.

and is accelerated in the curved converging flow channel between the two shells, where it reaches a maximum speed of approximately 2.6 m/s, as compared with the free stream speed of 2.22 m/s. The flow first decelerates before entering the inlet, then accelerates in the curved converging gap between the shells. Recirculation zones can be observed near the entrance of the exhaust tube. The three views of Figure 3.1 show there is a split in the aerosol flow in the gap between the shells where the center portion on the upwind side follows up the slope of the bell-shaped shells and, the off-center portions flow around the waist of the bell-shaped shell and leave the gap between the shells on the downwind side. Most of the flow goes around the inner shell and is discharged at the downwind side, while part of the flow enters the openings (windows) between the roof of the outer shell and the entrance of the exhaust tube. Part of the flow exits through the downwind vertical openings and 100 L/min leaves through the exhaust tube.

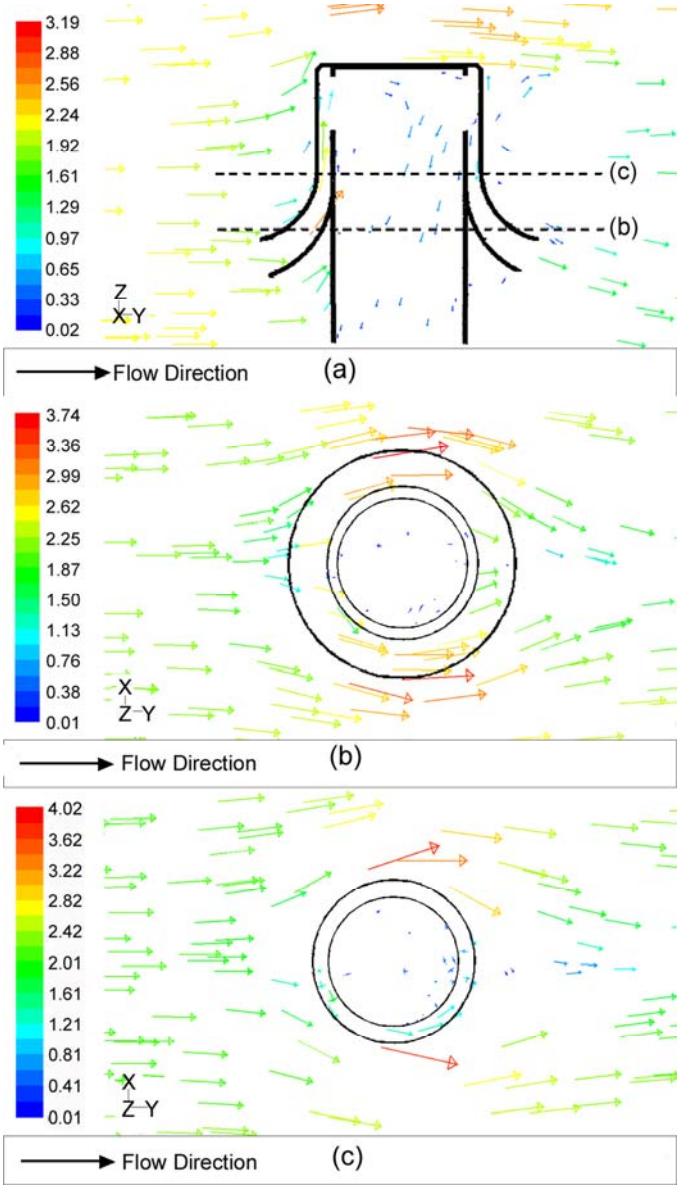

Figure 3.1 CFD simulation of the flow field at a wind speed of 8 km/h (2.2 m/s). (a) Velocity vectors in the vertical plane through the BSI-e axis and parallel to the free stream (dashed lines "b" and "c" indicate locations of the two horizontal planes for (b) and (c). (b) Velocity vectors in a horizontal plane slightly above the rim of the outer shell. (c) Velocity vectors in a horizontal plane in the cylindrical section of the shells (shell radii do not change with height). Units of velocity scales are m/s. (Tang et al. 2010).

3.1.2 CFD-Based Penetration and Regional Deposition

Aerosol penetration as a function of particle size and for wind speeds of 2, 8, and 24 km/h is shown in Figure 3.2. The CFD-based penetration results not only have the proper trends, but they are also in excellent quantitative agreement with the experimental results. The root-mean-square normalized error, e_{rms} calculated using Equation (2.3) with all available experimental data, was 3.8%.

The CFD-based penetration decreases with increasing particle size, and for the high inertia particles (e.g., 20 μm AD), the penetration also decreases with increasing wind speed. These results agree with the expectation of penetration based on aerosol mechanics for situations where inertial impaction, as illustrated by deposition in the accelerating curvilinear flow region near the entrance to the BSI-e, would control the losses.

The three penetration terms, aspiration efficiency, P_1, penetration through the between-shell passage region, P_2, and penetration through the exhaust tube, P_3 (defined in Equations 2.4 – 2.6), were calculated for 10 and 15 μm AD particles and for wind speeds of 2, 8, and 24 km/h; and, the results are shown in Table 3.1. The aspiration, P_1, is approximately equal to or slightly greater than 1, where values greater than unity are apparently associated with subisokinetic sampling conditions (Hinds, 1999). From Figures 3.1(a) and 3.1(b) it may be observed that the flow decelerates (indicated by a shift in color of velocity vectors) just upstream of the BSI-e. Also, in Figure 3.1(b), it may be noted that there is a divergence in flow away from the mean wind direction for the vectors just outside of the BSI-e on the upwind side, i.e., curvilinear flow in the x-y

plane. This external flow deceleration effect tends to enrich the concentration of aerosol in the approximate intake region subtended by the 60° angle and the height between the shell rims.

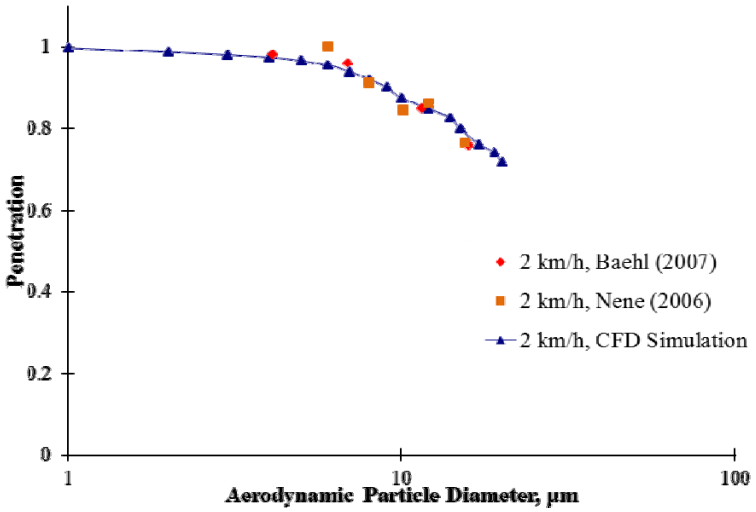

(a)

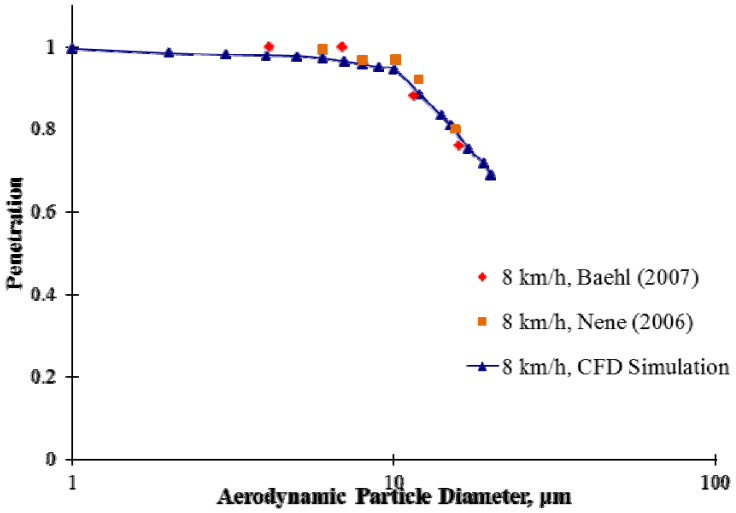

(b)

Figure 3.2 Comparison of penetration from experiments and CFD simulations at wind speeds of: (a) 2 km/h. (b) 8 km/h. (c) 24 km/h.

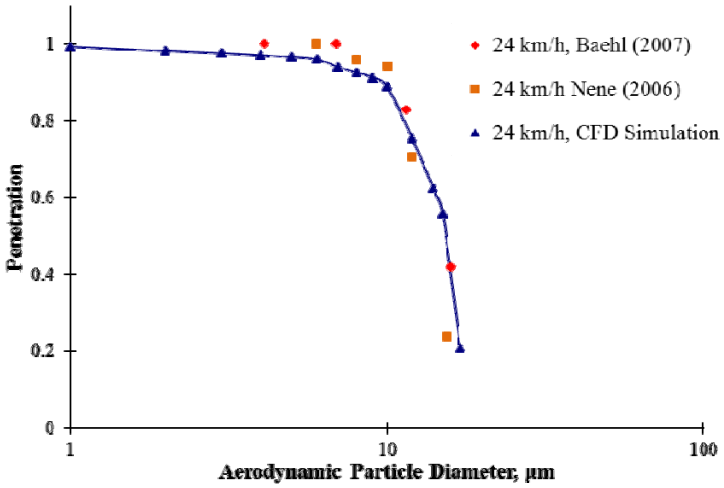

Figure 3.2 continued. (c)

Table 3.1 Estimated regional and overall penetration percentage of the BSI-e from CFD analyses. (Tang et al. 2010)

Region	Free Stream Wind Speed					
	2 km/h		8 km/h		24 km/h	
	Aerodynamic Particle Diameter					
	10 µm	15 µm	10 µm	15 µm	10 µm	15 µm
P_1	101%	102%	104%	105%	110%	112%
P_2	88.0%	81.5%	94.1%	81.5%	85.7%	55.3%
P_3	98.5%	96.4%	96.5%	94.7%	94.4%	90.1%
P_{total}	87.5%	80.1%	94.4%	81.0%	89.0%	55.8%

The penetration P_3 is near unity, suggesting that the particle losses in the exhaust tube are quite small. This is likely due to the low velocity in exhaust tube (less than 0.4 m/s in most cases) and there being no gravitational settling effect on particle deposition. P_2 had the lowest value among the three penetrations; it had approximately the same value as the overall penetration of BSI-e.

No particle deposition was found on the internal surface of the outer shell. However, significant particle deposition occurred on the curved surface of the inner shell. Deposition locations of various particle sizes on the inner shell are shown in Figure 3.3, for wind speeds of 24 km/h. The figure is the top view of the inner shell, showing deposition locations of particles of 10, 15, 20 μm AD. Each dot in the views represents a deposited particle. Each view shows approximately 200 to 1000 deposited particles, from tracking a total of 400,000 particles that enter the upstream surface of the computational domain. The visualization results clearly show that most particle deposition was concentrated on an upwind area of the inner shell that lies within the angle of about 60°, and involves the sloped portion of the inner shell. Larger particle sizes and higher wind speeds cause the particles to deposit closer to the rim of the shell. The higher inertia could cause the particle turn less when the aerosol flow entering the intake of inlet and make a turn, which means these particles with higher inertial (larger diameter and higher speed) would be more likely to deposit on the relatively lower region on the upwind area of the inner plenum just due to the inertial impaction mechanism. Scattered particle deposition locations on the lateral side might be due to a turbulent effect at those localities where turbulence intensity values of over 65% were

noted. Based on this deposition feature, some modification of the BSI design could be considered, in order to reduce this part of the inertial impaction and particle depositions in the front surface region.

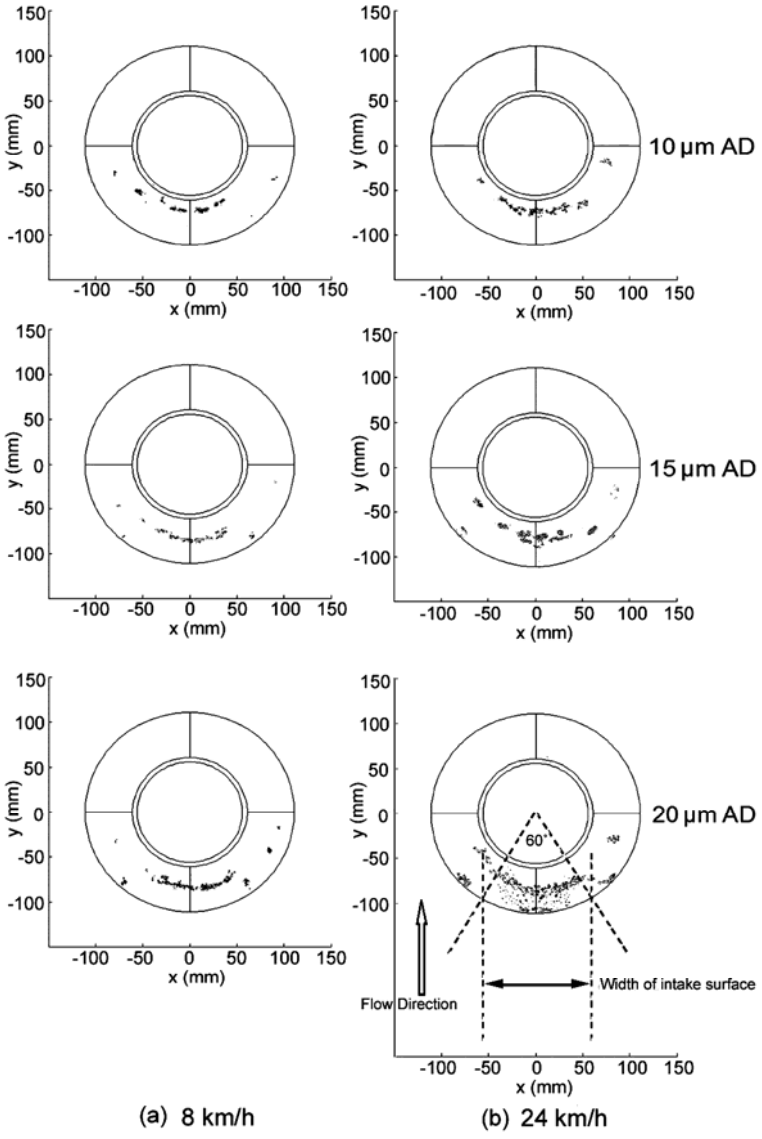

Figure 3.3 Visualization of particle deposition locations on the surface of BSI inner shell (top view) for particle diameter of 10, 15 and 20 micrometers at free wind speed of 8 and 24 km/h. (Tang et al. 2010).

3.1.3 Effect of Gravitational Settling on Penetration

CFD simulation was also used to determine the importance of gravitational settling in particle deposition. The approach used was to first conduct the particle tracking without including the gravitational force, and then repeat the calculations with gravity included. As shown in Table 3.2, at the higher wind speeds (8 and 24 km/h), the CFD-based penetration was essentially the same for all particle sizes whether gravity was considered or not. However, at the wind speed of 2 km/h, the gravitational effect was significant with the largest difference being about 8% in the case of 20 μm AD particles. At low wind speeds, the gravitational effect is more significant because of the longer residence time of the particles in the sloped part of the between-shell passage, due to the lower flow velocity in that region. This may also explain why the penetration of intermediate particle sizes at the wind speed of 2 km/h can be lower than that at 8 km/h (Figure 3.1), e.g. in Table 3.2, the penetration of 10 μm AD particles is 87.5% at 2 km/h, and 94.4% at 8 km/h.

Table 3.2 CFD-based overall penetration efficiency of the BSI-e with and without the gravitational effect.

Particle Diameter µm	**Free stream wind speed** 2 km/h			**Free stream wind speed** 8 km/h			**Free stream wind speed** 24 km/h		
	With gravitational effect	Without gravitational effect	Difference	With gravitational effect	Without gravitational effect	Difference	With gravitational effect	Without gravitational effect	Difference
1	99.6%	99.8%	0.2%	99.5%	99.6%	0.1%	99.4%	99.5%	0.1%
2	98.8%	99.4%	0.6%	98.5%	98.7%	0.2%	98.3%	98.4%	0.1%
3	98.1%	99.1%	1.0%	98.1%	98.3%	0.2%	97.7%	97.8%	0.1%
4	97.5%	98.9%	1.4%	97.9%	98.1%	0.2%	97.2%	97.4%	0.2%
5	96.7%	98.9%	2.1%	97.4%	97.7%	0.3%	96.6%	96.8%	0.2%
6	95.5%	98.3%	2.8%	97.2%	97.5%	0.3%	96.0%	96.2%	0.2%
7	93.9%	97.6%	3.7%	96.5%	96.8%	0.3%	94.1%	94.3%	0.2%
8	92.0%	96.8%	4.8%	95.8%	96.0%	0.2%	92.7%	92.9%	0.2%
9	90.1%	95.9%	5.8%	95.1%	95.4%	0.3%	91.4%	91.5%	0.1%
10	87.5%	94.4%	6.9%	94.4%	94.6%	0.2%	89.0%	89.1%	0.1%
12	85.0%	92.1%	7.1%	88.5%	88.8%	0.3%	75.5%	75.7%	0.2%
14	82.6%	89.8%	7.2%	83.4%	83.9%	0.5%	62.4%	62.6%	0.2%
15	80.1%	87.5%	7.4%	81.0%	81.7%	0.7%	55.8%	56.1%	0.3%
17	76.2%	83.9%	7.7%	75.3%	75.9%	0.6%	20.8%	21.1%	0.3%
19	74.1%	82.1%	8.0%	71.9%	72.6%	0.7%	N/A	N/A	N/A
20	71.9%	80.4%	8.5%	69.0%	69.9%	0.9%	N/A	N/A	N/A

3.1.4 Effect of Saffman Lift Force on Penetration

In most previous studies, the effects of inertial and gravitational forces had been considered; in present research, considerable effect of the Saffman lift force (Saffman, 1965), which causes motion transverse to the free stream velocity direction (Fan et al., 1992), has been numerical invested in the numerical simulation model, in order to replicate and illustrate the experimental methodology in numerical simulation. The

results showed the effect of the Saffman force would increase as the flow velocity or particle size increases; also it could decrease the penetration efficiency by 0.5%~3.4% in CFD simulation. And in comparison, Table 3.3 shows the difference of the prediction on the penetration efficiency of BSI with or without introducing the Saffman force in simulation. It suggested that the Saffman force would not be as crucial as the inertial impaction and the gravitational settling in aerosol deposition mechanism.

Table 3.3 The difference of the prediction with or without the Saffman force.

Particle Diameter μm	**Free wind speed** 2 km/h		**Free wind speed** 8 km/h		**Free wind speed** 24 km/h	
	With Saffman force	Without Saffman force	With Saffman force	Without Saffman force	With Saffman force	Without Saffman force
2	98.8%	99.3%	98.5%	99.1%	98.3%	99.0%
5	96.7%	97.6%	97.4%	98.2%	96.7%	98.1%
10	87.5%	88.8%	94.4%	95.3%	89.0%	91.0%
15	80.1%	81.5%	81.0%	82.9%	55.8%	59.2%
20	71.9%	73.3%	69.0%	71.1%	N/A	N/A

3.1.5 Relative Importance of Turbulent Dispersion

The performance of the aerosol sampling device BSI-e was evaluated using RSM model *without* the turbulent dispersion, and compared with the results from Tang et al.(Y. Tang *et al.*, 2010) which included dispersion. The device efficiency results comparison showed that in most of cases, the deviation with or without dispersion included was less than 5% of the total penetration efficiency (Figure 3.4). In this case, it is apparently that the turbulent dispersion would not be a significant influence on aerosol

deposition, if other dominant mechanism exists, such as the inertia impaction. This usually would happen when there are curved and complex flow passage, high flow rate or/and large particle size. And in such cases, the CFD-based simulation from commercial CFD codes on aerosol deposition appear be reliable.

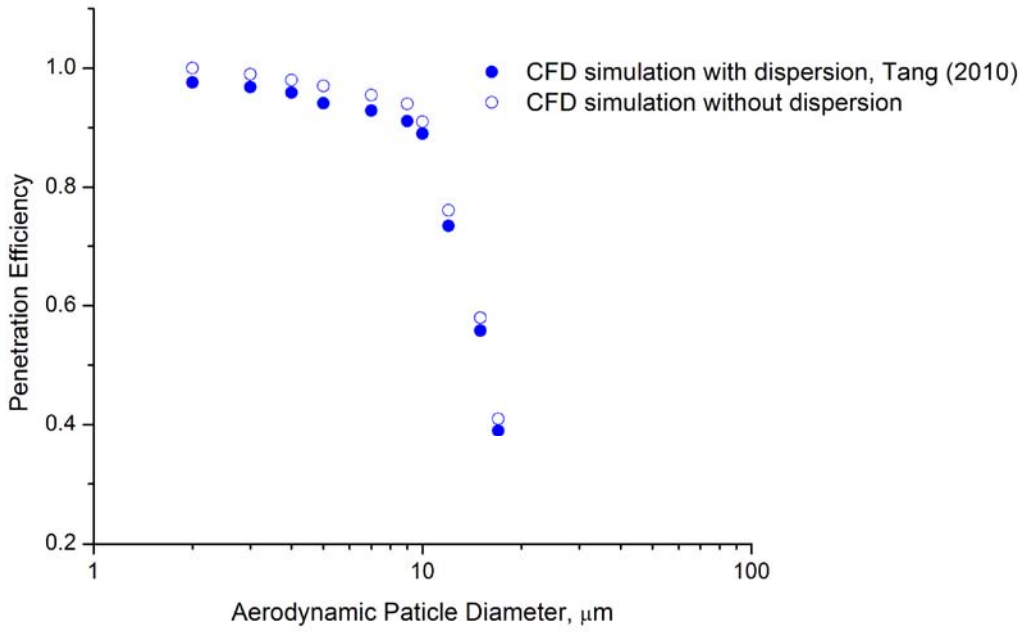

Figure 3.4 CFD simulation results with or without turbulent dispersion effect at the free wind speed of 24 km/h (Tang & Guo, 2011).

In vertical pipe flows, turbulent dispersion is the dominant mechanism for particle deposition, but there are empirical relations. Some empirical relations for calculating the rate of deposition of aerosol particles on the surface of vertical tubes were presented (Friedlander & Johnstone, 1957; Benjamin Y.H Liu & Agarwal, 1974; Mednikov, 1980) and also used for validation of CFD simulations (R. Gao & Li, 2011; Jiang *et al.*, 2010; Nerisson *et al.*, 2011; Parker, et al., 2008; F. P. Zhang & Li, 2008).

The turbulent effect on particle deposition would be quantitatively discussed within Section 3.3.

3.1.6 Dimensionless Numbers and Empirical Correlation of Penetration

Assuming that impaction and gravitational settling are the most important factors affecting aerosol penetration through the BSI-e, a semi-empirical correlation equation similar to that utilized in filtration theory (Hinds, 1999) can be constructed to relate overall penetration to a Stokes number, S_{tk}, a dimensionless gravitational settling parameter, G, and a velocity ratio, r_v, which represents the relationship of the external and the internal flow fields, and provides a correction to the first two dimensionless numbers. Assume the form of the correlation to be:

$$P = \left[1 - \frac{1}{1 + \frac{C_1 \cdot r_v^{C_2}}{Stk^{C_3}}}\right] \cdot \left[1 - \frac{1}{1 + \frac{C_4 \cdot r_v^{C_5}}{G^{C_6}}}\right] \tag{3.1}$$

where C_1 through C_6 are parameters that are determined from curve fitting. Terms in the first set of brackets on the rights size of Equation (3.1) represent the penetration if only inertial impaction is considered, and those in the second pair of brackets represent the penetration if only gravitational settling is in effect. The form of Equation (3.1) was chosen so that it would be asymptotically correct in the sense that the penetration would tend to zero when S_{tk} or G approaches infinity and it would tend to unity for very small particles for which S_{tk} and G approach zero.

The Stokes number, S_{tk}, is defined as:

$$Stk = \frac{\rho_p d_p^2 U_0 C_c}{18 \mu d_c} \tag{3.2}$$

where ρ_p is the particle density; d_p is the aerodynamic diameter of particle; U_0 is the free stream velocity (wind speed); C_c is Cunningham slip correction factor; μ is the viscosity of air; and, d_c is the characteristic dimension, which is chosen as the width of the intake gap at the flow entrance to the BSI-e (see Figure 2.1). The gravitational settling parameter, *G*, is defined as (Hinds, 1999):

$$G = \frac{\rho_p d_p^2 C_c g}{18 \eta U_0} \tag{3.3}$$

The velocity ratio, r_v, is defined as:

$$r_v = \frac{U^*}{U_0} \tag{3.4}$$

where *U** is the aerosol sampling flow rate divided by the annular area between the outer and inner shells in the region where the two shells are cylindrical ($A_{annular}$):

$$U^* = \frac{Q_{exhaust}}{A_{annular}} \tag{3.5}$$

The impaction and gravitation settling effects are functions of the between-shell air velocity, which depends on the free stream velocity, and the aerosol sample flow rate. Since *Stk* and *G* use the free stream velocity, it is necessary to modify the results through the use of the velocity ratio. Nene (Nene, 2006), in his experimental study of the BSI-e, proposed an empirical correlation that included a Stokes number and a velocity ratio but it did not include the gravitational settling factor. In the study of a cap-and-funnel type omni-directional aerosol inlet, Lee et al. (S. R. Lee, et al., 2008) had proposed an empirical equation that only included a Stokes number. The semi-empirical equation

generated in this study, which includes the three dimensionless numbers, takes into account both inertial deposition and gravitational settling. Including the velocity ratio is essentially equivalent to including a Reynolds number (based on the free stream velocity) in the correlation.

Using the experimental and CFD-based data, curve fitting with the OriginPro 7.5 software provided the correlation coefficients for Equation (3.1), which are shown in Table 3.4. With reference to Figure 3.5, the fitted curves for the three wind speeds are in excellent agreement with the experimental and CFD penetration data, especially for the lower Stokes number cases.

Table 3.4 Curve fitting results for the coefficients in Equation (3.1) with corresponding uncertainties (Tang et al. 2010).

Coefficien	C_1	C_2	C_3	C_4	C_5	C_6
Curve fitting values	0.0076 ± 0.0003	-0.105 ± 0.004	2.91 ± 0.08	0.072 ± 0.003	0.507 ± 0.009	0.955 ± 0.022

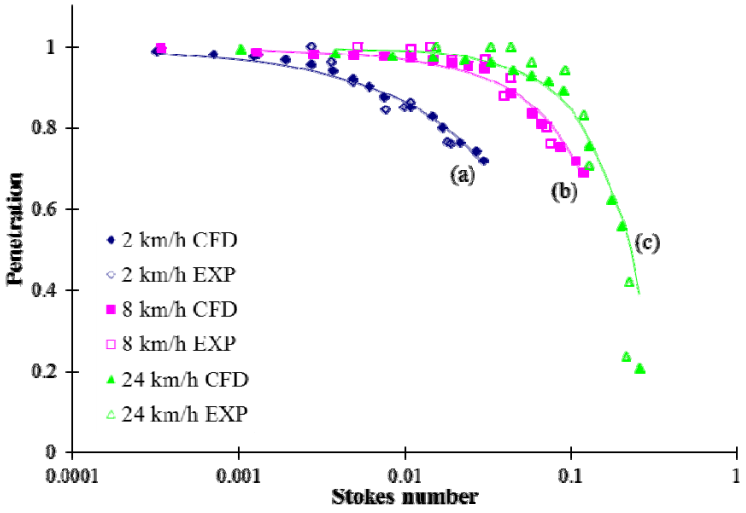

Figure 3.5 Penetration predicted from correlation compared with experimental and CFD data at wind speeds of (a) 2 km/h, (b) 8 km/h, (c) 24 km/h.

Figure 3.6 shows the agreement of the penetration predicted from Equation (3.1) with the experimental and CFD penetration values. Note that there are two data points, which are associated with the smallest abscissa values on the 24 km/h curve, that have large errors. The slope of the penetration curves through these two data points, Figure 3.2(c), is steep so a small uncertainty in the abscissa value, e.g., experimentally measured particle size or correlation fit to the numerical data, results in a large relative deviation between the experimentally measured or numerically calculated penetration and the prediction from the correlation. The root-mean-square relative error of the fitting is 3.8% with the two outlying data points removed; however, it is 13.5% when all data points are included. Omission of the two data points, which are associated with particle sizes ≥ 15 μm AD, is not a critical concern for most applications where a pre-separator with a cutpoint ~ 10 μm AD would be included in the overall inlet system; and, as the

penetration for those points is 20 – 40%, such particles would mostly be eliminated by the pre-separator.

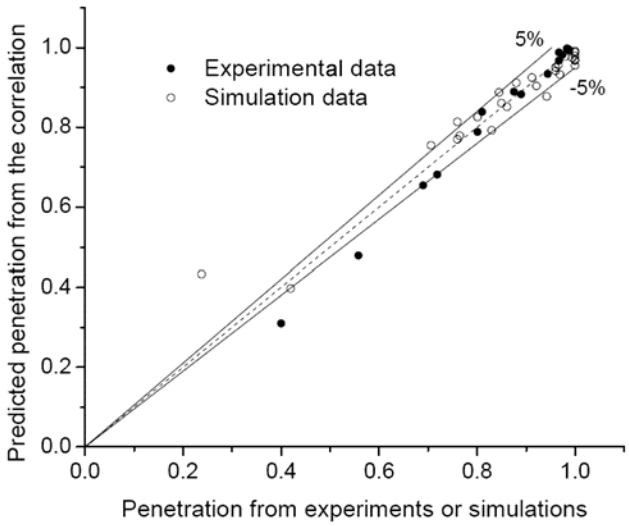

Figure 3.6 Agreement of correlation equation predictions with experimental and CFD results. (Tang et al. 2010)

3.2 CFD Predicting of Filter Interception Results

3.2.1 Flow Field and Particle Tracks

The CFD-based flow field and particle tracks results using the k-ε model are shown in Figure 3.7, for both FLUENT and STAR-CCM+, at the face velocity of 1.06 m/s. The flow field shown is that of the cross-sectional plane, while the particle tracks are originated from the entire inlet surface. In order to quantify the agreement between these simulations with the two CFD programs, flow velocities were compared at 10 points evenly spaced along the central line of the domain, 5 upstream of the fibers and 5

downstream. The average deviation of the velocity magnitude at these 10 points was about 4.8%; the maximum deviation in velocity magnitude was 7.1%.

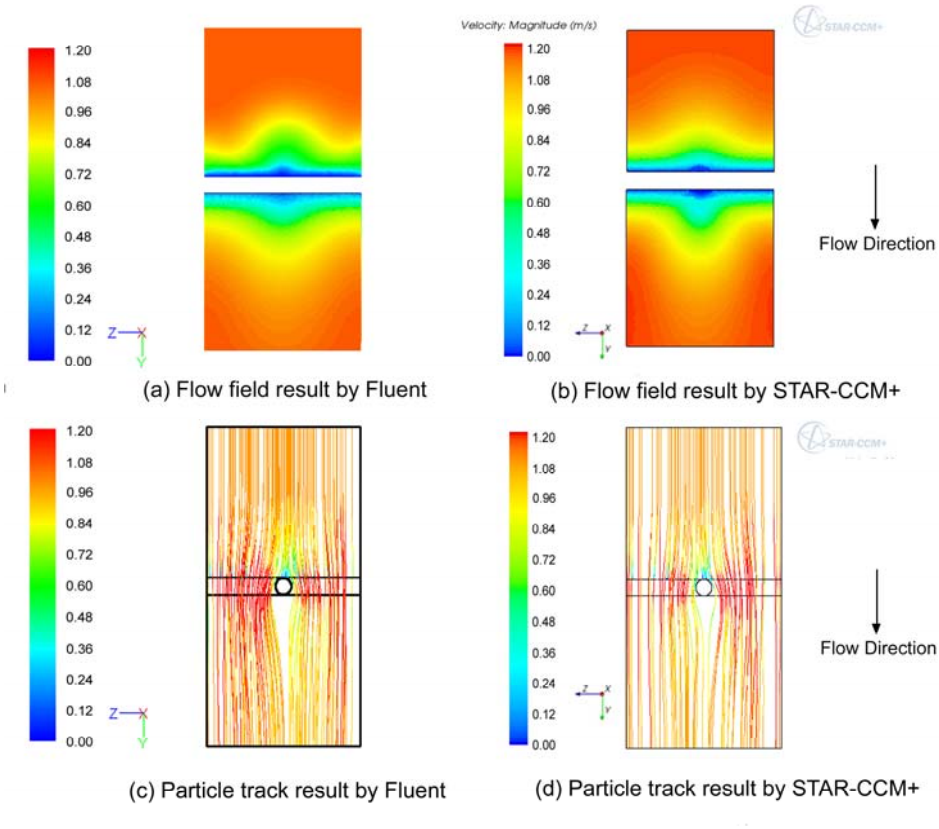

Figure 3.7 The k-ε model flow field simulation results with (a) FLUENT and (b) STAR-CCM+, and the particle tracks results with (c) FLUENT and (d) STAR-CCM+, at the face velocity of 1.06 m/s.

Figure 3.7 (c) and (d) show the particle tracking results with the two CFD programs. The particle trajectories shown are from the entire inlet surface. Note that particle tracks with high velocity at the vertical level of the fibers are actually located close to the symmetric boundary of the domain, where the air velocity is high. The

particle trajectories near the fiber wall, which should have lower velocities, are mostly blocked by these high-velocity particle tracks in this view.

The velocity contour map in Figure 3.7 apparently cannot provide sufficient information about the flow profile in the downstream, i.e. if any flow separations. In order to find out the detailed velocity profile in the downstream side right behind the fiber, Figure 3.8 and 3.9 was used to show the velocity vectors in two face velocities: 1.06 m/s and 0.6 m/s. Reynolds number based on the fiber diameter d_f and the face velocity for these two cases are 4.70 and 2.44. The k-ε turbulent model and the laminar were used within these two cases. Both Figures 3.8 and 3.9 showed that the flow fields right after the fiber from two viscous models are almost the same. The Lagrangian particle tracking process also obtains the similar results. For the 1.06 m/s case, it clearly suggested that there were flow separations in the downstream side of the fiber. The low-velocity region contained two sets of flow recirculation. But this was not the same case in the 0.6 m/s case, which suggested no apparent separation occurred in such low Reynolds number case.

Another 'numerical experiment' had been done to simulate the flow field with the k-ε model at the unsteady condition in the face velocity of 1.06 m/s case. The flow field obtained from the steady simulation was used as the initial condition within the computational domain. The time step was set to be 10^{-4} s and 50000 steps were carried out. The results suggested that no significant difference was observed in both the flow field results and particle deposition efficiency for different physical time cases. Thus it is safe to presume in this case the Reynolds number is not high enough to cause unsteady

vortex and the steady simulation would be feasible and reliable to predict the filter efficiency.

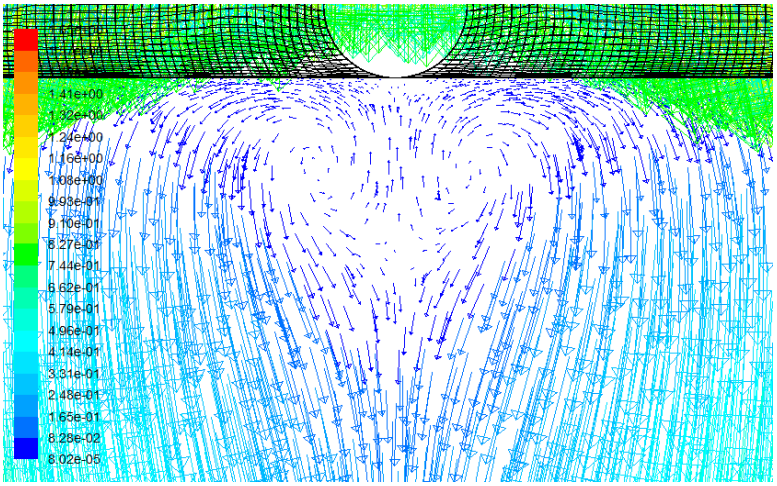

(a)

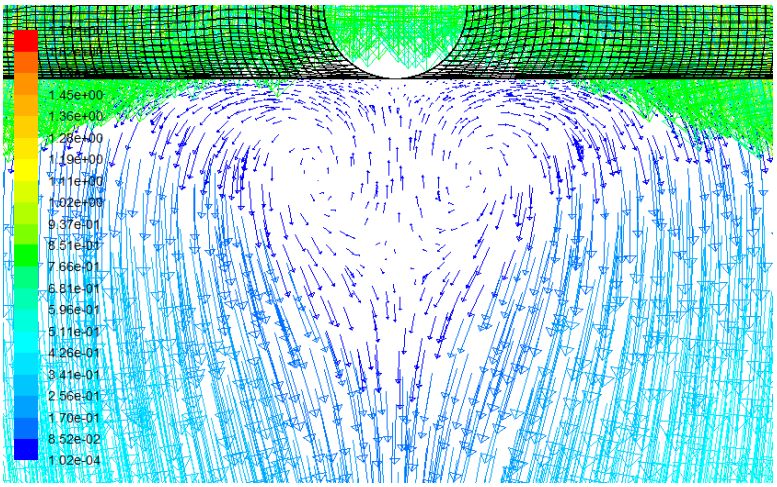

(b)

Figure 3.8 Flow field vectors in the downstream region of the fiber, at the face velocity of 1.06 m/s (Re = 4.70), using (a) the k-ε model, and (b) the laminar model.

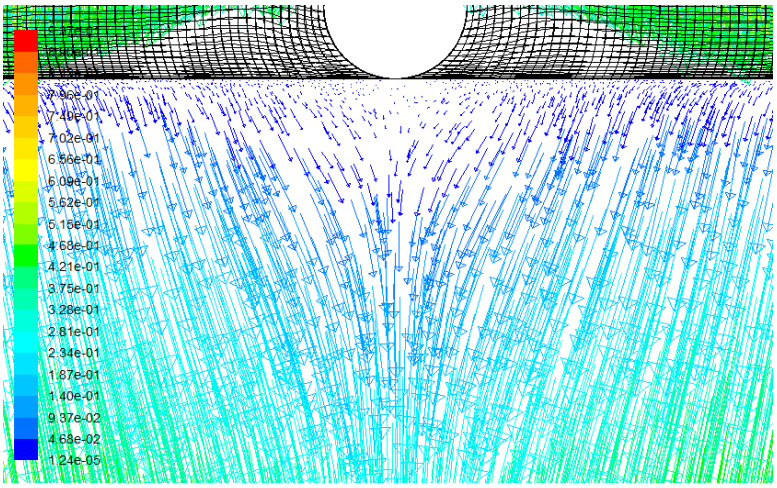

(a)

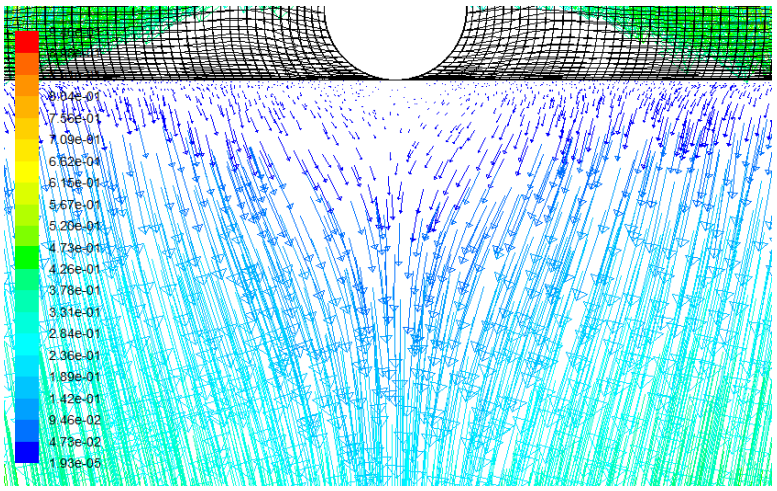

(b)

Figure 3.9 Flow field vectors in the downstream region of the fiber, at the face velocity of 0.6 m/s (Re = 2.44), using (a) the k-ε model, and (b) the laminar model.

Figure 3.10 shows the particle tracks of two different types. Both tracks are for 5 μm diameter particles with a density equal to that of water. Track A goes through the virtual surface (concentric with the fiber wall with a 2.5 μm gap) but not captured by fiber in standard Lagrangian particle tracking; Track B terminates on the fiber surface.

Track A represents that of a particle that would deposit by interception, while Track B represents that of a particle that deposits by impaction. As discussed before, programs do not recognize that interception would occur for particle track A. However, standard functions of these CFD programs are able to record the event that a particle track (trajectory of the center of a particle) comes within on particle radius from the fiber, in other words, go through the virtual surface.

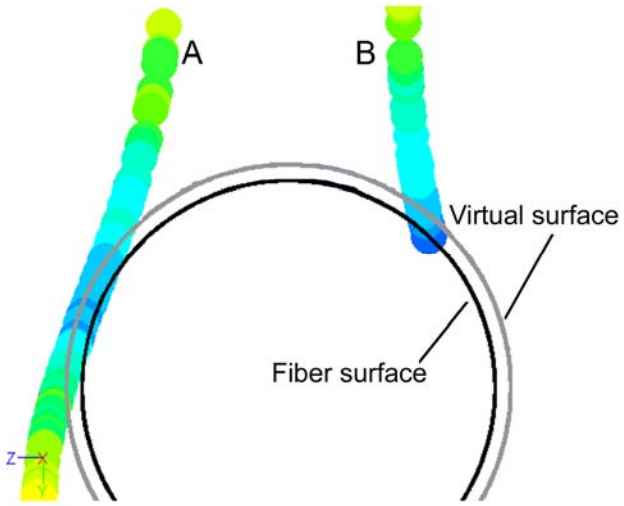

Figure 3.10 Particle trajectories (Impaction and Interception) for 5 micrometer particle.

3.2.2 Comparison between CFD Programs and Against Experimental Results

Simulations were done based on the screen whose parameters are shown in Table 2.1, at face velocity of 0.213, 0.6 and 1.06 m/s, particle diameter of 4~20 micrometer. Han (T. Han, 2007; T. Han, et al., 2009) used the same electroformed screen in experimental test to find the collection efficiency. Our simulation results were compared to Han's experimental data in same conditions.

Figure 3.11 shows results of the total, impaction and interception deposition efficiency obtained with the two CFD programs, along with the experimental results of total deposition efficiency from Han (T. Han, 2007) at the same flow condition (face velocity 1.06 m/s). Two commercial CFD packages, ANSYS FLUENT and STAR-CCM+ apparently provided the similar results in predicting the efficiencies (in total, by impaction or by interception), which only differed by 1.4% for total collection efficiency. Three deposition efficiencies were defined and calculated using Equation (2.5) ~ (2.10).

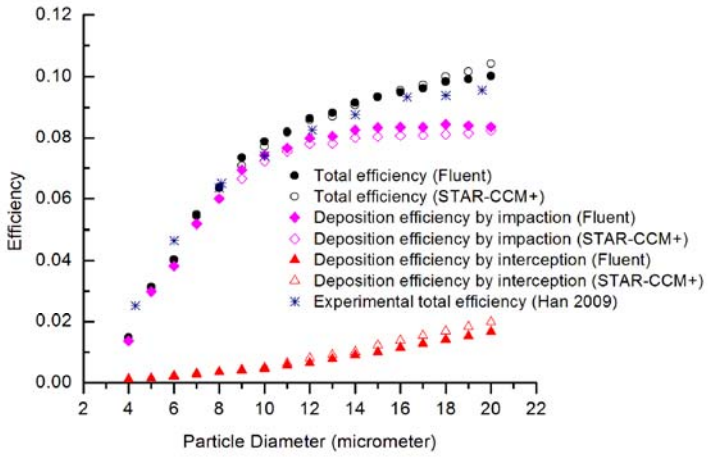

Figure 3.11 Comparison between FLUENT and STAR-CCM+ in simulations of total, impaction and deposition efficiency by interception at the face velocity of 1.06 m/s.

Interception efficiencies obtained with STAR-CCM+ were a little higher than that from FLUENT. This could be caused by minor difference of the simulated flow fields by the two CFD tools. Another possible reason is that in STAR-CCM+, virtual

surfaces consisted of two crossing cylinders, and the intercepted particles might be double counted in the crossing region of two cylindrical surfaces. In this case, it can conclude that two CFD tools have a good agreement, and thus the study mainly used FLUENT-based simulation efficiency results for discussion below.

Figure 3.12 provided the comparisons of the experiments and the CFD-based results of total, impaction and deposition efficiency by interception at all three face velocities, based on the Stokes number of particles. As shown in Figure 3.12, the CFD-based (by FLUENT) screen efficiency results not only have the proper trends, but they are also in good quantitative agreement with the experimental results. The root-mean-square normalized error with all available experimental data, defined as Equation (2.14), was 6.2% for CFD-based total efficiency. And it seems that after introducing interception mechanism with virtual surface model, CFD tools could predict collection efficiency for filtration electroformed screen. It was obvious that for larger particles, interception accounts for a larger fraction of the total deposition. In these cases, neglecting interception in CFD modeling would significantly under-estimate the total deposition.

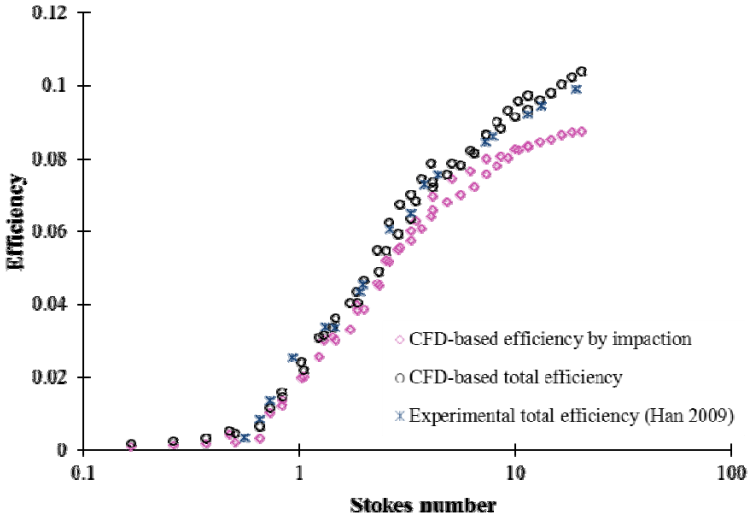

Figure 3.12 Comparison of experiment and CFD-based results of total, impaction and deposition efficiency by interception at all three face velocities.

3.2.3 CFD-Based Results Compared against Empirical Correlations

Deposition efficiency results calculated from the empirical correlations (as described in Table 2.2) are shown in Figure 3.13. The CFD-based results of deposition efficiency by interception are also shown in the figure for comparison.

The discrepancy between the empirical correlations was greater than the difference between the two CFD programs. This may be because each expression is empirically adjusted for a given range of particle size, fiber size, and/or flow regime, and hence not accurate for a wide range of parameters. However, the FLUENT-based deposition not only has the same trends comparing to the theoretical calculation, it also has a good agreement with the average interception value of all the correlations cited (with root-mean-square deviation of 4.9% with FLUENT results for particle size range of 4~20 micrometer, using Equation 2.14). The STAR-CCM+ based results seem to be

higher than the average interception correlation value due to possible reasons mentioned earlier, but still with a similar trend.

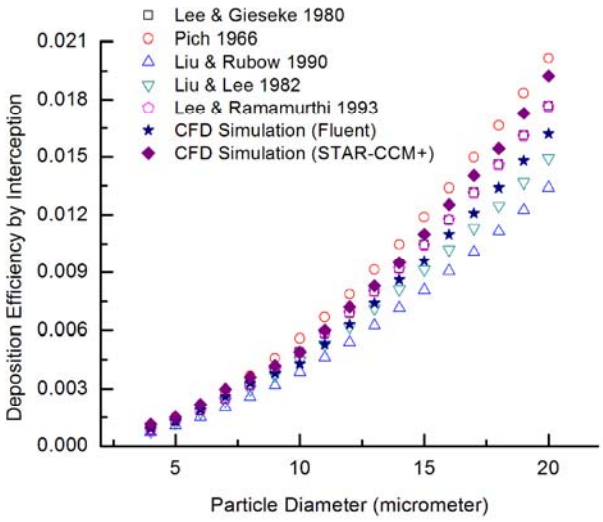

Figure 3.13 Comparison of deposition efficiency by interception between empirical correlations and CFD-based simulation.

3.2.4 Deposition Efficiency by Interception and Interception Ratio

In present research, the CFD results were utilized to determine the major parameters or conditions that affect the interception mechanism. Figure 3.14 shows the relation between interception parameter R (defined in Equation 1.9) and deposition efficiency by interception. As observed in Figure 3.14, the deposition efficiency by interception would increase significantly as R grows. And it could reach as over 1.6% when the interception parameter exceeds 0.3. So this could be enlightening in filtration study when estimate whether interception would be neglected or not. For a filtration

case, filter with fibers or fibrous screen, when the particle diameter is closed to or even larger than the fiber diameter, i.e. the interception parameter *R* would be approaching or even over unity, the interception effect could be significant enough and cannot be neglected. And it seemed that the deposition efficiency would significantly increase as *R* increased. Also apparently, the deposition efficiency by interception would have little difference as face velocity increased, which suggests that interception is a mechanism that does not depend on the normally flow velocity (Hinds, 1999).

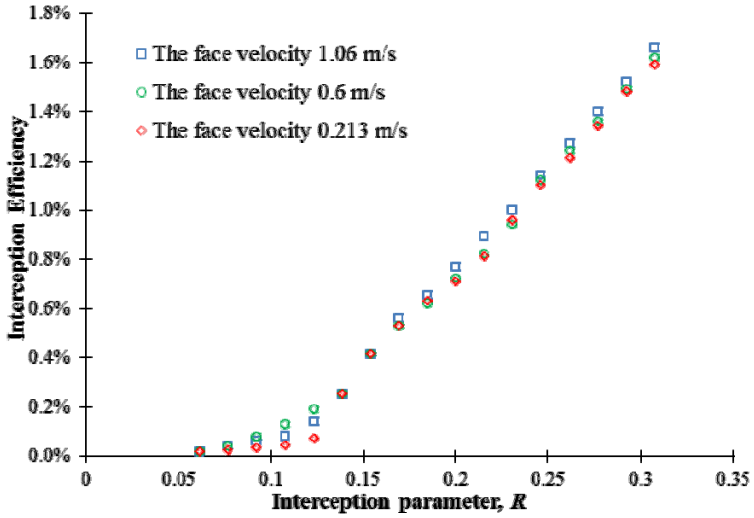

Figure 3.14 Deposition efficiency by interception in various face velocities.

Another comparison was made to reveal the significance of interception in collection efficiency. A new definition was made named the interception ratio, which equals the deposition efficiency by interception divided by total collection efficiency (impaction+interception):

$$R_{int} = \frac{\eta_{int}}{\eta_{total}} \tag{3.6}$$

Obviously, this ratio is utilized to show the relative effect of interception mechanism in the filtration study. Figure 3.15 gives the interception ratio value for various interception parameters and three face velocities are used in our simulation. As discussed before, as the interception parameter R increases (larger particles or smaller filtration dimensions), the interception itself would become more and more important. And note that, although absolute deposition efficiency by interception would be almost constant if only face velocity changed, the interception ratio would decrease as face velocity increases, because the impaction itself would obviously increase in this case. For impaction itself, as air flows around the fibers, the impaction process is governed by the Stokes number (S_{tk}), the fraction open area, and the fiber Reynolds number, Re_f, which is calculated based on the velocity, U, in the screen, Parameters are given in the Symbols and Abbreviations section. The average velocity through the mesh openings, U, is related to the face velocity, U_0. So in terms of dimensionless number, if the particle size fixed, the interception ratio would decrease when the Stokes number or fiber Reynolds number increased. As consequence, in the case of the highest interception parameter (0.308) and lowest face velocity (0.213 m/s), intercepted particles may account for up to 19% of the total aerosol depositions in CFD simulation.

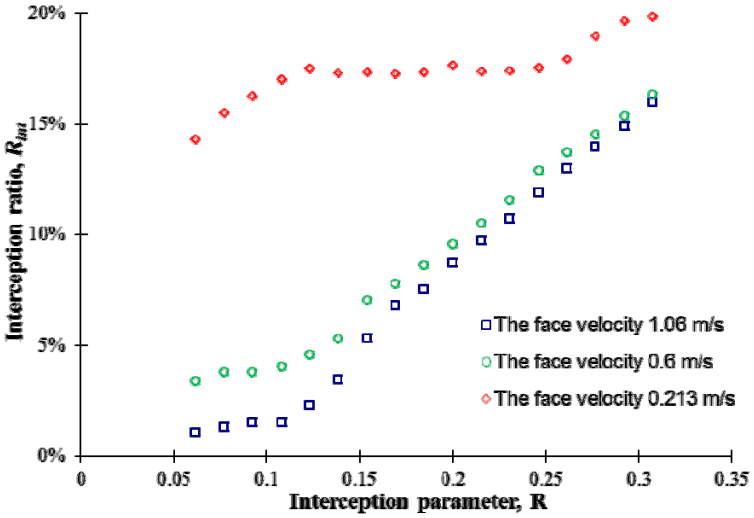

Figure 3.15 Interception ratio R_{int} in various face velocities.

3.2.5 Gravitational Effect in Filter Model

CFD simulation was also used to determine the effect of gravity on particle collection efficiency. The approach used here was to first conduct the particle tracking without including the gravitational force, and then repeat the calculations with gravity included. The gravitational force was set to be in the direction the same as the face velocity. At the higher face velocity (0.6 and 1.06 m/s), the CFD-based total efficiency was essentially the same for all particle sizes whether gravity was considered or not. However, at the face velocity of 0.213 m/s, as shown in Figure 3.16, the gravitational force would increase up to 6.9% of the total efficiency. At low face velocity, the gravitational effect is more significant because of the longer residence time of the particles in near-wall region could cause deposition velocity due to gravity more relatively significant. However, for the deposition efficiency by interception, the

gravitational effect seems to have limited effect even in this low face velocity case. Only less than 1.2% change would occur for deposition efficiency by interception.

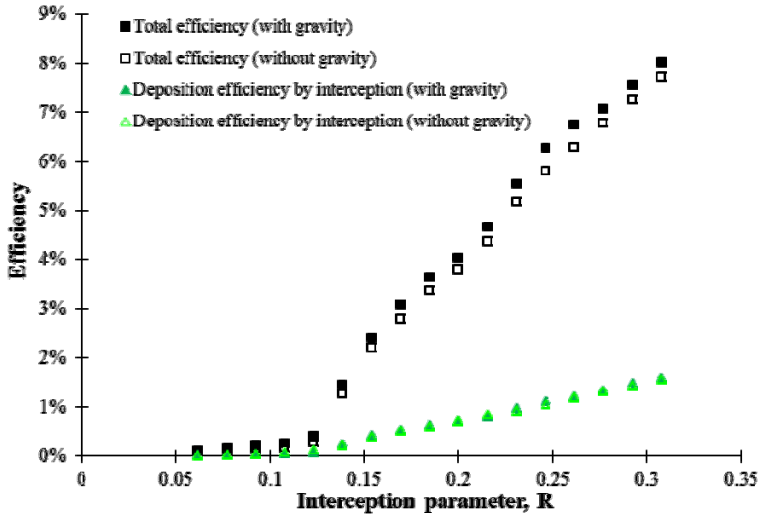

Figure 3.16 Gravitational effect on total and deposition efficiency by interception at the face velocity of 0.213 m/s.

3.3 Turbophoresis Simulation Results

Turbulence model, mesh resolution, and wall treatment all had significant effects on the accuracy of the CFD simulation of turbulent deposition. LES and RSM produced the most accurate results, when using the highest mesh resolution and the all-y+ wall treatment.

3.3.1 Effect of Turbulence Model

Flow simulation in a vertical straight pipe was done with various turbulence models: k-ε, k-ω, Reynolds stress model (RSM) and LES. The Lagrangian particle

tracking were carried out to evaluate the deposition based on turbulent flow filed simulation. Penetration through the pipe was simulated with aerodynamic particle sizes of 1 ~ 20 micrometer and the results were shown in Figure 3.17 for two separated Reynolds number cases, together with experimental data from Liu and Agarwal (Benjamin Y.H Liu & Agarwal, 1974) and 2D simulation data from Parker (Parker, et al., 2008) with RSM model.

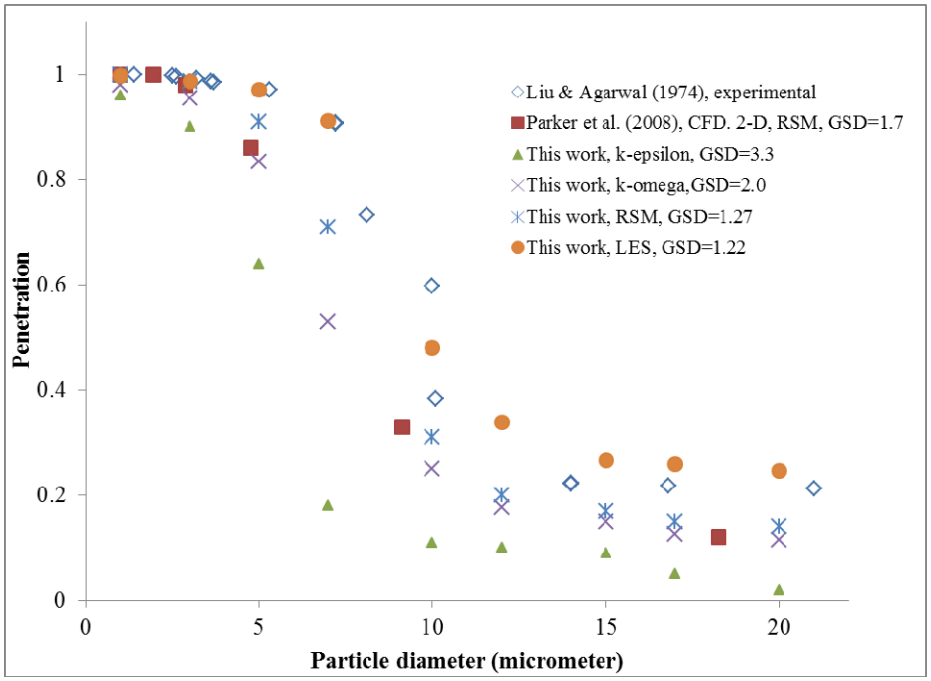

(a)

Figure 3.17 Penetration through the vertical pipe against particle diameter for different turbulent models in the case when (a) Re = 10000, (b) Re = 50000. Experimental data from Liu and Agarwal (Benjamin Y.H Liu & Agarwal, 1974) and 2D CFD simulation from Parker (Parker, et al., 2008) using RSM.

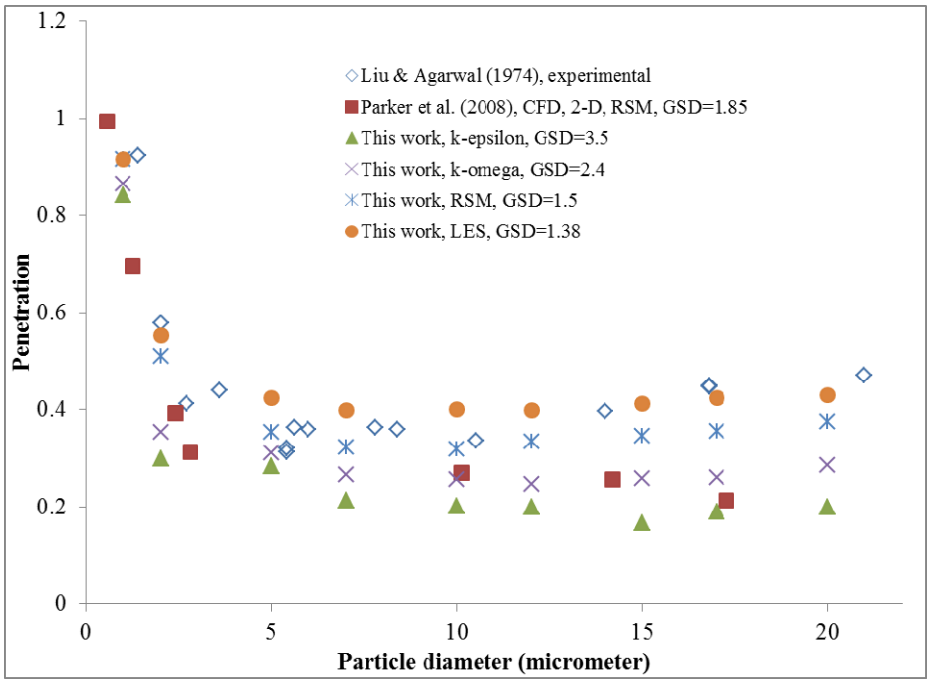

Figure 3.17 continued. (b)

The results show that moderate deviations occur in very small particles for different models compared to the experiments. But both in Re = 10000 and 50000 cases, for particle size larger than 3 micrometer, the simulations based on all three RANS models (k-ε, k-ω and RSM) generally under-predict the pipe penetration. Among RANS model, the RSM had a better agreement compared to experiments. For large particles, the penetration decreasing would slow down as particle size increased, which might be because the inertia makes the large particles less able to follow the fluid fluctuations.

For LES model, better agreement could be observed as particle size increased, but for larger particles (around 10 micrometer), LES appears to be over-predict the penetration, which is the opposite compared to the RANS simulation. Also in Re= 50000

case, LES seems to have a good agreement again when the particle size approaches to 20 micrometer.

The variation in predicted dimensionless deposition velocity with particle dimensionless relaxation time is shown in Figure 3.18 for the four turbulence models. The experimental data of Liu and Agarwal (Benjamin Y.H Liu & Agarwal, 1974) for both Reynolds numbers and the 2D RSM simulation result from Parker (Parker, et al., 2008) are also shown on this plot. Compared to the published experimental results, the geometric standard deviations (GSD) are calculated for each turbulent model used in this simulation. GSD for k-ε, k-ω, RSM and LES models were 3.4, 2.2, 1.37 and 1.29, separately.

Apparently, for $10 < \tau_+ < 1000$ (approximately 10 μm< d_p <100 μm for Re=10000, and 2 μm< d_p <25 μm for Re=50000), all four turbulence models perform reasonably well, predicting a dimensionless deposition velocity within approximately a factor of less than 2 of the experimental data, although it seemed more significant deviations in penetration predictions for k-ε and k-ω models in Figure 3.17. However, for $\tau_+ < 10$ region, while penetrations predicted earlier shown moderate agreement with experiments, the simulated deposition velocity varied very strongly compared to experimental data with growth of the relaxation time, especially for two isotropic turbulent models. These two isotropic turbulence models (k-ε and k-ω) seemed to fail to capture the deposition behavior and both over-predict the deposition velocity at small relaxation times by approximately 2~3 orders of magnitude. On the other hand, the anisotropic RSM and LES performed much better, capturing the log-linear relaxation

time dependence in this region (as suggested by Liu (Benjamin Y.H Liu & Agarwal, 1974) and Guha (Guha, 2008)), although still slightly over-predict the deposition velocity.

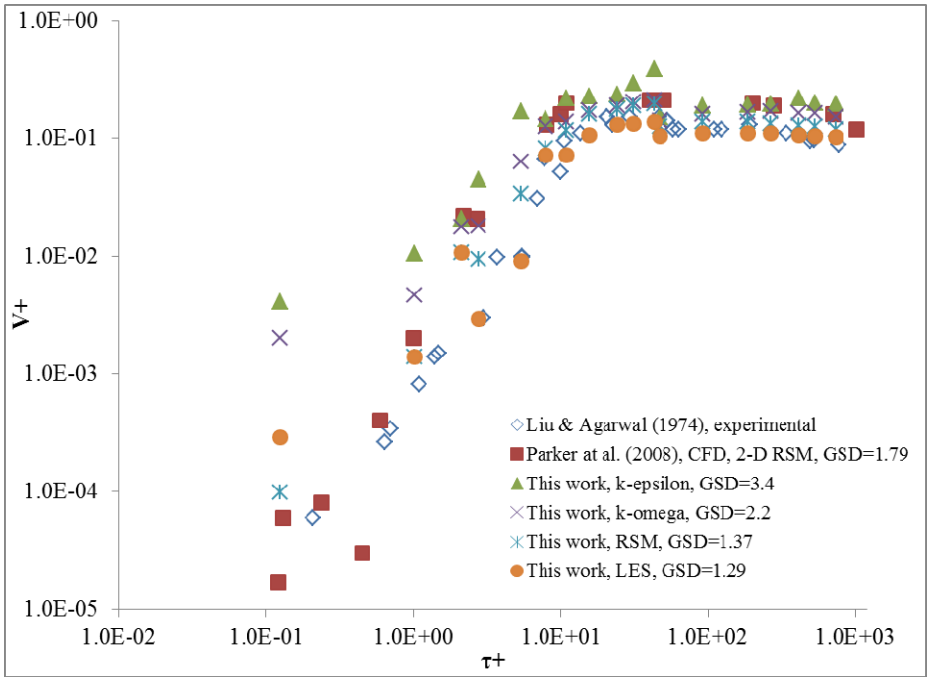

Figure 3.18 Dimensionless deposition velocity against dimensionless particle relaxation time for different turbulent models in both Re cases, with GSD values compared to experimental data from Liu and Agarwal (Benjamin Y.H Liu & Agarwal, 1974). 2D CFD simulation data from Parker (Parker, et al., 2008) using RSM is also included.

This STAR-CCM+ simulation could also provide the turbulence kinetic energy (TKE) or the wall-normal velocity fluctuation distribution. From the TKE results gained by simulation (see section 3.3.2), it showed that higher flow Reynolds number would cause a more intense turbulent effect in core-region and at near-wall region and higher

TKE peak with greater decreasing gradient in near-wall viscous sub-layer. In the core region within the pipe, the TKE slightly increased against the radial distance from central axis, then a peak exist for each turbulent model in the near-wall region. After the peak, the TKE would sharply decrease to 0 at wall surface due to no-slip boundary condition.

For particle size greater than 1 μm, little diffusion effect would influence on particle deposition in vertical pipe flow, and turbophoresis effect would dominate turbulent deposition. So in this case, as the driven force of turbophoresis, the predicted near-wall TKE gradient would have crucial influence on particle deposition rate gained by CFD simulation: greater TKE or the wall-normal velocity fluctuation gradient would cause a higher deposition velocity and overall deposition rate. The inability of the isotropic models to capture the damping of the wall-normal fluctuations in the near-wall region was believed to be the reason of their over-prediction of the wall-normal velocity fluctuation distribution. Although more convergence time are needed for the RSM and LES compared to an isotropic model, the particle tracking procedure, which can be a considerable part of the overall solution time, should be independent to the chosen turbulence models.

Based on these results, considering RANS models, greater decreasing gradient would possibly cause a lower penetration prediction in Guha-defined Regime II (Turbulent diffusion-eddy impaction area) (Guha, 2008), which refer to particles larger than 5 micrometer in Re =10000 case and particle size range of 3 ~ 14 micrometer in Re = 50000 case. In this particle size region, turbophoresis would have dominating

influence on particle deposition. So if CFD turbulent modeling has deviations or errors in predicting the near-wall TKE gradient, deviations or errors would occur in predicted deposition through Lagrangian particle tracking in CFD simulation, which is based on turbulent flow modeling. For instance, over-predicting the wall-normal velocity fluctuation using k-ε model, would over-predict the turbophoresis effect, which should be dominant in Regime II on aerosol deposition, and directly leads to over-predict of particle deposition rate in this regime. On the contrary, LES modeling seemed to slightly under-predict the deposition (over-predict the penetration) in Regime II compared to experiment. This leads to the possibility that LES modeling might provide a lower kinetic energy gradient at near-wall region compared to the real physical case, but was relatively closer to experiment compared to the RANS models did. Thus, penetration result obtained by LES seemed to have a better agreement to experiments. If this hypothesis above is true, the real physical wall-normal velocity fluctuation distribution could lie between LES and RSM, which could be validated in future PIV test.

For the particle sizes used in this study, it is reasonable to neglect the deposition effect due to diffusion. Thus, turbulent effect (turbophoresis) would be the dominant effect on aerosol deposition under such flow and particle condition. Note that although different turbulent models, wall functions or mesh resolutions were applied to derive the flow field in this case, the same Lagrangian particle tracking method was used in CFD code, which was based on the obtained turbulent flow field information. Therefore, any deviations in particle deposition prediction among each case would generally due to deviations coming from the flow field modeling (using different turbulent models, wall

functions and mesh resolutions). That is to say, deviations or errors in predicting near wall gradient of wall-normal velocity fluctuation (driving force of turbophoresis) would also cause difference in aerosol deposition results. However, these deviations due to choices of different turbulent models, wall functions and mesh resolutions would not influence on the analysis about the relation between the wall-normal velocity fluctuation gradient and deposition velocity. In order to evaluate this relation, the first step is to transformation of non-dimensional parameters.

3.3.2 Mean Square Wall-Normal Fluid Velocity Fluctuation

Figure 3.19 shows the radial distribution of K_+ (the dimensionless term of $\overline{V_{fy}'^2}$) at half pipe length (0.51 m). As can be seen in the figure, simulations with the two isotropic RANS models (k-ε and k-ω) produced steeper gradient of K_+ than those with the RSM and the LES models. However, with any of the turbulence models, the dimensionless gradient appears to be independent of the Reynolds number. The fluid velocity fluctuation results of this study are similar to those reported by Parker et al. (Parker, et al., 2008).

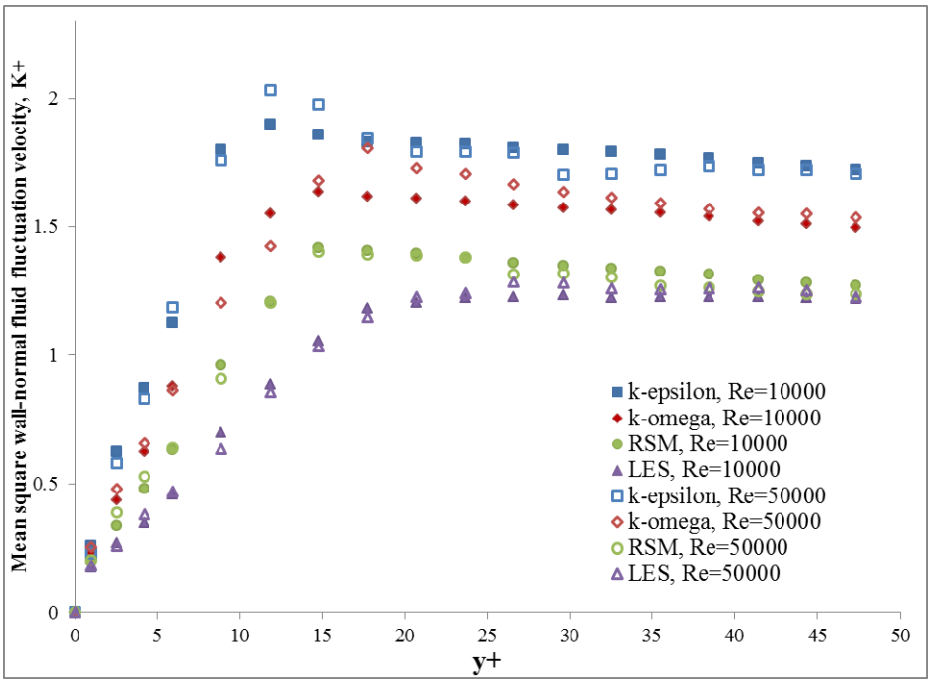

Figure 3.19 Radial distribution of dimensionless mean square wall-normal fluid velocity fluctuation ($K_+ = K / u_*^2$) at half pipe length, each data set containing two Reynolds number cases.

3.3.3 Effects of Mesh Resolution and Wall Treatment

As shown in Figure 3.20, the accuracy of the turbulent deposition simulation was dependent on the mesh resolution. All simulations shown in Figure 3.20 were with RSM and the all-y+ wall treatment. Figure 3.20 shows that increasing the wall-adjacent cell size (increasing y_+ value) resulted in over-prediction of deposition; the number of the mesh prism layers shows a "convergence" trend that more prism layers would be more likely leading to accurate predicting, and no significance observed for simulations using 15, 20 and 25 prism layers; only when the wall-adjacent cell y_+ values were sufficiently low (around unity), the simulated deposition velocity was in good agreement with experiments.

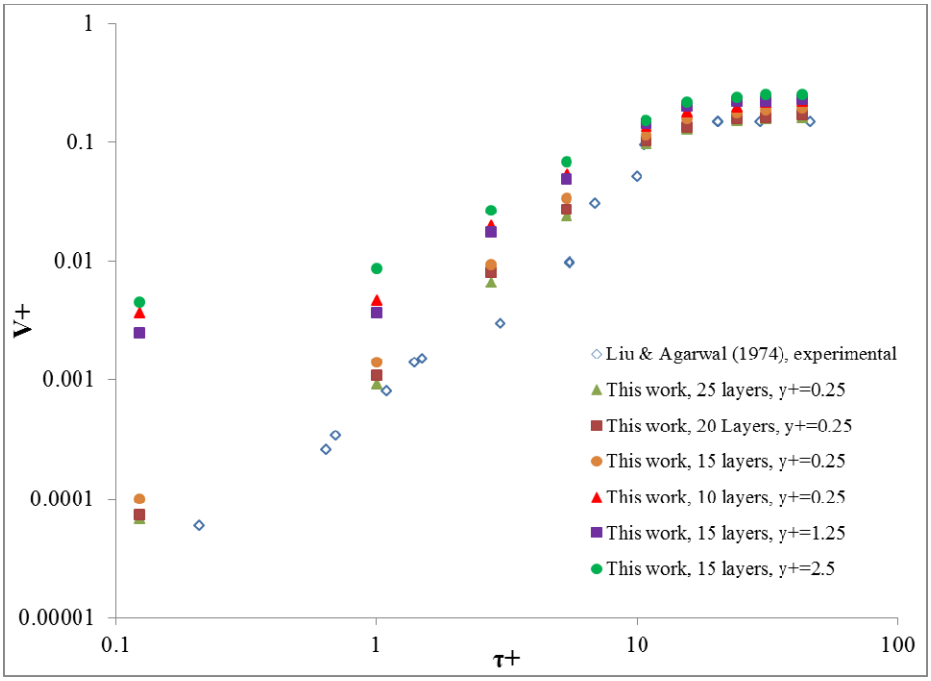

(a)

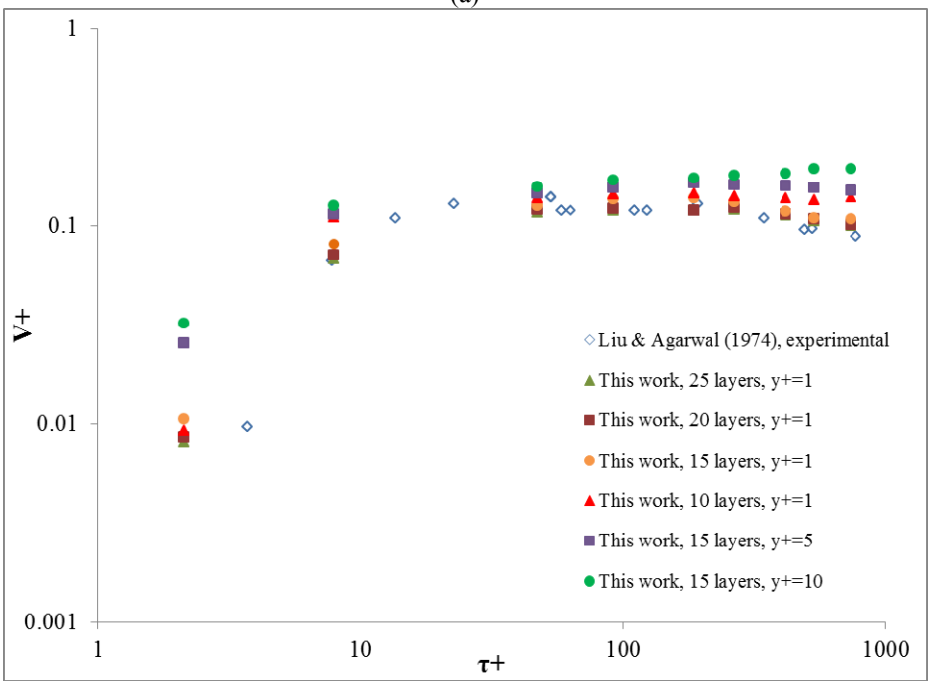

(b)

Figure 3.20 Dimensionless deposition velocity as a function of dimensionless particle relaxation time using the RSM turbulence model and various mesh conditions; both Reynolds number conditions included. (a) Re = 10000, (b) Re = 50000.

RSM simulation results using two types of wall treatment – high-y+ wall treatment and all-y+ wall treatment – are shown in Figure 3.21. Using the high-y+ wall treatment resulted in over prediction of particle deposition.

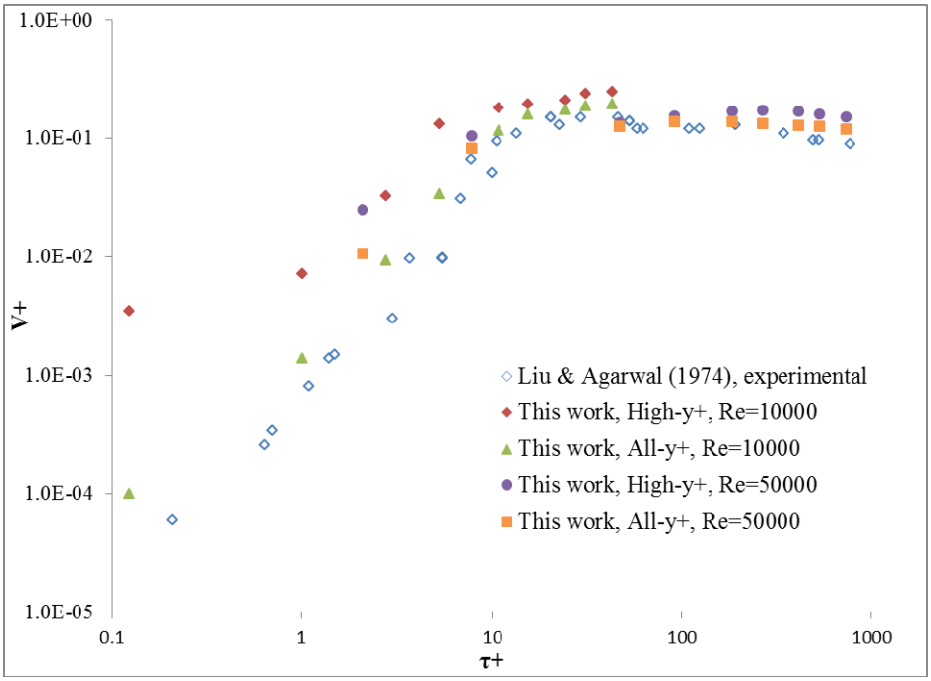

Figure 3.21 Dimensionless deposition velocity as a function of dimensionless particle relaxation time using the RSM turbulence model and different wall treatments in both Re cases. Experimental data from Liu and Agarwal (Benjamin Y.H Liu & Agarwal, 1974) was included.

According to the results shown in Figures 3.20 and 3.21, both mesh resolution and wall treatment had significant effect on the simulated particle deposition velocity.

The effects of wall-adjacent cell size and number of prism layers observed in this study are similar to that reported for 2-D CFD simulations (Parker, et al., 2008). Namely, the wall-adjacent cells should be sufficiently small such that the y+ value is on the order

of unity, and the number of prism layers should be sufficiently large (15~20 in this case) to cover the near-wall region, where steep gradient of turbulent velocity fluctuation exists. Part of the results are shown in Table 3.5, along with the corresponding particle deposition velocity and the simulated $\overline{V_{fy}'^2}$, for the case Re=10000. It is clear that the CFD configurations that predicted higher $\frac{d}{dy}\left(\overline{V_{fy}'^2}\right)_w$ also over-predicted the particle deposition velocity.

Table 3.5 Effects of mesh conditions and wall treatment on CFD-simulated dimensionless wall-normal velocity fluctuation gradient using the RSM model and all y+ wall treatment (unless otherwise noted), Re=10,000.

Number of prism layers	First layer y_+	K_+/y_+	V_+ (τ_+=1)
15	0.25	0.357	0.0014
	0.25 (High-y+)	0.438	0.0064
	1.25	0.405	0.0029
	2.5	0.428	0.0059
10	0.25	0.416	0.0038

3.3.4 The Particle Responsiveness Factor

As shown in Figure 3.22, the particle responsiveness factor (defined as Equation 2.20), obtained from CFD simulations, increases as the particle size decreases, and

eventually approaches unity; the results agree well with results obtained from empirical equations (Binder & Hanratty, 1991; Vames & Hanratty, 1988). For very small particles, the particle follows the fluid streamline perfectly, consequently the particle responsiveness factor approaches 1; for large particles, particle might not follow the flow velocity fluctuation because of its great inertia, and the particle responsiveness factor approaches 0. Note that, the relationship of α and τ appears to depend on the flow Reynolds number; for the same τ value, α is smaller at higher Re. This suggests that in a higher Reynolds number flow, there exists greater slip between the particle and the fluid. This may be explained by the particles inability to follow the higher frequency fluid velocity fluctuation in higher Reynolds number flows (P. L. Miller & Dimotakis, 1996; Shang & Xia, 2001).

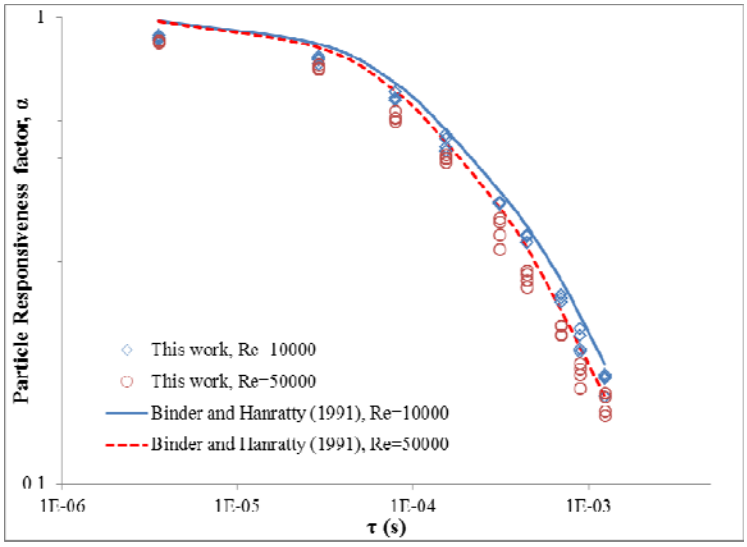

Figure 3.22 The particle responsiveness parameter α against particle relaxation time τ for CFD simulation in both Re cases; multiple data points at a given τ value correspond to multiple turbulence models.

3.3.5 The Turbophoresis Factor

The turbophoresis factor r_t as a function of the dimensionless particle relaxation time τ_+ is shown in Figure 3.23. Multiple data points for the same dimensionless particle relaxation time correspond to the various turbulence models used. Figure 3.23 suggests that the relationship between r_t and τ_+ is similar to the relationship between V_+ and τ_+. This is no surprise given that r_t is the ratio of dimensionless deposition velocity to dimensionless gradient of $\overline{V_{fy}'^2}$, and the latter appears to be independent of the pipe flow Reynolds number. Figure 3.23 suggests that, the effect of turbophoresis on particle deposition increases with particle size in the range $0.1 < \tau_+ < 10$; for larger τ_+ values, the effect of turbophoresis on particle deposition decreases with increasing particle size.

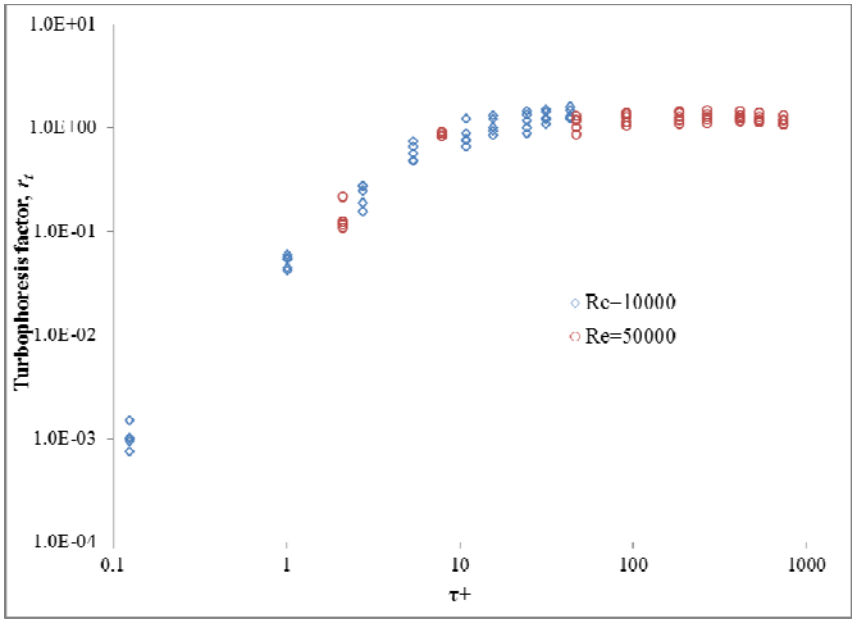

Figure 3.23 The turbophoresis factor r_t as a function of dimensionless particle relaxation time, both Re conditions included.

4. DISCUSSION *

Based on all the CFD-based simulations in *Result* section, some discussions on these mechanisms of particle transport and deposition would be necessary. Basically notes in the CFD modeling of aerosol transport and deposition were raised as following, and with relative difficulties and challenges.

4.1 Modeling on BSI-e Sampling Performance

4.1.1 Selection of Boundary Conditions

In this study, the boundary condition of the lateral boundary surfaces of the tunnel was set to be 'symmetric', which means that it is defined that the flow rate through these boundaries and the normal velocity both should be zero; and all the variable gradients at the surface should be zero. So strictly, this 'Symmetric' surface should be infinitely or sufficiently far away. Although space had been retained to avoid excessive flow blockage between the inlet and the lateral surfaces of the wind tunnel, the finite parameter could cause error to the flow field in numerical simulation and affect the particle trajectories. The error caused by dimensions of the domain boundaries was

---

*Reprinted with permission from "Computational fluid dynamics simulation of aerosol transport and deposition" by Tang, Y.J., & Guo, B. 2011. *Frontiers of Environmental Science & Engineering in China*, 5, 362-377, Copyright [2012] by GAODENG JIAOYU CHUBANSHE.

discussed in Appendix A. Various of dimensions of these 'Symmetric' boundaries were tested for the local wind speed and penetration gained by simulation. The results suggested that the potential error caused by the dimensions of the computational domain could be acceptable under present simulation conditions.

4.1.2 Particle Deposition on the Inner Plenum

Figure 3.2 also shows that a small number of particles deposited outside the main deposition region which refers to the upstream surface of the inner plenum (e.g. in the case of 24 km/h and 20 μm particle). The possible reason for this is because there could be some other aerosol flow with particles enter the intake, but also leave it without getting into the windows on the top (either fairly immediately, with a grazing contact, or all the way going "around" the inner and out at the downwind side). This would probably cause some depositions on the lateral side of the inner plenum due to the inertial impaction when the flow had a turn around the inner plenum. This part of flow could also be observed in Figure 3.1 (b).

4.1.3 Particle Loss

Some calculation was made to shows the fraction of the particles deposited on the inner plenum contributes to loss of the penetration. In present research, 400,000 particles were released from the inlet surface of the computational domain in simulation. For different wind speed, a number of particles, $n_{100\%}$ could be calculated as the ideal amount of particles going through the exhaust surface of BSI assuming there was no

wall loss, i.e. if all particles followed the flow streamline perfectly, $n_{100\%}$ of particles would transport through the exit of BSI-e.

So,

$$n_{100\%} = n_{total} \cdot \frac{Q_{exhaust}}{Q_{total}} \tag{4.1}$$

Remember that the $Q_{exhaust}$ is the flow rate through the BSI, which is 100 L/min in our case. The number of particle depositions contributes to loss of penetration could be calculated as:

$$n_{depo,wl} = n_{100\%} \cdot (1 - P_{sim}) \tag{4.2}$$

This parameter $n_{depo,wl}$ would represent how many sampling-loss particles, which were supposed to transport through the BSI exit in an ideal case, would deposit on the BSI-e surface.

Also, the particle number deposited on the inner plenum, $n_{depo,ip}$ could be found in the result of the Lagrangian particle tracking, which is also shown in Figure 3.2. Table 4.1 could show the comparison results of these two parameters, $n_{depo,wl}$ and $n_{depo,ip}$. It suggested that the fraction of the particles deposited on the inner plenum surface contributes to loss of penetration would decreased as wind speed increased. For various particle diameters at same wind speed, this fraction could increase as particle size increased at 24 km/h case, but minor difference was shown in 8 km/h case. It suggested that the inertial effect more significantly influenced the particle loss of penetration. And

particles mentioned in Section 4.1.2 might not be as sensitive to the inertial effect as the particle loss of penentration.

Table 4.1 The comparison of the number of particle depositions on the inner plenum and number of particle depositions contribute to the wall loss (with total particle number of 400,000).

Free wind speed 8 km/h			**Free wind speed 24 km/h**		
Particle Diameter μm	Number of particle deposited on inner plenum $n_{depo,ip}$	Number of particle contribute to the wall loss $n_{depo,wl}$	**Particle Diameter** μm	Number of particle deposited on inner plenum $n_{depo,ip}$	Number of particle contribute to the wall loss $n_{depo,wl}$
10	134	58	**10**	224	37
15	437	196	**15**	821	150
20	717	319	**20**	1327	340

4.2 Modification Model – Shrouded BSI

The purpose of the aerosol inlet research is to optimize the device and shape-modification to ensure to obtain a highly quality aerosol sampling efficiency in different flow conditions. It can be seen from the results and discussions above that there is still a fair amount of research needed, in order to comprehensively prove that the currently available CFD approach are indeed capable as a highly dependable design and development tool for aerosol sampling inlets. The CFD simulation could provide the predicted particle trajectories with fixed flow conditions, as a result of which, the particle depositions on wall surfaces of interest. This result could be helpful to show and prove the deposition mechanism for the aerosol particles in desired situations, and based

on which, some shape modification could be done to the geometric model to improve the function of aerosol inlet. So our research goal here is to accomplish the shape modification and try to reduce these particle depositions and increase the inlet efficiency, and the result would be evaluate in CFD simulation.

4.2.1 The Shrouded BSI-e model

Based on the CFD simulation and analysis of the original BSI-e model, the results suggested that the main particle loss and the particle depositions were most likely due to the inertial impaction, which would cause the particles with higher inertia to impact on the relatively lower positions on the upstream side of the inner plenum, since the higher inertia made the particles turn less when they were entering the circumferential intake of BSI.

For the BSI-e device, two shrouded eaves were added before the intake of the original BSI (as Figure 4.1). The major purpose of the shrouded structure is to change the streamline direction and reduce the turning angle near the intake which might reduce the inertial effect of particle motion. So in this case, the shrouded eaves might have some influence to improve the efficiency of original BSI-e, by reduce the particle deposition due to the inertial impaction on the upstream side of inner plenum.

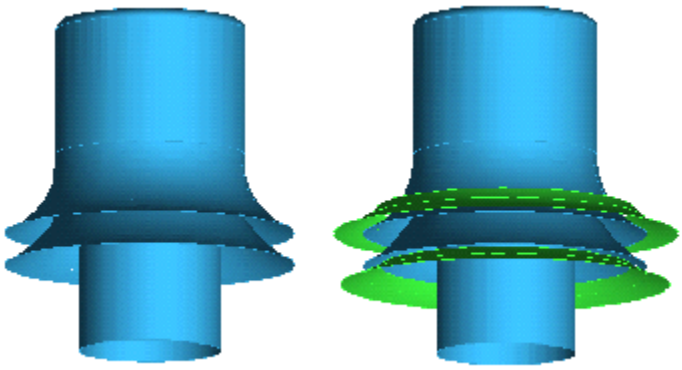

(a) (b)

Figure 4.1 The geometric models of (a) the origin BSI-e model and (b) the shrouded BSI-e model.

In this case, the same CFD simulation settings (computational domain, mesh generations, turbulence models, etc.) are applied for the shrouded BSI model. Based on CFD simulations, particle penetration was calculated for particles from 2 to 20 μm in aerodynamic diameter, at wind speed of 2, 8 and 24 km/h, and the fixed sampling flow rate of 100 L/min.

Predictions for penetration efficiency were compared between the original and the shrouded BSI model. Subsequent to the above determination, simulation was performed to get the particles' locations of deposition on the inlet walls, which would be a significant factor to influence on the penetration efficiency, could help understanding the turbulent flow pattern and particle trajectories, and modify the inlet shape toward this basis. For the modification of the inlet, two circumferential shrouded (Figure 4.1) eaves were added in front of the intake of BSI just to change the aerosol flow direction of the streamlines to ensure that the aerosol flow entering absolutely towards the tangential

direction of the curvilinear surface of inner plenum instead of horizontally as the free wind speed. The dimensions of these shrouded eaves were shown in Table 4.2.

Table 4.2 Important dimensions of the shrouded eaves.

Upper Shrouded Eave	Top and Bottom Spacer Dimension	Bottom Shrouded Eave	Shrouded Eave Intake Width	Eave Thickness
$D_o = 10''$ $D_i = 7.5''$	$0.375''$	$D_o = 9.5''$ $D_i = 7.25''$	$1.388''$	$0.1''$

4.2.2 Predicted Penetration Efficiency

For the modified Shrouded BSI-100 Model, the penetration results were shown in Figure 4.2, at the same flow conditions and particle sizes as the simulations on the original BSI model. Also comparison has been done for the penetration efficiency of these two models. It suggested that the shrouded model indeed increased the penetration and this difference would increase as the wind speed and particle diameter increased. This is because the main function of the shrouded structure is to change the flow direction and ensure that the aerosol flow entering absolutely towards the tangential direction of the curvilinear surface of inner plenum instead of horizontally as the free wind in the original BSI-e model. So, the advantage of the shrouded eaves is to reduce the inertial impaction mechanism when aerosol flow entering the circumferential intake of BSI, and decrease the opportunities of the particle depositions on the upstream side of the inner plenum. Since the inertial impaction mechanism would become more

significant at higher wind speed and larger particle size conditions, the penetration improvement of shrouded BSI would increase as wind speed and particle size increased. For this result in Figure 4.2, the largest absolute increasing amounts were 3.3% for the 2 km/h case, 4.2% for the 8 km/h case and 5.1% for the 24 km/h case.

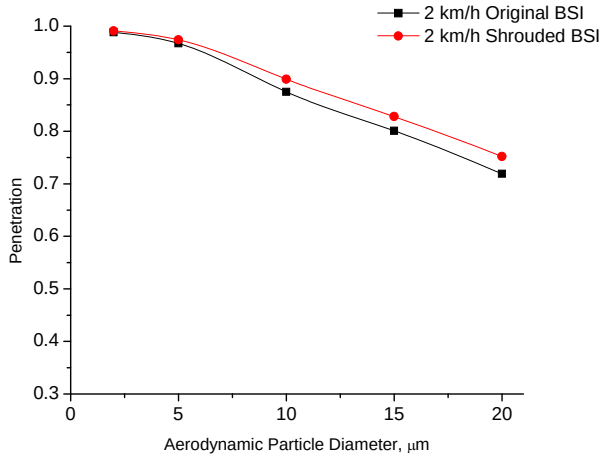

(a)

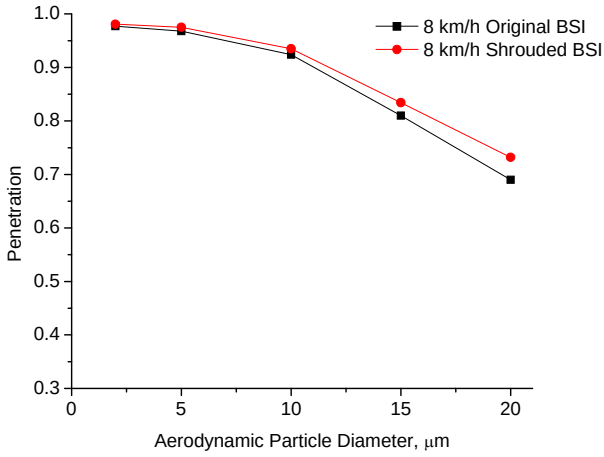

(b)

Figure 4.2 Comparison of penetration for shrouded and original BSI at the winds speed of (a) 2 km/h, (b) 8 km/h, and (c) 24 km/h.

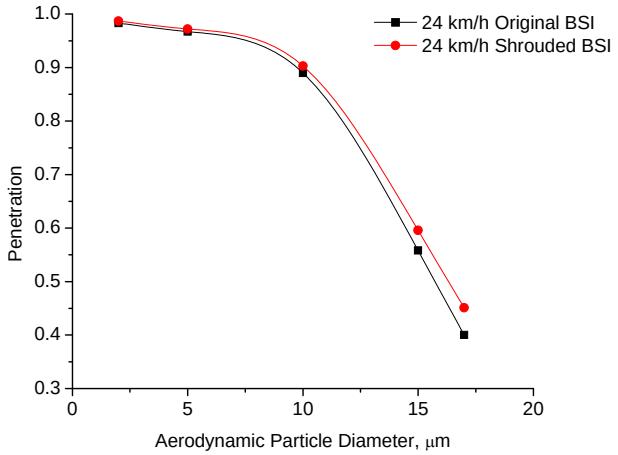

Figure 4.2 continued. (c)

4.2.3 Visualization of Particle Deposition on Inner Plenum and Bottom Shrouded Eave

Like the simulation on the original BSI-e model, the visualization of particle deposition was accomplished for the upstream of inner plenum and the upper surface of the bottom shrouded eave. The results were shown in Figure 4.3. Comparing to the simulation on the original model, there were less particle depositions on the inner plenum, which improves the penetration efficiency of the original BSI-e. Also, since the effect of the shrouded eaves would change the streamline direction, it seems that the differences of the deposited positions for particles with various of wind speeds and particle sizes became less significant comparing to the original model. In other word, from the deposition results at same wind speed, it showed that the particle deposition positions seemed to be close to each case with different particle diameters.

On the other hand, in visualization of the depositions on the bottom shrouded eave, it suggested that almost all particle depositions were located on the front surface and the inertial impactions still made the particle with higher inertia more depositions and the deposited region started at lower deposition locations. Also for the particles with higher inertia (large particle size or high wind speed), the deposited region on the surface of shrouded eave seemed to be wider than particles with lower inertia. It would be similar to the analysis above as it was expected.

Also according to this deposition results, another new idea of shrouded structure modification was provided. Since the research showed that a large number of the particles could hit and be stuck on the front surface of inner plenum due to the inertial impaction, the length dress-edge of the inner plenum could be reduced, and also extend the length of the bottom shrouded eave. This change could possibly make these particles which supposed to hit on the inner plenum by inertial impaction go through the gap between the inner plenum and the bottom shrouded eave, which means probably much fewer depositions on the front surface of inner plenum. So under this circumstance, some different dimensions of the shrouded eaves, such as longer eaves as mentioned above or curve planed eaves with less camber, could be considered in CFD simulation study in future.

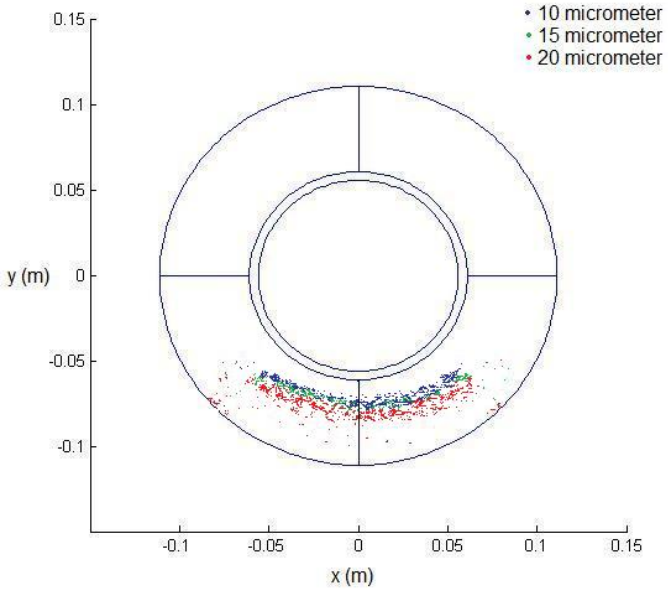

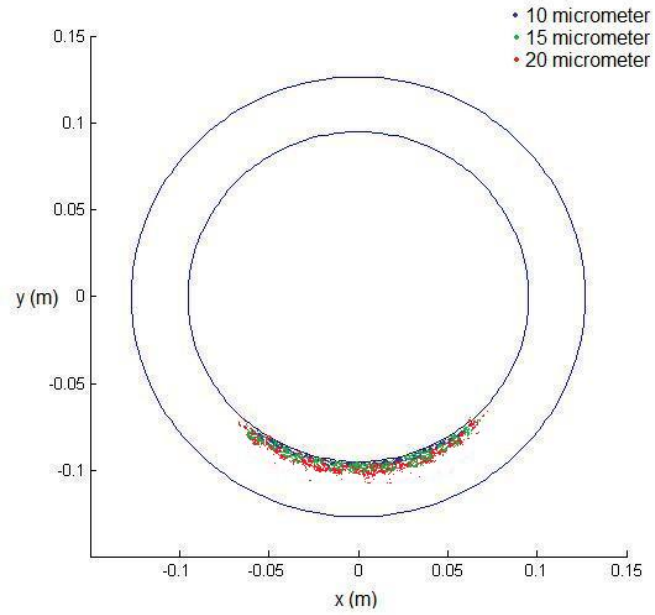

(a)

Figure 4.3 Top view of particle deposition on the upper surface of the inner plenum and upper surface of bottom shrouded eaves in Shrouded BSI-e model at the wind speeds of (a) 8 km/h and (b) 24 km/h.

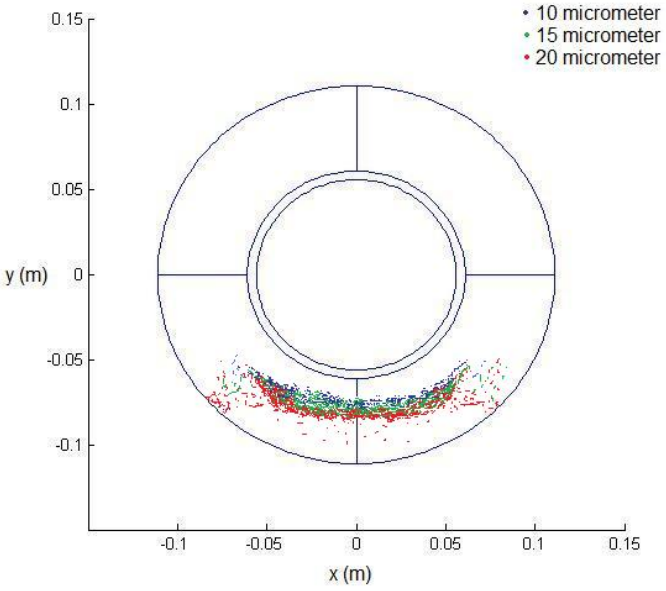

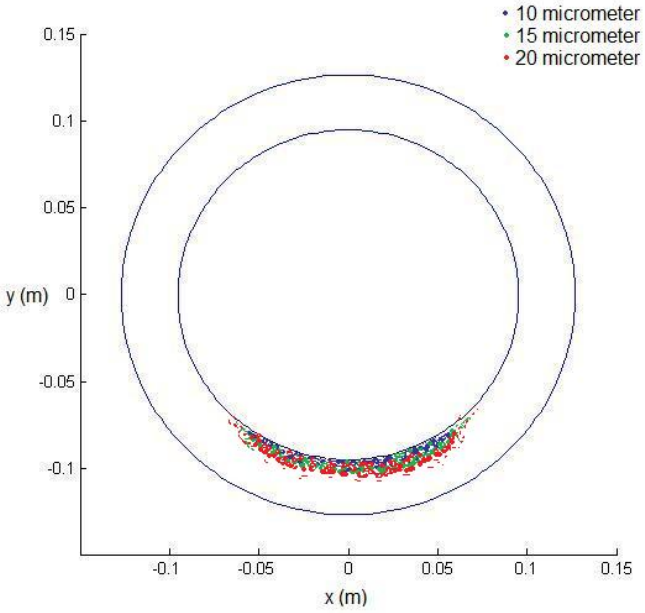

Figure 4.3 continued. (b)

4.3 Modeling on Interception via the Virtual-Surface Approach

A new approach using virtual-surface was utilized in order to account for particle interception in two common used CFD tools: ANSYS FLUENT and STAR-CCM+. This modeling strategy can be used to directly calculate the particle events captured by fiber walls due to interception with any fiber diameters when challenged with aerosols of any particles sizes, and then conclude with deposition efficiency by interception. More important, this method could quantitatively predict the particle interception via the standard function in commercial programs. The methods developed in this study, which can be readily validated and adopted by researchers in the field, would help to study the interception mechanism in filtration without the need for user defined functions or other subroutines.

The approach to create virtual surfaces in order to count intercept particles is shown in present work. The method successfully simulates the filtration process including particle impaction and interception without the need for user defined functions to account for interception. It can be readily validated and adopted by researchers in the field, and the comparison to the experimental data and the theoretical correlations also prove the feasibility of this approach. However, geometric limitations still remain for this approach. The virtual surface could be very difficult to build in a more complex geometric model, such as a randomly organized fibrous filter (S. A. Hosseini & Tafreshi, 2010), since extra considerations about the interaction between physical-virtual or virtual-virtual surfaces are necessary, which significantly increase the difficulty of the modeling process. Furthermore, for a large-dimension model such as an impactor or

inlet, the relative small distance between virtual and physical surfaces might also cause a tolerance problem when building the geometric models during the modeling process.

After all, this "virtual surface" approach should be especially useful for filter or screen models with cylindrical or elliptical fibers, in which case the "virtual surface" can be readily created. When more complex geometries are involved, creation of the "virtual surface" may become more challenging. Nevertheless, cylindrical or elliptical fibers are widely used geometries in filtration systems. Therefore, the "virtual surface" approach introduced in this study shall be useful in many modeling applications. Also, some developments are expectable for the virtual-surface approach to work together with user defined functions in order to extend its utilization.

4.4 Turbophoresis Modeling in the Vertical Straight Pipe

The effects of turbulence model, mesh resolution and wall treatment on the accuracy of turbulent deposition simulation observed in this study are similar to those observed in 2-D CFD simulations (Parker, et al., 2008). This suggests that similar criteria (e.g., near-wall mesh resolution, wall treatment) may be applied to both 3-D and 2-D CFD simulations of turbulent deposition, in order to achieve accurate results.

Simulations with RSM and LES turbulence models yielded similar levels of accuracy in terms of particle deposition velocity. The LES is associated with significantly higher computation cost – several weeks for flow field simulation and particle tracking, on a desktop computer with a 2.8 GHz processor, 8GB RAM running 8 parallel processes. Therefore, RSM – only a few days of computation time to produce

the flow field and particle tracking results – should probably be the choice of turbulence model for most practical turbulent deposition simulations.

The results in this study suggest that the accuracy of turbulent deposition simulation is critically dependent on the accuracy of the near-wall turbulence simulation. All the effects of the CFD model parameters on the accuracy of turbulent deposition appear to be through their effects on the accuracy of the near-wall turbulence simulation. It should be noted that all CFD configurations resulted in similar results of particle responsiveness factor, which agreed well with empirical results. In other words, the Lagrangian scheme in the CFD package can produce sufficiently accurate simulation of the particle random motion, as long as the turbulent flow field simulation is sufficiently accurate. This further suggests that the accuracy of the near-wall turbulence simulation is the most critical factor for turbulent deposition simulation.

The turbophoresis factor results should be useful for CFD simulation of turbulent deposition. Even though the typical value of the turbophoresis factor may vary with problem, what is presented in this study can at least serve as a reference point. For example, if one has the CFD simulation of a complex turbulent flow field such as that in a cyclone, and would like to know the relative contribution of turbulent deposition as opposed to deposition due to centrifugal acceleration, then the values of turbophoresis factor presented in this study will become useful.

The particle responsiveness factor computed from the CFD simulation and Lagrangian particle tracking results is apparently useful for validating the numerical model at a more fundamental level. The methodology used to obtain the particle

responsiveness factor suggests that the Eulerian description of turbulent deposition is useful for the validation of numerical simulations based on a Lagrangian approach.

4.5 Major Challenges in Turbulence Modeling on Aerosol Deposition

In spite of the significant progress in CFD simulation of particle transport and deposition in aerosol flows, many challenges remain in this field, especially in predicting turbulence effect in stochastic turbulent dispersions. Even with RSM or LES modeling, CFD tools could also be difficult to get accurate enough results here. The computational expense could also draw sufficient attention in any industrial applications. In this section, some challenges or opportunities were discussed.

4.5.1 Turbulence Modeling

The accuracy of the turbulent flow field simulated would be the first important condition to obtain an accurate enough particle transport and deposition results. Even though the more elaborate models such as LES may probably produce more accurate results, RANS models are still the first choice in most cases due to the balance consideration of computation economy. Unfortunately in current CFD studies, the turbulence solution is usually dependent upon the RANS model choice and the wall treatments, with no apparent universal rules for model and parameter selection. For simple geometry or simple flows, the mean flow field solutions with various turbulence models may be fairly similar, but the turbulence properties (e.g. turbulence kinetic

energy) can vary orders of magnitude from one model to another (Hoekstra, et al., 1999; Parker, et al., 2008).

Parker et al.(Parker, et al., 2008) compared in their research the turbulent friction velocities and wall-normal fluctuations obtained by several RANS model (RNG k-ε, RMS and k-ω SST) and significant deviations were observed between the turbulence models. All RANS models overpredicted the turbulent deposition velocity compared to the experimental measurements. Among those results, it seemed that the RSM model with a certain wall treatment could lead to relatively better agreement. The present study also got similar results, and it suggested that in most of cases, RSM could be the first choice in turbulence modeling on aerosol turbulent flow.

The high computational cost of LES still limits its utilization in CFD simulation. However it should be noted that, there appears to be a development of increasing use of LES in predicting particle transport and deposition. A cost-effectiveness assessment is still needed to validate LES-based simulations in predicting aerosol depositions. Currently, major efforts had been made using LES to evaluate the aerosol deposition in human respiratory tracts (Jayaraju *et al.*, 2008; Y. Liu, et al., 2007; Matida *et al.*, 2006), in channel or duct turbulent flow (Kuerten & Vreman, 2005; Lo Iacono *et al.*, 2005; Q. Wang & Squires, 1996), and in particle transport mechanism(Q. Wang, et al., 1997). It seems promising in these studies to use LES to improve the prediction of aerosol transport and deposition.

4.5.2 Turbulent Dispersion Modeling

When a RANS model was applied for turbulence modeling, the flow field information is insufficient to allow an exact mathematical description of the particle turbulence dispersion. The interaction between particles and turbulence can only be modeled using the turbulence flow field information provided by the turbulence modeling. Therefore, a turbulent dispersion model can be only as accurate as the turbulence model itself. If a turbulence model cannot correctly describe the turbulent profile, then the turbulent dispersion model would not be able to completely consider particle-turbulence interactions. Especially, due to the inability of RANS models to accurately simulate turbulence in the near-wall region, simulating turbulent depositions on walls is above all challenging. For example, Longest(Longest *et al.*, 2007) and Matida (Matida, et al., 2004) both suggested it was typically inaccurate to use particle dispersion models in combination with two-equation isotropic turbulence models. In fact, the isotropic turbulence models could not account adequately for the dampening of the wall-normal turbulent fluctuations, and consequently over-predict the particle deposition (Parker, et al., 2008).

In a near-wall turbulent flow region, a large gradient (Reynolds number dependent) of the wall-normal velocity fluctuation exits, because the velocity fluctuation must decrease from a high value in the fully developed turbulence core zone to zero at the wall due to the no-slip wall condition. This phenomenon turbophoresis causes particles to concentrate near the wall, and contributes to particle deposition onto the wall (Guha, 2008). Therefore, the accuracy of a RANS-based turbulent dispersion model

depends on the RANS model's ability to compute not only the near-wall velocity fluctuations, but also its gradient. However, even for a relatively simple pipe flow, different RANS models could produce very different results of near-wall velocity fluctuation distribution and particle deposition rate near the wall (Parker, et al., 2008).

However, it should be noted that in the near-wall region, some doubts would be raised for any turbulent dispersion models based on RANS models as completely feasible methods. First, turbulent dispersion models apparently work practically well in any "homogeneous" turbulence flows where the wall effect is not significant. For instance, the turbulent dispersion model in STAR-CCM+ was used to simulate the dispersion of particles released from one single point source in decaying grid-generated turbulence, and the simulation results agreed well with experiments (CD-adapco, 2008; Gosman & Ioannides, 1983). Secondly, it is possible to well predict turbulent deposition if an anisotropic RANS model, e.g. RSM, is used in conjunction with a proper wall treatment and sufficiently fine mesh (Parker, et al., 2008). The open question is whether an approach that works well for pipe flows will also work well for more complex flows, such as that in and around an omni-directional inlet.

With sufficient computational power, LES could be a better choice to simulate the turbulence and the particle dispersion/deposition. However, as discussed earlier, the LES approach may need more computational sources, and become too computationally expensive for simulations over significant time periods. It is not yet clear whether LES would be able to provide sufficiently higher accuracy of particle deposition to justify the added cost in general sampling cases.

4.5.3 Effect of Turbulent Dispersion

Noted among many cases, the turbulent dispersion is not the dominant particle deposition mechanism. One example here is the study on the performance of the aerosol sampling device (BSI), which was evaluated using RSM model without turbulent dispersion, and compared with the results from Tang et al. (Y. Tang, et al., 2010) which included dispersion. The device efficiency results comparison showed that in most of cases, the deviation with or without dispersion included was less than 5% of the total penetration efficiency (Figure 3.4). The results mentioned earlier suggested that the inertial separation would be the dominant mechanism to cause deposition in such case.

Another example was for the cyclone simulation. Hu and McFarland (Hu & McFarland, 2007) simulated the turbulent flow and the particle deposition in a cyclone without including a turbulent dispersion model, but their CFD-derived particle deposition rate were in an excellent agreement with obtained experimental data, which would as well suggest that the turbulent dispersion should not be a dominant mechanism to cause deposition. Furthermore, some currently researches (Y. Liu, et al., 2007; Longest, et al., 2007) on RANS simulation of respiratory system also showed that, for large particles, the regional aerosol deposition pattern could be likely independent to dispersion. It is apparently that the turbulent dispersion would not be a significant factor to cause particles deposit on the wall surface, if other dominant mechanism exists, such as inertial separations. This most likely would occur when there are curved and complex flow passages, and high flow rates or/and large particle sizes involved. While in such

cases, the simulation from most commercial CFD codes on aerosol deposition appear to be reliable.

In vertical pipe flows, however, turbulent dispersion is the dominant mechanism for particle deposition, and no other mechanisms would be so important (for large particles, Brownian motion could be neglected). But there are published empirical relations. Some empirical relations for calculating the rate of deposition of aerosol particles on the surface of vertical tubes were presented (Friedlander & Johnstone, 1957; Benjamin Y.H Liu & Agarwal, 1974; Mednikov, 1980) and also used for validation of CFD simulations (R. Gao & Li, 2011; Jiang, et al., 2010; Nerisson, et al., 2011; Parker, et al., 2008; F. P. Zhang & Li, 2008). On the other hand, the turbophoresis factor provided by the present study results should be useful at least serve as a reference point for the numerical research. Also, the methodology used to obtain the particle responsiveness factor suggests that the Eulerian description of turbulent deposition is useful for the validation of numerical simulations based on a Lagrangian approach.

In actual fact, CFD simulation of turbulent dispersion may be avoided if the computational resources do not allow for accurate modeling. For instance, the mean flow field obtained from a RANS model could be used to simulate particle deposition and still led to satisfactory results, if the inertial separation is dominant and turbulent dispersion only acts as a minor role. On the other hand, one may choose empirical relations or mathematical relationship as the turbophoresis factor, instead of the Lagrangian particle tracking in CFD tools to predict particle deposition, for a turbulent dispersion dominant case (e.g. vertical pipe flow).

5. SUMMARY AND CONCLUSIONS

In this article I provided a brief review of CFD modeling of particle transport and deposition in aerosol flows, followed by detailed CFD-based analysis on different particle transport and deposition mechanisms, such as particle inertial impaction, gravitational effect, lift force, interception, and most importantly, turbophoresis. These mechanisms were evaluated within different practical applications, which included aerosol sampling inlet, fibrous screen and vertical flow pipe. Two commonly used commercial CFD packages, ANSYS FLUENT (ANSYS Inc., Canonsburg, PA) and STAR-CCM+ (CD-adapco, London, UK) are applied in the CFD simulation of this study. According to the specific flow conditions, different flow viscous models were used to predict the flow field, then the Lagrangian particle tracking approach was applied to identify the particle trajectories and deposition rate.

In the study on BSI-e performance, turbulent flow field simulations and Lagrangian particle tracking were carried out for a 100 L/min omni-directional aerosol inlet. For the free wind speeds of 2, 8, and 24 km/h, particle penetration efficiency results based on the CFD simulations were in an excellent agreement with experimental results in previous studies. The root mean square normalized standard error, from comparing the simulation results with the experimental data group for all three wind speeds, was 3.8%. CFD-derived regional deposition pattern revealed that particle deposition took place essentially on the upstream surface of the inner shell, in a potion

where the flow was curvilinear and decelerating as it changed direction from horizontal to vertical. Although the inertial separation was the dominant mechanism of particle deposition, the gravitational effect was observed to contribute a significant effect at the lowest wind speed test (2 km/h). Based on the knowledge of regional particle deposition and the dominant deposition mechanisms, a six-parameter semi-empirical correlation equation was constructed to predict the penetration through the inlet. The semi-empirical correlation uses a Stokes number based on the free stream velocity and the width of the intake gap at the flow entrance to the BSI-e, a dimensionless gravitational settling parameter, and a velocity ratio for correction of the first two dimensionless numbers.

The findings of this study demonstrate that CFD simulation can provide information that is difficult to acquire through experimental measurements, such as regional distribution of particle deposition and the importance of specific deposition mechanisms, e.g. the gravitational settling, the Saffman force and the turbulent dispersion. Such information should be valuable for optimizing designs of aerosol inlets. Also, the correlation should be used as a scaling law and allow designers to predict the performance of an integrated inlet that may also include a screen and a pre-separator with known penetration characteristics.

Shrouded structure was added in the BSI-e model in order to improve the penetration efficiency of this sampling inlet. The predicted particle penetration efficiency in numerical simulation suggested that the shrouded structure could enhance the penetration and improve the efficiency of BSI-e. The visualization of particle depositions on the inner plenum and the bottom shrouded eave suggested that the

shrouded structure could weaken the effect of inertial motion and reduce the inertial impactions when entering the intake of BSI.

Secondly, for the fibrous screen simulation, a three-dimensional geometric model was built in this study to simulate the flow field and particle tracks about two crossing fibers. A new approach using "virtual-surfaces" was utilized in order to account for particle interception with two commonly used CFD programs: Fluent and STAR-CCM+. In particular, this CFD-based modeling strategy was demonstrated in comparing with experimental study on the same physical screen model, and calculation results from the existing empirical/semi-empirical correlations. The flow field and particle tracking results for both CFD programs were compared in present study with no obvious deviation observed. Also, comparing to the experimental data shows that the CFD simulation could predict the total collection efficiency very well after introducing the interception mechanism in particle tracking, and the root-mean-square normalized error is about 6.2%; while the results from empirical/semi-empirical correlations also tell that the deposition efficiency by interception predicted by CFD simulation – virtual-surface approach, is apparently within the right range and agree with the average value of former empirical estimations. The results after all prove that this modeling strategy is trustable in predicting filtration efficiency. In practical utilization, this virtual-surface approach can be used to calculate particle deposition due to interception with any fiber diameters when challenged with aerosols of any particles sizes. This approach does not require user defined functions or subroutines, and hence can be readily validated through peer review, and widely adopted by the research community.

Turbulent dispersion is probably the greatest challenge for CFD simulation on the aerosol transport and deposition. In this study, a 3-D CFD simulation of turbulent aerosol particle deposition was carried out, the results of which compared with published experimental results and previous 2-D simulations. The effects of the CFD modeling parameters were examined; a particle responsiveness factor and a turbophoresis factor were calculated based on the simulation results. Based on the results, the following may be concluded. The criteria for accurate simulation of turbulent deposition are similar for either 2-D or 3-D CFD models. Specifically, the Reynolds stress turbulent model should be used, with sufficiently small wall-adjacent cells to ensure a cell centroid y+ on the order of unity, sufficient number of prism layers to resolve the near-wall gradient of turbulent velocity fluctuation, and an "advanced" wall treatment (the "all y+" wall treatment in the case of STAR-CCM+). The more computationally expensive LES may not be necessary for simulating turbulent deposition. The particle responsiveness factor may be used for validating numerical simulations of turbulent deposition. The Eulerian description of turbulent deposition is useful for analyzing and validating the numerical simulations that are based on a Lagrangian approach. The "turbophoresis factor" quantitatively relates the deposition velocity and the gradient of the wall-normal turbulence fluctuation, and may be useful for assessing the importance of turbulent deposition in complex flows.

From the applications that sampled in this study, it is clear that CFD is a very useful tool, with significant limitations. Turbulent deposition is especially challenging for CFD modeling, due to the difficulty in profiling turbulent flow and the interaction

between the particle and the eddy. Limitations of CFD tools remain, for instance, the accuracy in simulating complex flow and the validation would be necessary.

Despite of this, CFD simulation, once validated with experiments, can be quite useful to carry out “numerical experiments” and based on which correlations useful for device design could be developed. It should be noted that CFD simulation or numerical calculation is able to provide sufficient information which might be difficult to obtain via physical experiments, or to reduce the cost and the number of experiments needed for device design. It is possible to take a balanced approach towards quantitative description of studied objects using CFD simulation in conjunction with empirical relations. Challenges still remain in CFD research and I am willing and motivated to make some contributions.

REFERENCES

ANSYS. (2008). ANSYS FLUENT 12.0/12.1 Documentation. ANSYS, Inc., Canonsburg, PA. http://www.ansys.com

Baehl, M.M. (2007). Ambient aerosol sampling inlet for flow rates of 100 and 400 L/min. M.S. Thesis, Department of Mechanical Engineering, Texas A&M University, College Station, Texas.

Belyaev, S.P., & Levin, L.M. (1974). Techniques for collection of representative aerosol samples. *J Aerosol Sci,* 5, 325–338.

Binder, J.L., & Hanratty, T.J. (1991). A diffusion-model for droplet deposition in gas-liquid annular-flow. *Int J Multiphas Flow,* 17, 1-11.

Bird, A.J. (2005). Use of numerical calculations to simulate the sampling efficiency performance of a personal aerosol sampler. *Aerosol Sci Tech,* 39, 596-610.

Bisgaard, H. (1995). A metal aerosol holding chamber devised for young children with asthma. *Eur Respir J,* 8, 856-860.

Broday, D.M., & Georgopoulos, P.G. (2001). Growth and deposition of hygroscopic particulate matter in the human lungs. *Aerosol Sci Tech,* 34, 144-159.

Cain, S.A., & Ram, M. (1998). Numerical simulation studies of the turbulent airflow through a shrouded airborne aerosol sampling probe and estimation of the minimum sampler transmission efficiency. *J Aerosol Sci,* 29, 1145-1156.

Casella, G., & Berger, R.L. (2002). *Statistical inference* (2nd ed.). Pacific Grove, CA: Thomson Learning.

CD-adapco. (2008). STAR-CCM+ 5.04.006 Guide and Documentation, http://www.cd-adapco.com/.

Chandra, S., & McFarland, A.R. (1997). Shrouded probe performance: Variable flow operation and effect of free stream turbulence. *Aerosol Sci Tech,* 26, 111-126.

Chen, Y.S., & Hsiau, S.S. (2008). A new method for measuring cake thickness by a powder pressure-displacement system. *Adv Powder Technol,* 19, 49-60.

Clift, R., Grace, J.R., & Weber, M.E. (1978). *Bubbles, drops, and particles*. New York: Academic Press.

Coroneo, M., Mazzei, L., Lettieri, P., Paglianti, A., & Montante, G. (2011). CFD prediction of segregating fluidized bidisperse mixtures of particles differing in size and density in gas-solid fluidized beds. *Chem Eng Sci,* 66, 2317-2327.

Darquenne, C. (2001). A realistic two-dimensional model of aerosol transport and deposition in the alveolar zone of the human lung. *J Aerosol Sci,* 32, 1161-1174.

Darquenne, C., & Paiva, N. (1996). Two- and three-dimensional simulations of aerosol transport and deposition in alveolar zone of human lung. *J Appl Physiol,* 80, 1401-1414.

Davies, C.N. (1966). *Aerosol science*. New York: Academic Press.

Deuschle, T., Janoske, U., & Piesche, M. (2008). A CFD-model describing filtration, regeneration and deposit rearrangement effects in gas filter systems. *Chem Eng J,* 135, 49-55.

Drobyshevsky, N.I., Zaichik, L.I., Mukin, R.V., & Filippov, A.S. (2009). Development and application of a diffusion-inertia model for calculating aerosol particle deposition from turbulent flows. *J Eng Thermophys,* 18, 271-278.

Fan, B., Mcfarland, A.R., & Anand, N.K. (1992). Aerosol-particle losses in isokinetic sampling probe inlets. *Environ Sci Technol,* 26, 390-394.

Fluent Inc. (2005). FLUENT 6.2 User's Guide. *Fluent Inc., Centerra Resource Park, 10 Cavendish Court, Lebanon, NH 03766*.

Fortes, F.J., & Laserna, J.J. (2010). Characteristics of solid aerosols produced by optical catapulting studied by laser-induced breakdown spectroscopy. *Appl Surf Sci,* 256, 5924-5928.

Fotovati, S., Tafreshi, H.V., Ashari, A., Hosseini, S.A., & Pourdeyhimi, B. (2010). Analytical expressions for predicting capture efficiency of bimodal fibrous filters. *J Aerosol Sci,* 41, 295-305.

Friedlander, S.K., & Johnstone, H.F. (1957). Deposition of suspended particles from turbulent gas streams. *Ind Eng Chem,* 49, 1151-1156.

Gao, P.F., Chen, B.T., Baron, P.A., & Soderholm, S.C. (2002). A numerical study of the performance of an aerosol sampler with a curved, blunt, multi-orificed inlet. *Aerosol Sci Tech,* 36, 540-553.

Gao, P.F., Dillon, H.K., Baker, J., & Oestenstad, K. (1999). Numerical prediction of the performance of a manifold sampler with a circular slit inlet in turbulent flow. *J Aerosol Sci,* 30, 299-312.

Gao, R., & Li, A.G. (2011). Modeling deposition of particles in vertical square ventilation duct flows. *Build Environ,* 46, 245-252.

Gimbun, J., Chuah, T.G., Choong, T.S.Y., & Fakhru'l-Razi, A. (2005). Prediction of the effects of cone tip diameter on the cyclone performance. *J Aerosol Sci,* 36, 1056-1065.

Gong, H.R., Chandra, S., McFarland, A.R., & Anand, N.K. (1996). A predictive model for aerosol transmission through a shrouded probe. *Environ Sci Technol,* 30, 3192-3198.

Gosman, A.D., & Ioannides, E. (1983). Aspects of computer-simulation of liquid-fueled combustors. *Journal of Energy,* 7, 482-490.

Griffiths, W.D., & Boysan, F. (1996). Computational fluid dynamics (CFD) and empirical modelling of the performance of a number of cyclone samplers. *J Aerosol Sci,* 27, 281-304.

Gu, F., Liu, C.J., Yuan, X.G., & Yu, G.C. (2004). CFD simulation of liquid film flow on inclined plates. *Chemical Engineering & Technology,* 27, 1099-1104.

Guha, A. (1997). A unified eulerian theory of turbulent deposition to smooth and rough surfaces. *J Aerosol Sci,* 28, 1517-1537.

Guha, A. (2008). Transport and deposition of particles in turbulent and laminar flow. *Annu Rev Fluid Mech,* 40, 311-341.

Han, T. (2007). Experimental and numerical studies of aerosol penetration through screens. PhD dissertation, Department of Mechanical Engineering, Texas A&M

University, College Station, Texas. Available online at: http://repository.tamu.edu/handle/1969.1/ETD-TAMU-1344.

Han, T., Haglund, J.S., Hari, S., & McFarland, A. (2009). Aerosol deposition on electroformed wire screens. *Aerosol Sci Tech,* 43, 112-119.

Happel, J. (1959). Viscous flow relative to arrays of cylinders. *Aiche J,* 5, 174-177.

Hinds, W.C. (1999). *Aerosol Technology - Properties, Behavior, and Measurement of Airborne Particles* (2nd edition). New York: Wiley-Interscience.

Hoekstra, A.J., Derksen, J.J., & Van Den Akker, H.E.A. (1999). An experimental and numerical study of turbulent swirling flow in gas cyclones. *Chem Eng Sci,* 54, 2055-2065.

Hosseini, S.A., & Tafreshi, H.V. (2010). 3-D simulation of particle filtration in electrospun nanofibrous filters. *Powder Technol,* 201, 153-160.

Hosseini, S.H., Ahmadi, G., Razavi, B.S., & Zhong, W.Q. (2010). Computational fluid dynamic simulation of hydrodynamic behavior in a two-dimensional conical spouted bed. *Energ Fuel,* 24, 6086-6098.

Hu, S.S., & McFarland, A.R. (2007). Numerical performance simulation of a wetted wall bioaerosol sampling cyclone. *Aerosol Sci Tech,* 41, 160-168.

Jayaraju, S.T., Brouns, M., Lacor, C., Belkassem, B., & Verbanck, S. (2008). Large eddy and detached eddy simulations of fluid flow and particle deposition in a human mouth-throat. *J Aerosol Sci,* 39, 862-875.

Jayaraju, S.T., Brouns, M., Verbanck, S., & Lacor, C. (2007). Fluid flow and particle deposition analysis in a realistic extrathoracic airway model using unstructured grids. *J Aerosol Sci,* 38, 494-508.

Jiang, H., Lu, L., & Sun, K. (2010). Simulation of particle deposition in ventilation duct with a particle-wall impact model. *Build Environ,* 45, 1184-1191.

Johansen, S.T. (1991). The deposition of particles on vertical walls. *Int J Multiphas Flow,* 17, 355-376.

Kasper, G., Schollmeier, S., Meyer, J., & Hoferer, J. (2009). The collection efficiency of a particle-loaded single filter fiber. *J Aerosol Sci,* 40, 993-1009.

Kim, C.H., & Lee, J.W. (2001). A new collection efficiency model for small cyclones considering the boundary-layer effect. *J Aerosol Sci,* 32, 251-269.

Kirsch, A.A., & Stechkina, I.B. (1978). The theory of aerosol filtration with fibrous filters. In *Fundamentals of Aerosol Science* (D.T. Shaw Ed.), New York: Wiley.

Kuerten, J.G.M., & Vreman, A.W. (2005). Can turbophoresis be predicted by large-eddy simulation? *Phys Fluids,* 17, 1.

Kuwabara, S. (1959). The forces experienced by randomly distributed parellel circular cylinders or spheres in a viscous flow at small rynolds numbers. *J Phys Soc Jpn,* 14, 527-532.

Landau, L.D., & Lifshits, E.M. (1987). *Fluid mechanics* (2nd ed.). Oxford, England: Pergamon Press.

Launder, B., Reece, G.J., & Rodi, W. (1975). Progress in the development of a Reynolds-stress turbulence closure. *J Fluid Mech,* 68, 537-566.

Launder, B., & Spalding, D.B. (1974). The numerical computation of turbulent flows. *Computer Methods in Applied Mechanics and Engineering,* 3, 269-289.

Lee, K.W., & Gieseke, J.A. (1980). Note on the approximation of interceptional vollection rfficiencies. *J Aerosol Sci,* 11, 335-341.

Lee, K.W., & Gieseke, J.A. (1994). Deposition of particles in turbulent pipe flows. *J Aerosol Sci,* 25, 699-709.

Lee, K.W., & Liu, B.Y.H. (1982). Theoretical-study of aerosol filtration by fibrous filters. *Aerosol Sci Tech,* 1, 147-161.

Lee, K.W., & Ramamurthi, M. (1993). Filter Collection. In *Aerosol Measurement: Principles, Techniques, and Applications*, New York: Van Nostrand Reinhold.

Lee, S.R., Holsen, T.M., & Dhaniyala, S. (2008). Design and development of novel large particle inlet for PM larger than 10 mu m (PM > 10). *Aerosol Sci Tech,* 42, 140-151.

Liu, B.Y.H., & Agarwal, J.K. (1974). Experimental observation of aerosol deposition in turbulent flow. *J Aerosol Sci,* 5, 145-148, 149-155.

Liu, B.Y.H., & Pui, D.Y.H. (1981). Aerosol sampling inlets and inhalable particles. *Atmos Environ,* 15, 589-600.

Liu, B.Y.H., & Rubow, K.L. (1990). Efficiency, Pressure drop and figure of merit of high efficiency fibrous and membrane filter media. In *Proceedings of the Fifth World Filtration Congress*, vol. 9.

Liu, Y., Matida, E.A., Gu, J., & Johnson, M.R. (2007). Numerical simulation of aerosol deposition in a 3-D human nasal cavity using RANS, RANS/EIM, and LES. *J Aerosol Sci,* 38, 683-700.

Liu, Z. (1993). Numerical Investigation of Particle Filtration Process in Fibrous Filters. Ph.D. dissertation, University of Wisconsin, Madison.

Lo Iacono, G., Tucker, P.G., & Reynolds, A.M. (2005). Predictions for particle deposition from LES of ribbed channel flow. *Int J Heat Fluid Fl,* 26, 558-568.

Longest, P.W., Hindle, M., & Das Choudhuri, S. (2009). Effects of heneration time on spray aerosol transport and deposition in models of the mouth-yhroat geometry. *Journal of Aerosol Medicine and Pulmonary Drug Delivery,* 22, 67-83.

Longest, P.W., Hindle, M., Das Choudhuri, S., & Byron, P.R. (2007). Numerical simulations of capillary aerosol generation: CFD model development and comparisons with experimental data. *Aerosol Sci Tech,* 41, 952-973.

Longest, P.W., & Xi, J.X. (2007). Effectiveness of direct Lagrangian tracking models for simulating nanoparticle deposition in the upper airways. *Aerosol Sci Tech,* 41, 380-397.

Ma, B., & Lutchen, K. (2009). CFD Simulation of aerosol deposition in an anatomically based human large-medium airway model. *Ann Biomed Eng,* 37, 271-285.

Matida, E.A., DeHaan, W.H., Finlay, W.H., & Lange, C.F. (2003). Simulation of particle deposition in an idealized mouth with different small diameter inlets. *Aerosol Sci Tech,* 37, 924-932.

Matida, E.A., Finlay, W.H., Breuer, M., & Lange, C.F. (2006). Improving prediction of aerosol deposition in an idealized mouth using Large-Eddy Simulation. *J Aerosol Med,* 19, 290-300.

Matida, E.A., Finlay, W.H., Lange, C.F., & Grgic, B. (2004). Improved numerical simulation of aerosol deposition in an idealized mouth-throat. *J Aerosol Sci,* 35, 1-19.

Mcfarland, A.R., Rodgers, J.C., Ortiz, C.A., & Moore, M.E. (1992). A continuous sampler with background suppression for monitoring alpha-emitting aerosol-particles. *Health Phys,* 62, 400-406.

Mcfarland, A.R., Wedding, J.B., & Cermak, J.E. (1977). Large particle collection characteristics of ambient aerosol samplers. *Environ Sci Technol,* 11, 387-390.

McKinnon, A.D., Bowyer, S.M., Hubbard, C.W., Miley, H.S., Perkins, R.W., Thompson, R.C., & Warner, R.A. (1998). Environmental measurements with a comprehensive Nuclear Test Ban Treaty radionuclide particulate monitor. *J Radioanal Nucl Ch,* 235, 115-119.

Mclaughlin, J.B. (1989). Aerosol-particle deposition in numerically simulated channel flow. *Phys Fluids a-Fluid,* 1, 1211-1224.

McMurry, P.H. (1999). A review of atmospheric aerosol measurements. *Atmos Environ,* 34, 1959-1999.

Mednikov, E.P. (1980). *Turbulent Transfer and Deposition of Aerosols*. Moscow: Nauka.

Miller, K., Chinzei, K., Orssengo, G., & Bednarz, P. (2000). Mechanical properties of brain tissue in-vivo: experiment and computer simulation. *J Biomech,* 33, 1369-1376.

Miller, P.L., & Dimotakis, P.E. (1996). Measurements of scalar power spectra in high Schmidt number turbulent jets. *J Fluid Mech,* 308, 129-146.

Mitsakou, C., Helmis, C., & Housiadas, C. (2005). Eulerian modelling of lung deposition with sectional representation of aerosol dynamics. *J Aerosol Sci,* 36, 75-94.

Morsi, S.A., & Alexander, A.J. (1972). An investigation of particle trajectories in two-phase flow systems. *J Fluid Mech,* 55, 193-208.

Murphy, S.A., Tice, R.R., Smith, M.G., & Margolin, B.H. (1992). Contributions to the Design and Statistical-Analysis of Invivo Sce Experiments. *Mutat Res,* 271, 39-48.

Nene, R.R. (2006). Design of bio-aerosol sampling inlets. M.S. Thesis, Department of Mechanical Engineering, Texas A&M University, College Station, Texas. Available online at: http://txspace.tamu.edu/handle/1969.1/5736?show=full.

Nerisson, P., Simonin, O., Ricciardi, L., Douce, A., & Fazileabasse, J. (2011). Improved CFD transport and boundary conditions models for low-inertia particles. *Comput Fluids,* 40, 79-91.

Nowak, N., Kakade, P.P., & Annapragada, A.V. (2003). Computational fluid dynamics simulation of airflow and aerosol deposition in human lungs. *Ann Biomed Eng,* 31, 374-390.

Papavergos, P.G., & Hedley, A.B. (1984). Particle deposition behavior from turbulent flows. *Chem Eng Res Des,* 62, 275-295.

Park, S.S., & Wexler, A.S. (2007). Particle deposition in the pulmonary region of the human lung: Multiple breath aerosol transport and deposition. *J Aerosol Sci,* 38, 509-519.

Parker, S., Foat, T., & Preston, S. (2008). Towards quantitative prediction of aerosol deposition from turbulent flows. *J Aerosol Sci,* 39, 99-112.

Pich, J. (1966). The effectiveness of the barrier effect in fiber filters at small Knudsen numbers. *Staub Reinhalt. Luft.,* 26, 1-4.

Pleil, J.D., Mcclenny, W.A., Holdren, M.W., Pollack, A.J., & Oliver, K.D. (1993). Spatially resolved monitoring for volatile organic-compounds using remote sector sampling. *Atmos Environ a-Gen,* 27, 739-747.

Pope, S.B. (2000). *Turbulent flows*. Cambridge, England: Cambridge University Press.

Reist, P.C. (1984). *Introduction to aerosol science*. New York: Macmillan Pub. Co. & Collier Macmillan.

Rostami, A.A. (2009). Computational modeling of aerosol deposition in respiratory tract: A Review. *Inhal Toxicol,* 21, 262-290.

Saffman, P.G. (1965). Lift on a small sphere in a slow shear flow. *J Fluid Mech,* 22, 385-400.

Schilichting, H. (1968). *Boundary layer theory*. New York: McGraw-Hill.

Schobeiri, M. (2010). *Fluid mechanics for engineers: a graduate textbook*. Berlin Heidelberg, Germany: Springer-Verlag.

Sehmel, G.A. (1970). Particle deposition from turbulent air flow. *J Geophys Res,* 75, 1766-1781.

Shang, X.D., & Xia, K.Q. (2001). Scaling of the velocity power spectra in turbulent thermal convection. *Phys Rev E,* 64.

Shapiro, M., & Brenner, H. (1989). Dispersion and deposition of aerosol-particles in porous filters. *J Aerosol Sci,* 20, 951-954.

Stahlhofen, W. (1980). Experimentally determined regional deposition of aerosol-particles in the human respiratory-tract. *Clin Res Proc,* 16, P145-P147.

Stahlhofen, W., Gebhart, J., Heyder, J., & Scheuch, G. (1983). New regional deposition data of the human respiratory-tract. *J Aerosol Sci,* 14, 186-188.

Stapleton, K.W., Guentsch, E., Hoskinson, M.K., & Finlay, W.H. (2000). On the suitability of k-epsilon turbulence modeling for aerosol deposition in the mouth and throat: A comparison with experiment. *J Aerosol Sci,* 31, 739-749.

Stein, S.W. (2008). Aiming for a moving target: Challenges with impactor measurements of MDI aerosols. *Int J Pharm,* 355, 53-61.

Tang, Y.J., & Guo, B. (2011). Computational fluid dynamics simulation of aerosol transport and deposition. *Frontiers of Environ Sci & Eng in China,* 5, 362-377.

Tang, Y.J., Guo, B., & McFarland, A.R. (2010). A computational fluid dynamics study of particle penetration through an omni-directional aerosol inlet. *Aerosol Sci Tech,* 44, 1049-1057.

Tronville, P., & Rivers, R. (2005). Numerical modeling of the flow resistance of fibrous air filter media having random fiber diameter. In *FILTECH conference* (2005) Wiesbaden, 2, 261-268.

Tsai, C.J., Lin, J.S., Aggarwal, S.G., & Chen, D.R. (2004). Thermophoretic deposition of particles in laminar and turbulent tube flows. *Aerosol Sci Tech,* 38, 131-139.

Tsuji, Y. (2007). Multi-scale modeling of dense phase gas-particle flow. *Chem Eng Sci,* 62, 3410-3418.

Vames, J.S., & Hanratty, T.J. (1988). Turbulent dispersion of droplets for air-flow in a pipe. *Exp Fluids,* 6, 94-104.

Vincent, J.H. (1995). *Aerosol science for industrial hygienists*. Tarrytown, N.Y: Pergamon, Elsevier Science.

Vinchurkar, S., Longest, P.W., & Peart, J. (2009). CFD simulations of the Andersen cascade impactor: Model development and effects of aerosol charge. *J Aerosol Sci,* 40, 807-822.

Wang, J., & Pui, D.Y.H. (2009). Filtration of aerosol particles by elliptical fibers: a numerical study. *J Nanopart Res,* 11, 185-196.

Wang, Q., & Squires, K.D. (1996). Large eddy simulation of particle deposition in a vertical turbulent channel flow. *Int J Multiphas Flow,* 22, 667-683.

Wang, Q., Squires, K.D., Chen, M., & McLaughlin, J.B. (1997). On the role of the lift force in turbulence simulations of particle deposition. *Int J Multiphas Flow,* 23, 749-763.

Wedding, J.B., Weigand, M., John, W., & Wall, S. (1980). Sampling effectiveness of the inlet to the dichotomous sampler. *Environ Sci Technol,* 14, 1367-1370.

Wilcox, D.C. (2006). *Turbulence modeling for CFD* (3rd ed.). La Cãnada, Calif: DCW Industries.

Witschger, O. (2000). Sampling of airborne dusts in workplace atmospheres. *Kerntechnik,* 65, 28-33.

Yeh, H.C., & Liu, B.Y.H. (1974). Aerosol fIltration by fibrous filters. *J Aerosol Sci,* 5, 191-217.

Zhang, F.P., & Li, A.G. (2008). CFD simulation of particle deposition in a horizontal turbulent duct flow. *Chem Eng Res Des,* 86, 95-106.

Zhang, Y., Finlay, W.H., & Matida, E.A. (2004). Particle deposition measurements and numerical simulation in a highly idealized mouth-throat. *J Aerosol Sci,* 35, 789-803.

Zhou, H., Mo, G.Y., Zhao, J.P., & Cen, K.F. (2011). DEM-CFD simulation of the particle dispersion in a gas-solid two-phase flow for a fuel-rich/lean burner. *Fuel,* 90, 1584-1590.

APPENDIX A

In simulations on the performance of BSI-e device, some effects of individual parameters on the simulation are discussed in this appendix. Sensitivity analysis are carried out for the size of the computational domain, the number of particle released, the tracking steps of particles and the effect of the orientation of the inner plenum.

A.1 Sensitivity Analysis on Effect of Size of the Computational Domain

The criterions of the height and the width of the domain 'tunnel' were considered and simulated before the efficiency study. Various heights and widths were adjusted and analyzed in multiple simulations, and the comparison results were shown in Figure A.1 and Figure A.2. The maximum velocity on the surface of domain could be more closed to the free wind speed as the height and width of the domain increased. However, the larger cross section of the domain 'box-shaped tunnel' was simulated, the more mesh cells and simulation time would be needed. To consider about the balance between these two, the criterion of height and width of the domain were set to be that the maximum velocity on the 'symmetric' surfaces would remain less than 110% of the free wind speed. So the cross-section of the domain was set to be $21'' \times 21''$ for this case. And in 24 km/h case, the maximum velocities of the top and lateral surfaces of the domain are 8.9% and 8.5% larger than the free wind speed, separately. Figure A.3 and A.4 showed the penetration efficiency at various height and width of the computational domain. It

also suggested that the penetration remained almost constant at the region of dimensions used in this research.

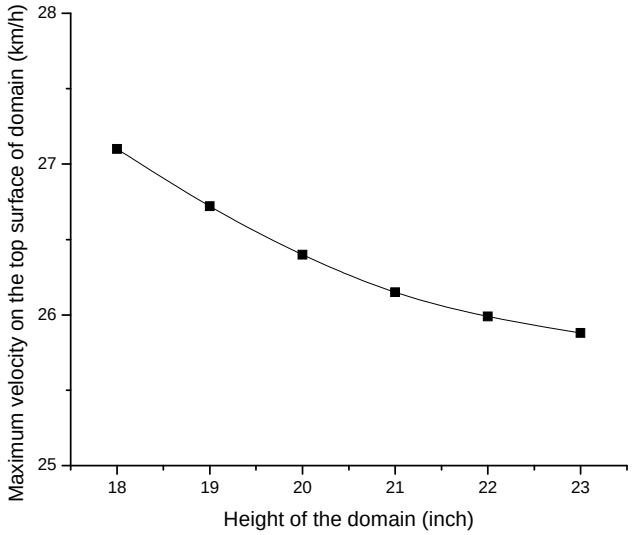

Figure A.1 Maximum velocity on the top surface of domain as a function of height of domain based on CFD simulation at a wind speed of 24 km/h.

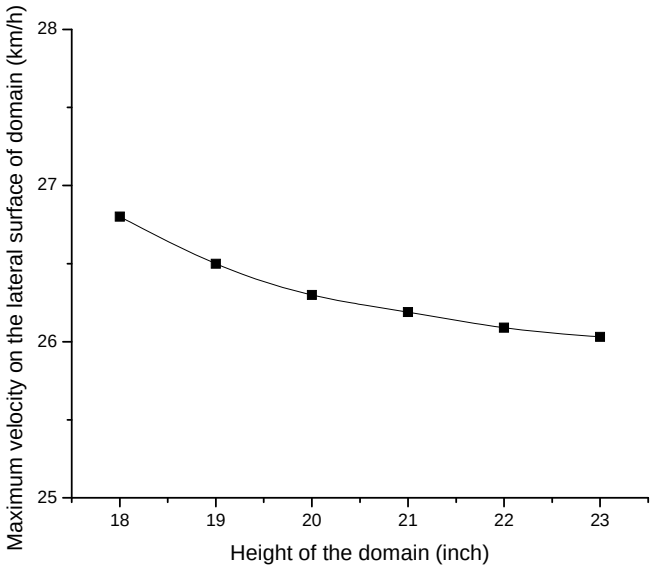

Figure A.2 Maximum velocity on the lateral surface of domain as a function of height of domain based on CFD simulation at a wind speed of 24 km/h.

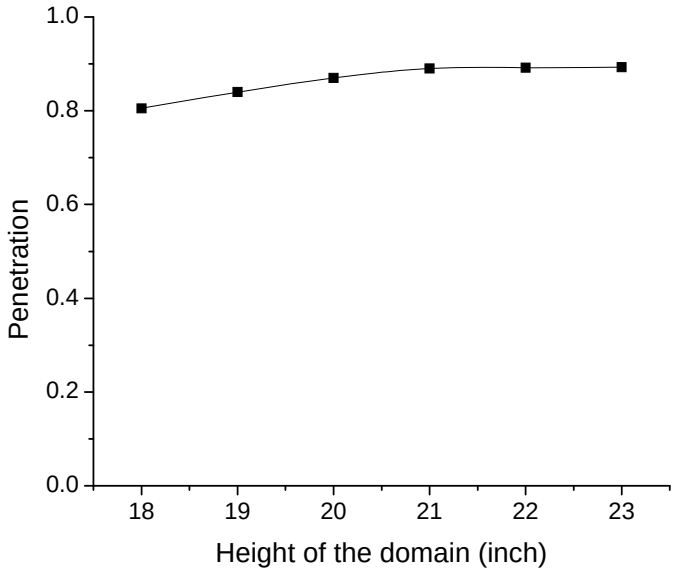

Figure A.3 Penetration efficiency as a function of height of domain based on CFD simulation at a wind speed of 24 km/h and a particle diameter of 10 micrometer.

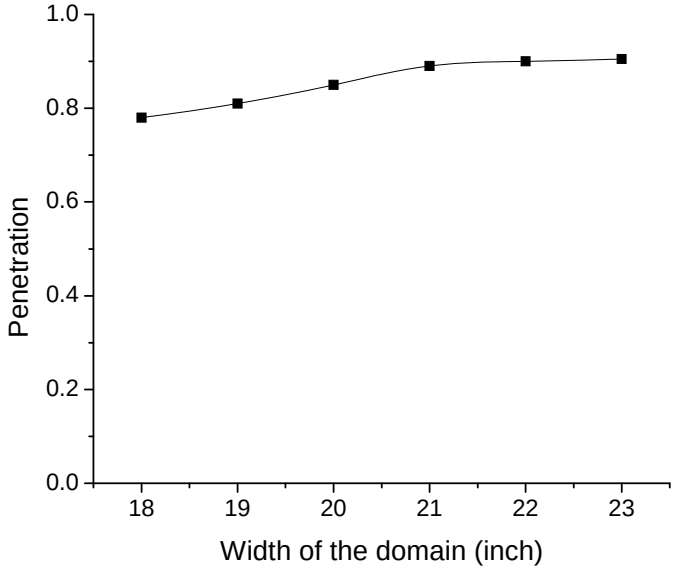

Figure A.4 Penetration efficiency as a function of width of domain based on CFD simulation at a wind speed of 24 km/h and a particle diameter of 10 micrometer.

A.2 Sensitivity Analysis on Effect of Number of the Particles Released/tracked

With the turbulent dispersion involved, the simulation would release 100 particles at each single particle injection points on the domain inlet boundary, and the turbulence fluctuation would cause randomly different trajectories for these 100 particles. The total number of particles released/tracked was set to be 10000~100000 in order to show sensitivity of the effect on the penetration efficiency in Figure A.5. The predicted penetration efficiency remains constant after the maximum number of particles used in simulation increases to 50,000. Considering the operation time for the numerical simulation, the final results of simulation were taken under the condition that the maximum particle number is 400,000 (4000 particle injection points were built on the domain inlet boundary).

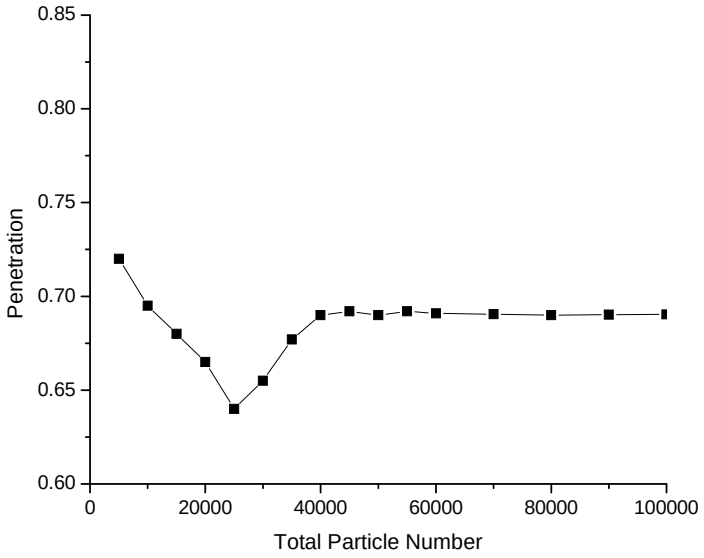

Figure A.5 Sensitivity analyses on total particle number in simulation.

A.3 Sensitivity Analysis on Effect of Max Number of Steps of Tracking Particles

The max number of steps in particles tracking was set to be 5000~40000 in order to show sensitivity of the effect on the penetration efficiency in Figure A.6. The predicted penetration efficiency reaches a constant value at approximately 15000 integration steps of tracking particles. Varying the number of tracking steps below 15000 results in a few percentage points difference in the predicted penetration efficiency. So all the final results of simulation were taken under the parameter: Max number of steps in particle tracking is 20000.

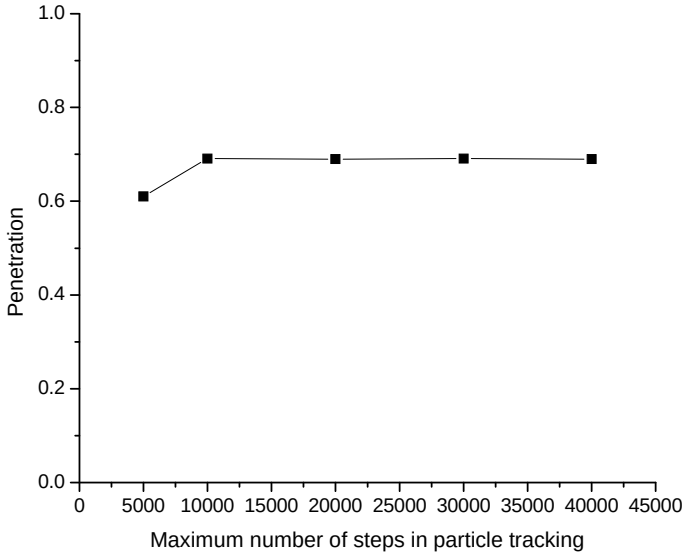

Figure A.6 Sensitivity analyses on max number of steps in particle tracking.

A.4 Effect of Orientation of the Inner Plenum

The bell-shaped inlet was designed for omni-directional aerosol sampling. The circumferential intake ensured that the sampling process remained the same status when

the sample flow came from different direction. However, note that the windows (no. 5 in Figure 2.1) at top of the inner plenum and the frames between the windows might cause different effect on the flow field in chamber and the penetration efficiency of BSI-e. Six windows (1.5 inch in height) are located near the top of the inner plenum, with 0.375 inch distance between. In this study, simulations had been done to show the difference between two extreme conditions: the free wind flow direction is perpendicular to one of the windows (CASE I) on the inner plenum or one of the frames between windows (CASE II). The results (Table A.1) showed that the largest difference of the penetration efficiency between these two conditions was about 2%.

Table A.1 The comparison of the prediction for different orientation of the inner plenum.

Particle Diameter μm	**Free stream wind speed** 24 km/h	
	CASE I	CASE II
2	98.3%	97.8%
5	96.7%	95.5%
10	89.0%	87.4%
15	55.8%	53.7%
20	N/A	N/A

VITA

Name: Yingjie Tang

Address: Department of Mechanical Engineering, Texas A&M University,
College Station, TX 77843-3123

Email Address: tangyingjie823@gmail.com

Education: B.S., Thermal Engineering, Tsinghua University, China, 2006
M.S., Thermal Engineering, Tsinghua University, China, 2008
Ph.D., Mechanical Engineering, Texas A&M University, TX, 2012